

**DEVELOPMENT OF A SPATIAL
HETERODYNE SPECTROMETER AND
ASSOCIATED INSTRUMENTATION FOR
SPACE AND GROUND OBSERVATORIES**

A Thesis

Submitted for the Degree of
Doctor of Philosophy (Technology)

Submitted by

NIRMAL K

Department of Applied Optics & Photonics

University College of Technology

University of Calcutta

SEPTEMBER 2018

*To my Family,
Friends and Teachers...*

List of Publications

1. Refereed Journal Articles

- (a) **Design and modeling of a tunable spatial heterodyne spectrometer for emission line studies - *K Nirmal, Sridharan Rengaswamy, Sripadmanaban Nadar Sriram, Jayant Murthy, Ambily Suresh, Margarita Safonova, Aickara Gopinathan Sreejith, Joice Mathew, Mayuresh N. Sarpotdar, J. Astron. Telesc. Instrum. Syst.* 4(2) 025001 (17 May 2018).**¹
- (b) **Pointing System for the Balloon-Borne Astronomical Payloads - *K Nirmal, A. G. Sreejith, Joice Mathew, Mayuresh Sarpotdar, Ambily Suresh, Ajin Prakash, Margarita Safonova, Jayant Murthy* , Journal of Astronomical Telescopes, Instruments and Systems, Vol. 02, issue. 04, 047001, 2016.**²
- (c) **Overview of High-Altitude Balloon Experiments at the Indian Institute of Astrophysics- *Margarita Safonova, Akshata Nayak, A. G. Sreejith, Joice Mathew, Mayuresh Sarpotdar, S. Ambily, K. Nirmal, Sameer Talnikar, Shripathy Hadigal, Ajin Prakash & Jayant Murthy*, Astronomical and Astrophysical Transactions (AApTr), Vol. 29(3): 397-426 2016.**³

2. Refereed Conference Proceedings

- (a) **Wavelength calibration of a tunable spatial heterodyne spectrometer, *K. Nirmal, Sridharan R., S. Sriram, Suresh Ambily, Joice Mathew, Mayuresh Sarpotdar, Jayant Murthy, Binukumar Gopalakrishnan, Margarita Safonova*, Proc. SPIE 10702, Ground-based and Airborne Instrumentation for Astronomy VII, 107024V (6 July 2018)**

¹Presented in Chapter 1,2 and 3

²Presented in Chapter 6

³Presented in Chapter 3

-
- (b) **Noise modeling and analysis of an IMU-based attitude sensor: improvement of performance by filtering and sensor fusion**, **K Nirmal**, Sreejith A. G., Joice Mathew, Mayuresh Sarpotdar, Ambily Suresh, Ajin Prakash, Margarita Safonova, Jayant Murthy, Proc. SPIE 9912, Advances in Optical and Mechanical Technologies for Telescopes and Instrumentation II, 99126W (22 July 2016)
 - (c) **Near UV imager with an MCP-based photon counting detector** - *S. Ambily, Joice Mathew, Mayuresh Sarpotdar, A. G. Sreejith, **K. Nirmal**, Ajin Prakash, Margarita Safonova and Jayant Murthy*, Proc. SPIE 9905, Space Telescopes and Instrumentation 2016: Ultraviolet to Gamma Ray, 990530 July 11, 2016.
 - (d) **Balloon UV experiments for astronomical and atmospheric observations** - *A. G. Sreejith, Joice Mathew, Mayuresh Sarpotdar, **K Nirmal**, Ambily S., Ajin Prakash, Margarita Safonova and Jayant Murthy*, Proc. SPIE 9908, Ground-based and Airborne Instrumentation for Astronomy VI, 99084E August 9, 2016

3. Journal articles not part of this thesis

- (a) **A software package for evaluating the performance of a star sensor operation** - *Mayuresh Sarpotdar, Joice Mathew, A. G. Sreejith, **K. Nirmal**, S. Ambily, Ajin Prakash, Margarita Safonova, Jayant Murthy*, Experimental Astronomy, Vol 43, Issue 1, pp 99–117, February 2017.
- (b) **Prospect for UV observations from the Moon. II. Instrumental Design of an Ultraviolet Imager LUCI** - *Joice Mathew, Ajin Prakash, Mayuresh Sarpotdar, A. G. Sreejith, **K. Nirmal**, S. Ambily, Margarita Safonova, Jayant Murthy and Noah Brosch*, Astrophysics and Space Science, Vol 362, Issue 2, pp 11, February 2017.

- (c) **Measurement of limb radiance and Trace Gases in UV over Tropical region by Balloon-Borne Instruments - Flight Validation and Initial Results** - *A. G. Sreejith, Joice Mathew, Mayuresh Sarpotdar, **K. Nirmal**, S Ambily, Ajin Prakash, Margarita Safonova and Jayant Murthy*, Atmos. Meas. Tech. Discuss., amt-2016-98, 2016.

Presentations

1. **Pointing system for balloon borne telescope-** *Nirmal Kaipachery, A.G. Sreejith, Joice Mathew, Mayuresh Sarpotdar, Ambily Suresh, Margarita Safonova and Jayant Murthy*, 32nd ASI Meeting, ASI Meeting, 2015, NCRA, Pune, **Poster presentation.**
2. **Wavelength calibration of Tunable Spatial Heterodyne Spectrometer-** *Nirmal Kaipachery, R. Sridharan, S. Sriram, Jayant Murthy, S. Ambily, A. G. Sreejith, Joice Mathew, Mayuresh Sarpotdar and Margarita Safonova*, SPIE Astronomical Telescopes + Instrumentation, 2018, Austin, TX, USA, **Poster presentation.**

Abstract

We describe the development of compact, lightweight payloads suitable for ground, space, and balloon-based observatories. The first instrument is a compact high resolution (≥ 20000) tunable spatial heterodyne spectrometer (TSHS). Spatial Heterodyne Spectroscopy (SHS) is a relatively novel interferometric technique similar to the Fourier transform spectroscopy with heritage from the Michelson Interferometer. An imaging detector is used at the output of an SHS to record the spatially-heterodyned interference pattern. The spectrum of the source is obtained by Fourier transforming the recorded interferogram. Since these instruments do not have slits, the entire incoming beam can be used to generate the spectrum. The small bandwidth limitation of the SHS can be overcome by building it in a tunable configuration (TSHS). This instrument can be used to observe and study faint, extended emission line targets by retrieving the high-resolution spectra from the entire source.

The second instrument is a pointing system suitable for balloon mission. Our first balloon observations were of atmospheric lines where the pointing stability is less critical, but now we are observing astronomical sources for which a pointing mechanism is required. Hence, in this work, we describe the design and realization of a low-cost light-weight 2-axis correction pointing and stabilization system intended for use in small balloon flights, built entirely using off-the-shelf components with an accuracy of 0.5 degrees.

Contents

List of Publications	iii
Abstract	ix
List of Figures	xv
List of Tables	xxvii
1 Introduction	1
1.1 Introduction	1
1.2 High Altitude Balloon in Astronomy	2
1.3 Spatial Heterodyne Spectrometer	4
1.3.1 Earlier SHS instruments	5
1.3.2 Our Tunable SHS system	7
1.4 Pointing system for balloon-borne telescope	7
1.5 Thesis outline	9
2 Spatial Heterodyne Spectroscopy concept	11
2.1 Introduction to Fundamentals of SHS	11
2.2 Mathematical formulation	12
2.2.1 Limitations of SHS	17
2.3 Summary	18

3	Simulation of SHS system in Zemax and MATLAB	19
3.1	Introduction	19
3.2	Modeling of SHS system in Zemax [®]	19
3.2.1	Tunable SHS	21
3.2.2	Tunability of the system	22
3.2.3	Identifying the wavelength	22
3.3	Interferogram with more than one emission line	23
3.4	Simulation of SHS system in MATLAB	25
3.5	Summary	29
4	Design, Implementation and First Light results	31
4.1	Introduction	31
4.2	Design considerations of a tunable SHS	32
4.2.1	Entrance Optics and Collimation	32
4.2.2	Gratings and beam splitter	32
4.2.3	Exit Optics	33
4.3	Alignment of the instrument	33
4.4	Experimental setup and first results	35
4.4.1	Estimation of Resolving Power (R)	37
4.4.2	Checking the tunability of the system	39
4.4.3	Interferogram from a continuum source	39
4.5	Effect of line broadening on the interferogram	41
4.5.1	Effect of vibration on the system	43
4.5.1.1	Observation of the celestial object	43
4.6	Summary	45
5	Wavelength calibration and implementation of a pipeline.	49
5.1	Introduction	49
5.2	Wavelength Calibration	50
5.3	Wavelength Calibration setup	52
5.4	Calibration procedure	53

5.5	Dark correction	54
5.6	Flat-fielding	57
5.7	Spectral leakage correction in SHS	58
5.8	A Python-based pipeline for SHS	61
5.9	Summary	63
6	Pointing system for balloon borne telescope	65
6.1	Introduction	65
6.2	Basic Principle and Realization of the System	66
6.3	Control Mechanisms	68
6.3.1	Conversion of Equatorial coordinates into horizontal coordinates	69
6.3.2	ACS computation	70
6.3.3	Estimation of the attitude	70
6.3.4	Estimation of azimuth	73
6.4	Checking the magnetometer calibration	78
6.5	Correcting the pointing position	78
6.5.1	Estimation of disturbances on the payload	79
6.5.2	Simulation of control system	81
6.5.3	Hardware implementation of the PID algorithm.	84
6.6	Pointing System Program Flowchart	84
6.7	Performance tests	84
6.7.1	Ground test	85
6.7.2	Tethered flights	86
6.7.3	Technical Specifications of the Controller	90
6.7.4	Power requirement	90
6.7.5	Data Handling	91
6.7.6	Technical Specifications about motor	91
6.8	Summary	92

7 Summary and Future work	93
7.1 Summary	93
7.2 Future works	94
7.2.1 Selection of material	95
Bibliography	101

List of Figures

1.1	An Image of the comet Ison. Image credit NASA/MSFC/Aaron Kingery	1
2.1	<i>Top Left:</i> The schematic diagram of the SHS system. L1, L2, and L3 are lenses, G1 and G2 are the gratings, and BS is the beam splitter. <i>Top Right:</i> The concept of fringe formation in SHS. The Littrow wavelength 350 nm does not create any fringes because the waves emerge parallel to each other from the two arms of the interferometer. Wavelengths other than Littrow form fringes on the detector because the gratings tilt them. <i>Bottom:</i> Zoomed version of one of the gratings.	12
2.2	A sinc function	16
2.3	The image of the grating with W as illuminated area. On the detector this area gets reduced to $W \cos \theta_L$. Hence x_{max} is $W \cos \theta_L$	17
3.1	A conceptual diagram of a tunable SHS modeled in Zemax [®] . G1, G2 are the gratings, BS is the beam splitter, and D is the detector.	20

-
- 3.2 The simulated detector view: generated interferogram in x and y positions, $I(x, y)$ is displayed when the incoming beam constituted of only the wavelength 450.0187 nm (*Left*), 450 nm (Littrow) (*Middle*) and 449.981 nm (*Right*). The size of the detector is 12 mm \times 12 mm, having 512 \times 512 pixels. The white circular patch (10 mm beamwidth) is the illuminated area of the detector. These images have been processed to enhance the fringe contrast. 20
- 3.3 The relation between the Littrow angle and wavelength for the holographic grating with 1200 lines/mm. 21
- 3.4 Simulated detector view: generated interferogram in x and y positions, $I(x, y)$ is displayed when the input beam constitutes only the wavelength 549.977 nm (*Left*), 550 nm (Littrow) (*Middle*) and 550.023 nm (*Right*). The size of the detector is 12 mm \times 12 mm, having 512 \times 512 pixels. The white circular patch (10-mm beamwidth) is the illuminated area of the detector. These images have been processed to enhance the fringe contrast. 22
- 3.5 Simulated fringes obtained for wavelength 450.0562 nm (*Left*) and for 449.944 nm (*Right*), when the grating G1 is tilted 0.001 $^\circ$ in the direction perpendicular to the Littrow angle. The Littrow wavelength for this setup is 450 nm. These images have been processed to enhance the fringe contrast. 23
- 3.6 Simulated detector view: generated interferogram in x and y positions, $I(x, y)$ is displayed when the input beam constitutes of wavelength 650.1 nm (*Left*), and 650.3 nm (*Right*). The size of the detector is 10 mm \times 10 mm, having 512 \times 512 pixels. The white circular patch (8-mm beamwidth) is the illuminated area of the detector. 24
- 3.7 A pictorial representation of the spectrum input to the Zemax simulation. 25

- 3.8 Simulated detector view: generated interferogram in x and y positions, $I(x, y)$ is displayed when the input beam constitutes of wavelength 650.1 nm and 650.3 nm. *Left* shows when the gratings doesn't have any tilt other than Littrow angle and *Right* shows when of the grating has a tilt of 0.01 degrees in a direction perpendicular to the littrow angle. The size of the detector is 10 mm \times 10 mm, having 512 \times 512 pixels. The white circular patch (8-mm beamwidth) is the illuminated area of the detector. 25
- 3.9 An enlarged version of the FFT of the interferogram generated for emission lines 650.1nm and 650.3nm (Fig. 3.8, Right). The central bright spot corresponds to the zero frequency value and the other two spots on the right of zero frequency corresponds to the emission line strength of 650.1nm and 650.3 nm respectively and the two spots left of zero frequency value are the corresponding negative frequencies 26
- 3.10 The block diagram representing the simulated model of SHS in MATLAB. 26
- 3.11 *Left:* The spectrum profiles that is fed to the system. The spectrum profiles are Gaussian function having different FWHM. Top left panel shows an emission line with FWHM of 0.005nm, Middle left panel shows an emission line with FWHM 0.05 nm, and bottom left panel shows an emission line with FWHM of 0.25nm. The simulated detector view corresponding to each spectrum profile is shown in the right panel. 28
- 4.1 Raw fringes obtained for a laser diode of wavelength 650nm. . 35
- 4.2 The TSHS setup arranged on a bread board (top view). CS is the collimator setup, F is the filter, L1 is the imaging lens, BS is the beam splitter, D is the detector, RS1 and RS2 are the rotational stages, and TS1, TS2 are the translational stages. . 36

-
- 4.3 First result obtained using a sodium vapor lamp. Two distinct fringes can be seen in the image corresponding to wavelengths 589 nm and 589.6 nm. However the fringe contrast is very poor due to mismatch in path length and poor imaging. 36
- 4.4 *Top:* The fringe obtained from the sodium vapor lamp. Two distinct fringes can be seen in the image corresponding to wavelengths 589 nm and 589.6 nm, respectively. *Bottom:* The two-dimensional FFT of the flat-corrected interferogram. 37
- 4.5 The spectrum of the sodium vapor lamp retrieved from the interferogram, (*Top:*) in pixel scale and in (*Bottom:*) in wavelength scale. 38
- 4.6 *Top:* The emission line corresponding to 589 nm (continuous line) and the fitted Gaussian curve (dotted line). *Bottom:* The emission line corresponding to 589.6 nm (continuous line) and the fitted Gaussian curve (dotted line). 39
- 4.7 The visible spectrum of a Helium lamp. Image courtesy: <https://www.sciencephoto.com> 40
- 4.8 Fringes obtained for different emission lines in the Helium lamp spectra. The emission line for each fringes follows the order 438.793 nm, 447.148 nm, 501.567 nm, 587.562 nm, and 667.815nm 41
- 4.9 The setup of monochromator Andor SR-303IA and halogen lamp. A halogen lamp produces a continuous spectrum. The monochromator is used to select a particular wavelength region. 42
- 4.10 The spectral distribution of a halogen lamp. Image courtesy: <http://zeiss-campus.magnet.fsu.edu/articles/lightsources> 42

4.11 Fringes obtained for a continuum source – halogen lamp. The central wavelength is changed using the monochromator. *Top Left:* Fringes obtained for a wavelength band centered at 587 nm. *Top Right:* Fringes obtained for a wavelength band centered at 588 nm. *Bottom:* Fringes obtained for a wavelength band centered at 589 nm. As the wavelength moves away from the central wavelength, there is a change in fringe frequency. 43

4.12 The variation in the interferogram with the output slit width of the monochromator. All the other parameters of the monochromator like the input slit width, the central frequency (589nm) are all kept the same except the output slit width. The output slit width of the monochromator corresponding to each fringe is as follows: from the top left corner, 200 μm , 400 μm , 500 μm , 1000 μm , 2000 μm and 2500 μm 44

4.13 Variation in the visibility of fringes in the presence of vibration. *Left:* Fringes corresponding to the H $_{\alpha}$ line of the hydrogen lamp taken with one-second exposure. The air conditioner was on during the exposure. The vibration caused by the air conditioner reduced the visibility of the fringes. *Right:* Same observation but with air conditioner switched off during the exposure. 45

-
- 4.14 *Top, Left:* The interferogram obtained for the Betelgeuse. The circular patch is the illuminated area of the grating imaged on to the detector. The fringes are visible in the central part of the illuminated area. *Middle:* The zoomed version of the 2D Fourier transform of the interferogram where spectrum is visible. The retrieved spectrum of the star (solid black line) along with the spectrum obtained from the ELODIE archive (red dashed line) is plotted together for comparison. The transfer function of the filter is not removed from the spectrum. The wavelength covered (FWHM) by the filter is shown in the green circle. 46
- 4.15 *Left:* The interferogram obtained for the Sirius. The circular patch is the illuminated area of the grating imaged on to the detector. The fringes are visible in the central part of the illuminated area. *Middle:* The zoomed version of the 2D Fourier transform of the interferogram where spectrum is visible. *Right:* The retrieved spectrum of the star (solid black line) along with the spectrum obtained from the ELODIE archive (broken red line) are plotted together for comparison. The transfer function of the filter is not removed from the spectrum. The wavelength covered (FWHM) by the filter is shown in the green circle. 47
- 5.1 Image of a Thorium-Argon lamp. Image courtesy *https : //www.photronlamp.com/products/p858a – thorium – argon* 50
- 5.2 The echelle spectrum of the Thorium Argon lamp. The bright dots represents the emission line in different orders. 51
- 5.3 The halogen lamp monochromator setup for wavelength calibration. 52
- 5.4 The interferogram obtained for different central wavelengths– 649nm, 650nm, 651nm, 652nm, and 653nm 54

5.5	The retrieved one dimensional spectrum (continuous line) from the interferogram corresponding to a monochromator central wavelength of 647 nm, 648 nm, 649 nm, 650 nm, 651 nm, 652 nm and 653 nm in the order from top Left. The fitted Gaussian profile is shown in broken line.	55
5.6	A graph showing the relationship between the fringe frequency and the central wavelength of the monochromator output. . .	56
5.7	(Top:) A dark frame generated from our image sensor by giving an exposure of 12s in log scale. The hot pixels are visible in the image.	57
5.8	Flats obtained by closing each arm of the interferogram. There is a slight intensity difference in each individual flat which is due to the ratio at which the beamsplitter splits light into each arm of the SHS.	58
5.9	Flat fielding applied to different signal. (Top, Left) The uncorrected interferogram corresponding to 648.5nm and (Top, Right) corrected interferogram corresponding to central wavelength 648.5nm. (Middle, Left) The uncorrected interferogram corresponding to 648.5nm and (Middle, Right) corrected interferogram corresponding to central wavelength 650.2nm. (Bottom, Left) The uncorrected interferogram corresponding to 648.5nm and (Bottom, Right) corrected interferogram corresponding to central wavelength 650 nm.	59
5.10	<i>Top Left:</i> The fringes obtained on the detector for the sodium vapor lamp. The original fringes are cropped to get 256×256 pixel as in figure. <i>Top Right:</i> The two dimensional Fourier transform of the obtained fringes. <i>Bottom:</i> The Fourier transform of the apodized fringes with a triangular window (Left) with a hamming window (right).	61

5.11	Different windowing function used to correct the spectral leakage. (Top, left) Hanning window, (Top, left) Hamming window, (Middle, left) triangular window, (Middle, right) Bartlett window, (Bottom) Barthann window	62
5.12	<i>Top:</i> The retrieved sodium vapor lamp spectrum after the multiplication of the window function. A zoomed version of the spectrum around the emission line is shown in the bottom panel.	63
5.13	The Graphical user interface of the python based pipeline of the SHS instrument. The localized fringe is shown in the rectangle.	64
5.14	A block diagram showing the SHS python pipeline.	64
6.1	The azimuth with respect to magnetic north represented on a horizontal plane. Image courtesy: http://directionaldrilling.blogspot.com	66
6.2	<i>Top:</i> Mechanical structure of pointing system. <i>Bottom:</i> Pointing system mounted on the payload.	67
6.3	A block diagram of the Attitude Control System (ACS).	69
6.4	<i>Left:</i> Results of the ACS calibration, on June 18, 2015. Difference between solar elevation obtained from NOAA (blue line) and elevation calculated using Eq. (1) (red line). Inlet: Zoom on the calculated elevation to show the error bars. <i>Right:</i> Difference between solar azimuth obtained from NOAA (blue line) and calculated azimuth using Eq. (1) (red line). Inlet: Zoom on the calculated azimuth to show the error bars.	71
6.5	<i>Top:</i> Elevation calculated from the accelerometer shows considerable scatter. <i>Bottom:</i> The sensor-fused elevation data from accelerometer and gyroscope using Kalman-filter is much smoother.	73

- 6.6 The figure shows the nonlinearity in magnetometer reading. The heading calculated from uncalibrated magnetometer measurements (line) and the heading calculated from calibrated magnetometer measurement (dots). 74
- 6.7 The magnetic field strength measured using the MEMS magnetometer. MagX, MagY, and MagZ are ADC readings correspond to the measured magnetic field strength in x, y, and z-axis of the magnetometer respectively. The red dots are the measured magnetic field strengths, and the green sphere is the ellipsoid fit. 76
- 6.8 Variation in magnetic inclination and declination with altitude. 77
- 6.9 Variation in azimuth estimated from the magnetometer readings with altitude. 77
- 6.10 *Top*: One of the images taken during the ground test when the magnetometer was not calibrated. *Bottom*: The image of the Moon taken during the ground test where the magnetometer is calibrated for hard iron and soft iron biases. The position of the Moon is marked in a rectangle. 79
- 6.11 Wind direction (*Left*) and movement of the payload in azimuth (*Right*) after reaching the stratosphere. Time axis shows time in hours elapsed since launch. The float altitude was reached at about 2 hrs after launch. The plots clearly show the difference between the rapid variation of payload azimuth before reaching the final float altitude and less variation of payload azimuth after reaching the float altitude. 80
- 6.12 *Top*: The motion of the payload in azimuth during the balloon flight. *Bottom*: The rms velocity ($^{\circ}/s$) of the payload in azimuth. 81
- 6.13 A block diagram of control system model, where \mathbf{r} is the control signal, \mathbf{d} is the disturbance (load), \mathbf{e} is the error signal and θ is the angle rotated by the motor shaft. 82

-
- 6.14 The closed loop step response of the system. *Top:* without the PID controller, *Bottom:* with the PID controller of gain $K_p = 2$, $K_d = 1$ and $K_i = 2$. The settling time is reduced to the satisfactory value. 83
- 6.15 Block diagram of the PID algorithm implemented in the controller. 84
- 6.16 The response of the PID controller for different proportional, integral and differential gains. *Y*-axis shows the deviation in percentage between the programmed and current position. For $K_p = 0.25$, $K_d = 0.25$, $K_i = 0.25$, the system response is slow (*Left*). Fast and stable response achieved with gain values $K_p = 2$, $K_i = 1$, $K_d = 2$ (*Middle*). For gains $K_p = 3$, $K_d = 3$, $K_i = 3$, the system becomes unstable and starts oscillating (*Right*). 85
- 6.17 A Program flowchart of the ACS. 86
- 6.18 *Left:* An image (the Sun) frame extracted from the video capture during the ground test. *Middle:* The isophote of the Sun's image scaled by 250:1. This isophote was used to find the centroid of the image. *Right:* The isophote of the Sun with overplotted centroids calculated for every image frame. The size of an image is marked in pixels. 87
- 6.19 The star-shaped platform is connected to the balloon through a parachute. The entire system is tethered to a spindle on the ground (not shown in figure) using a nylon tether of approximately 200 m length. 88
- 6.20 *Left:* Isophote of the Sun's image obtained during a tethered flight. *Right:* Individual centroids of the Sun in each of the 5 second frames are plotted on the over a period of 150 seconds. Scaling is the same as in Fig. 6.18. 89

6.21	The structure of the gimbal system. Different components used and their position on the gimbal is also marked. The azimuth frame is made of Aluminium, and the elevation frame is made of ABS plastic to reduce weight.	90
7.1	A schematic diagram of the field widened SHS.	95
7.2	The rate of change of refractive index of different glasses with respect to temperature is plotted against temperature.	97
7.3	The H_α of different Be stars (Top) HD225132, (Middle) HD11606, (Bottom) HD50138.	98
7.4	The mechanical structure of the whole system assembled.	98
7.5	A flowchart showing the program flow in the pointing system incorporated with the star sensor.	99

List of Tables

4.1	The components procured for building TSHS instrument.	34
4.2	Parameters obtained from the fitting of emission lines.	38
4.3	Details of Observations conducted on 20 March 2018	44
6.1	ACS programmed parameters.	70
6.2	Motion of the payload in elevation, azimuth and tilt.	80
6.3	ACS programmed parameters.	82
6.4	The closed loop step response parameters without and with an external PID	83
6.5	Ground test results of tracking stability	87
6.6	Technical specification of Arduino Mega controller.	91
6.7	Power requirement of various components in pointing system .	91
6.8	Details about data transfer between controller and sensor mod- ules	91
6.9	Technical specifications of the Servomotor	92
7.1	The refractive index of different glass from Schott glass catalog calculated using Sellmeier dispersion formula.	96

Chapter 1

Introduction

1.1 Introduction

In 2013 November the comet Ison (Fig. 1.1) passed through the solar system. This incidence was a great opportunity for the astronomers as well as comet lovers to study this great object in depth. We planned to observe this object in the Near Ultra Violet (NUV) regime of the electromagnetic spectrum through a 6- inch balloon-borne telescope and NUV spectrometer manufactured by *Ocean Optics*¹. However, we faced several challenges during this launch including lack of a lightweight pointing system for balloon-borne

¹<https://oceanoptics.com/>



Figure 1.1: An Image of the comet Ison. Image credit NASA/MSFC/Aaron Kingery

payloads and unavailability of a small compact high-resolution spectrometer. In this work, we tried to find a way to mitigate these issues. The problems mentioned above being the motivation, the thesis goals are to

1. Develop a compact high-resolution spectrometer.
2. Develop a lightweight, compact pointing system for balloon-borne payloads.

1.2 High Altitude Balloon in Astronomy

High-altitude balloon platforms are economical alternatives to space missions since the atmospheric conditions such as temperature and pressure at high altitudes are similar to that in near space. Stratospheric balloons are also used for testing instruments as well as for specific classes of observations, particularly observations of objects that require a rapid response, such as comets or other transients.

Hot air balloons had been used for aeronomy (Watson et al., 1995) previously and were inexpensive. These balloon platforms used a different kind of equipment such as Fourier Transform Infrared (FTIR) spectrometers, multi-spectral imaging spectrometers, mid- and far-infrared cameras to study the concentration of CO and O₃ in the atmosphere. They were able to collect and estimate the concentration CO and O₃ as a function of altitude.

Stratospheric balloons were used in astronomy for the first time in 1960-70s by Zeiss et al. (1969), and McCarthy et al. (1969). Later on, astrophysicists conducted several balloon experiments with instruments which were capable of performing observations at different wavelength regimes of the electromagnetic spectrum. There are two reasons behind conducting a balloon experiment in the astrophysical regime: first, to mitigate the effect of the Earth's atmosphere; second, to collect the photons which are opaque to earth's atmosphere.

Kunieda et al. (2006) explains the observation of hard X-ray from a high

altitude balloon. The hard X-rays above 25 keV is opaque to earth's atmosphere hence can be observed at the altitude of 40 km or above. The experiment was conducted to study non-thermal components from Super Novae Remnants (SNR) and Cluster of galaxies. Lamarre et al. (1990) explains about the use of the stratospheric balloon for the measurement of 3.3-micron feature in diffuse galactic emission feature. The project, namely *Pronaus* comprises a 2m class telescope, a sub-millimeter photometer, and a high-resolution heterodyne spectrometer.

Recently balloon experiments are gaining popularity with the introduction of balloon experiments such as SPIDER (Crill et al., 2008), balloon-borne large aperture submillimeter telescope (BLAST) (Pascale et al., 2008), and Balloon Experimental Twin Telescope for Infrared Interferometer (BETTII) (Rizzo et al., 2014). Even though these experiments use high altitude balloon platform the goals of these experiments are diverse, for example, SPIDER studies primordial gravitational wave imprinted on the cosmic microwave background with 6-degree resolution telescope. BLAST makes the high-resolution map of diffuse galactic emissions. BETTII is an infrared interferometric imager to view stars and star-forming region with an angular resolution of 5 arc seconds.

Safonova et al. (2016) describe our balloon program to study the sky in NUV regime (200-400 nm) which is not widely explored by the aeronomy and the astrophysical community. There are certain emission lines known as air-glow in the atmosphere which arise due to atmospheric chemical process.

Study of air-glow in NUV gives the chemical process happening in higher atmosphere and hence leads to the study of the atmospheric process including greenhouse effect and climate changes. Currently, we are exploring avenues to extend the balloon experiments for astrophysical purposes. However, the primary challenge we are facing right now is the development of lightweight, compact instruments for balloon mission. In the following sections, we describe an instrument which is suitable as a payload for lightweight balloon platforms, satellites, and ground-based observatories.

1.3 Spatial Heterodyne Spectrometer

Spectroscopy is one of the essential techniques used for the remote sensing of the celestial objects. However, the information achieved from spectroscopy is confined by the sensitivity, resolving power and spatial extent that can be covered by the instrument. In most of the high resolving power grating spectrometers, a narrow slit is used to achieve high resolution. However, the narrow slits limit the light gathering capacity of the instrument and hence the sensitivity. Therefore, high-resolution spectroscopy of faint extended objects in UV and visible is difficult because one has to compromise between the sensitivity and the resolving power. Another disadvantage of high-resolution grating spectrometers is that they tend to be quite bulky since the throw length of the instrument increases with the resolving power.

There are individual objects and phenomena in our solar system, viz. Comets, nebulae, planetary satellites, planetary auroras, and interplanetary medium, which are faint, extended and reservoirs of information. Low-resolution spectroscopy can only reveal their basic parameters such as composition, intensity, and energy distribution. However, high-resolution spectroscopy can reveal additional information such as velocity, temperature, pressure, and isotopic signatures (Harris et al., 2003). Scientific community usually uses interferometric spectral measurement technique such as Fourier Transform Spectrometer (FTS) or Spatial Heterodyne Spectrometer (SHS) (Harlander et al., 1990) in order to obtain the high-resolution spectrum.

However, FTS requires a scanning mirror which moves at the sampling of half of the resolution element which limits its applications to the laboratories where one does not have to worry about the exposure time and external vibrations. In this work, we probe the feasibility of another type of spectrometer known as the spatial heterodyne spectrometer which has the advantages of an FTS but does not require a scanning mirror for the scanning.

Since SHS do not have slits, the throughput of these instruments is higher than that of a slit-based grating spectrometer. However, off-axis rays in the

input beam reduce the fringe visibility and the efficiency of the system which in turn put a limitation on the field of view solid angle (FOV) of the SHS. The FOV of an uncompensated (Harlander et al., 1992) (without a field-widening prism) SHS is relatively small, given by $\frac{2\pi}{R}$, where R is the resolving power of the instrument. This FOV can be increased by introducing the field-widening prism in SHS arms and, hence, they are more sensitive compared to the grating spectrometers with similar configurations.

1.3.1 Earlier SHS instruments

There are different configurations of SHS instruments built for different science goals. In this section, we explore the previously built SHS instruments and their applications. Englert et al. (2009) describes the design and implementation of a long-wave infrared (LWIR) SHS –Spatial Heterodyne Imager for Chemicals and Atmospheric Detection (SHIMCAD) and first light results. Englert et al. (2009) was the first successful application of SHS in LWIR. The main advantage of this system over conventional grating spectrometer is that high throughput, no moving part, and the decontamination of the spectra by changing scenes. The wavelength coverage of this instrument is between $8.4\mu m$ (1190 cm^{-1}) and $11.2\mu m$ (890 cm^{-1}) with a spectral resolution of about 4 cm^{-1} .

Milligan et al. (1999) describes the optical design of an infrared imaging spatial heterodyne spectrometer, the design constraints of the long wave infrared (LWIR), and the choices made to mitigate these issues. Milligan et al. (1999) also explains the simulated expected performance of the design and the details about the second generation instruments.

Harlander et al. (2010) explains the design of an all reflection grating with broad spectral coverage. This system was built using custom gratings having very low groove density (18 lines/mm). The fringes from additional grating orders achieve the broader coverage which superimposes with the prime fringes of the interferometer. Hence the wavelength coverage of this

instrument is four times that of the conventional SHS.

Mierkiewicz et al. (2004) reports a near UV payload based on SHS. They describe the development and the first light performance of the instrument. The instrument was built to study the O[II] emission lines (372.6 nm and 372.9 nm) from the interstellar medium of the galaxy. The lines arise from the warm ionized component of the galaxy. The sensitivity of the system is 10000 fold larger than conventional grating spectrometer having the similar configurations since this instrument uses field widening techniques to increase the light gathering capacity.

Kenneth et al. (2012) describes a Doppler Asymmetric Spatial Heterodyne (DASH) interferometer which was built to measure the thermospheric line of sight wind speed. This instrument is suitable to use from the ground or a satellite. They have discussed the thermal effect on the DASH instrument using a model in which each optical component is allowed to expand independently with variation in temperature and hence mitigate the due distortion stresses induced by the thermal expansion which helps in the selection of the materials for the interferogram design. The major science goals of the SHS instruments can be summarized as follows:

1. Near simultaneous study of the brightness and line shapes of atomic and molecular diagnostic emissions from astrophysical targets, such as comets or planetary atmosphere.
2. Remote sensing of faint extended targets interstellar medium, planetary atmosphere, and heliosphere provide velocity distribution, thermal and nonthermal properties, turbulence, radiative transfer effects, isotopic ratios and contribution from multiple sources (background emission and coronas). Study of upper planetary atmosphere coronae, plasma process and interaction of the planets with solar winds and solar high energy rotation field.
3. Ideal candidate for low-cost Satellite payload.

1.3.2 Our Tunable SHS system

We can mitigate the limited bandwidth limitation of SHS by building it in tunable configuration or using broadband configuration. The tunable SHS system described in the literature (Dawson et al., 2009) are in all-reflective configurations, which requires a roof mirror and a fold mirror, and hence are suitable for UV missions. In this work, we describe modeling, simulation, and the design of a tunable SHS instrument in a refractive configuration for the optical wavelength regime, where we use a beam splitter for splitting the incoming beam. Hence, the alignment of this instrument is simpler, compared with all-reflective SHS where fold and roof mirrors are in use. This instrument can be used to observe and study faint extended emission line targets by retrieving the high-resolution spectra (with resolving power greater than 20000) from the entire source. Shortly, we will use this instrument to observe the H_α emission lines from Be stars to study their shape and variability. Another science case of this instrument is to monitor the flaring activities of red dwarf stars in $H\alpha$ by looking at the star continuously through a meter-class telescope.

1.4 Pointing system for balloon-borne telescope

Our first balloon experiments were of atmospheric study (Sreejith et al., 2016) where the pointing stability is less critical, but we do plan to observe astronomical sources for which require a pointing mechanism. We have developed some payloads which operate in the near ultraviolet (NUV: 200–400 nm) which we would like to fly on high-altitude balloons (Safonova et al., 2016). We are limited to payloads under 6 kg for regulatory reasons, and this constrains our payload size.

Light balloons are an exceptionally challenging platform for accurate pointing because the platform itself is in constant motion, sometimes with

violent jerks and rotations. Most pointing systems for scientific balloon experiments to date have been designed for the use on large balloons with payload weights of a tonne, or more.

Such systems include SPIDER (Crill et al., 2008), BETTII (Rizzo et al., 2014), BOOMERANG (Crill et al., 2003), BLAST (Pascale et al., 2008) or BLAST-Pol (Fissel et al., 2010). The accuracy of pointing of these systems varies from several arcminutes to few arcseconds. For example, the pointing system in SPIDER has an accuracy of 1° and in BLAST Pol of $30''$; accuracy increasing with weight and complexity of the system.

Attitude control of a balloon platform is a challenging issue. Several techniques like flywheels (Arabash et al., 2010), (Sahnou et al., 2006) are used in balloon platform to obtain a gimbal mechanism are used to point the balloon gondola to a required attitude (elevation and azimuth). In some cases, flywheels are used to control the attitude of the balloon platform. Arabash et al. (2010) describes a method to achieve a particular attitude by changing the angular momentum of each flywheel. Attitude control in BETTII (Benford et al., 2012) is achieved by a multistage control system which has rigid body motion as well as tip-tilt correction mechanism. This system uses two gyros to estimate the attitude of the gondola. They have obtained absolute pointing through a star tracker. BETTII also uses a fringe angle tracker for precise attitude estimation.

In a broad sense, pointing systems for high-altitude balloons consist of four parts: 1. attitude sensors (ASs), 2. actuators, 3. attitude control system, and 4. mechanical structure. In this work, we describe the design and realization of a low-cost light-weight 2-axis correction pointing and stabilization system intended for use in small balloon flights, built entirely using off-the-shelf components. The primary challenge in this development is that its weight must be under 1 kg, given the total mass constraint of 6 kg.

We plan to use this pointing system with other instruments that we are developing. The immediate requirements for accurate pointing come from a light-weight (650 gm) compact star-sensor camera *StarSense* with an ac-

curacy of 30" and 10° field of view (FOV) (Sarpotdar et al., 2017), and a wide-field compact (15 × 15 × 35 cm) NUV imager (Ambily et al., 2016). Both these instruments are developed for use in small balloon payloads, as well as in nanosatellites or CubeSats, and will have a test flight in November 2018.

1.5 Thesis outline

This section comprises of details of each chapter.

Chapter2: Spatial Heterodyne spectrometer concept

This chapter reports the concept of a spatial heterodyne spectrometer (SHS) and elaborates on the basic working principle of the system. A mathematical formulation of the SHS system and the derivation of the parameters of the spectrometer are briefed here.

Chapter3: Simulation of the instrument in Zemax and MATLAB

The simulation of the Tunable SHS system in Zemax, a commercially available ray tracing software is described in the chapter. With the help of this model, we could able to show the detector output of the SHS system under different configurations. Even though the Zemax SHS model gave a fair idea about the system, it would indeed be a tedious process to include a wide range of wavelengths with different intensities with the non-sequential mode that we used for the simulations. Hence we modeled the SHS system in MATLAB- a high level interpreted language to examine SHS performance for a polychromatic input beam and is also explained in this chapter.

Chapter4: Design testing and first light result

In this chapter, we report the design and development of the Tunable SHS instrument. The lab set up of the system, and different tests we have conducted to check the performance of the system, the first light of the instrument and the data obtained are presented in this chapter.

Chapter5: Pointing system for the balloon-borne telescope

This section contains the development of a pointing system for a balloon-borne telescope. This system is developed to observe celestial objects in a balloon-based platform.

Chapter6: Conclusions and Future work

This chapter deals with the summary of the work as well as the future work that can be done.

Chapter 2

Spatial Heterodyne Spectroscopy concept

2.1 Introduction to Fundamentals of SHS

In this chapter, we present the SHS concept, working principle, and the mathematical formulation. Here we also describe the advantages as well as limitations. SHS instruments, like the FTS, share structural similarities with the Michelson interferometer. The primary difference between the two is that in the SHS, the mirrors are replaced with the gratings (G1 and G2 in Fig. 2.1). The position of the gratings is fixed such that the path difference between the two arms is zero, with the tilt of the gratings set for a particular central wavelength called the Littrow wavelength (λ_L). The heterodyne wavenumber is defined as $k_L = 1/\lambda_L$. Wavelengths near the Littrow wavelength form fringes in the detector plane because the grating introduces a tilt on the wavefront proportional to the absolute deviation between the wavelength and the Littrow wavelength, as shown in Fig. 2.1.

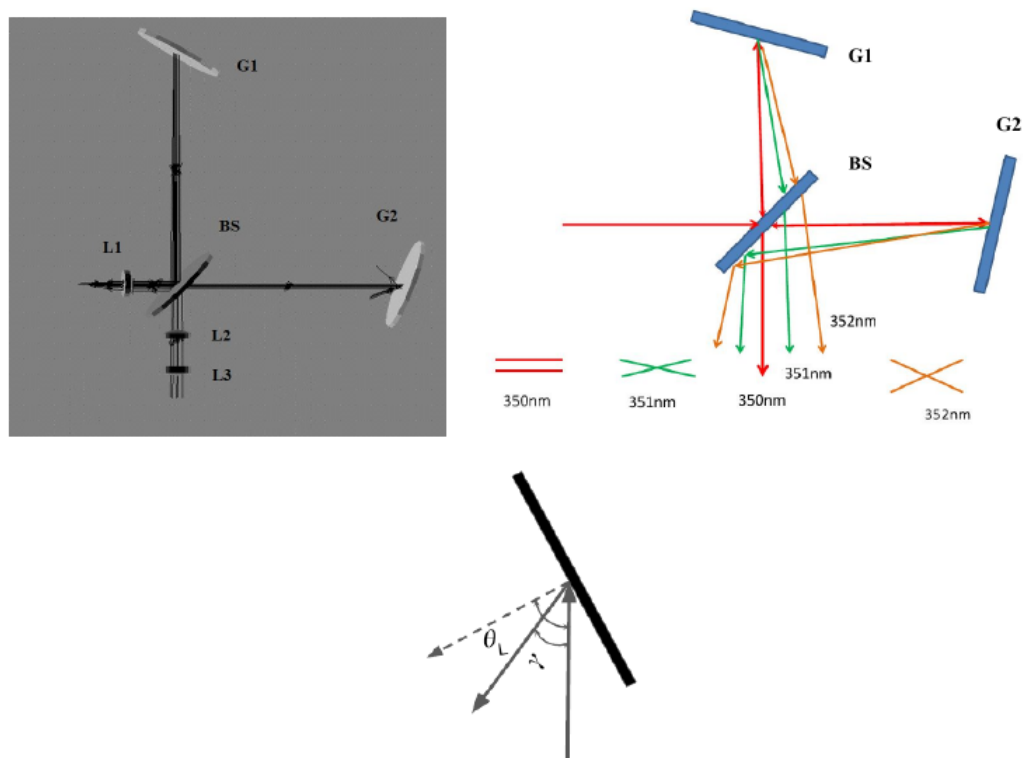


Figure 2.1: *Top Left:* The schematic diagram of the SHS system. L1, L2, and L3 are lenses, G1 and G2 are the gratings, and BS is the beam splitter. *Top Right:* The concept of fringe formation in SHS. The Littrow wavelength 350 nm does not create any fringes because the waves emerge parallel to each other from the two arms of the interferometer. Wavelengths other than Littrow form fringes on the detector because the gratings tilt them. *Bottom:* Zoomed version of one of the gratings.

2.2 Mathematical formulation

In order to understand the system mathematically, we have considered one grating in the SHS configuration (Fig. 2.1, *Bottom*). The relation between the incident ray and the refracted ray can be written using the grating equation,

$$d(\sin \theta_{in} + \sin \theta_{diff}) = m\lambda, \quad (2.1)$$

where d is the pitch of the grating, θ_{in} is the incident angle, θ_{diff} is the diffracted angle, m is the order of grating, and λ is the wavelength of the

light. Hence, for the grating shown in Fig. 2.1, *Bottom*, the equation becomes

$$d(\sin\theta_L + \sin(\theta_L - \gamma)) = m\lambda, \quad (2.2)$$

where θ_L is the Littrow angle for the wavelength λ_L , and γ is the angle between the incident and diffracted light. The incident beam and the diffracted beam follow the same path in the Littrow configuration, and $\gamma = 0$. Eq. 2.2 then becomes Eq. 3.1, which gives the relation between Littrow wavelength and Littrow angle,

$$\sin(\theta_L) = \frac{m}{2k_L d}, \quad (2.3)$$

where $k_L = 1/\lambda_L$ is the wavenumber in cm^{-1} . Expanding the sine terms in Eq. 2.2 using the small angle approximation for γ ($\sin\gamma = \gamma$, $\cos\gamma = 1$), and eliminating d and m using Eq. 3.1, we obtain

$$\sin(\theta_L) + \sin(\theta_L)\cos(\gamma) + \sin(\gamma)\cos(\theta_L) = m\lambda \quad (2.4)$$

$$\sin(\theta_L) + \sin(\theta_L) + \gamma\cos(\theta_L) = \frac{m}{k} \quad (2.5)$$

$$\gamma = \frac{2(k - k_L)\tan(\theta_L)}{k}, \quad (2.6)$$

where $k = 1/\lambda$ is the wavenumber in cm^{-1} . If two beams with the wavelength $1/k$, tilted at angles γ and $-\gamma$, respectively, are made to interfere each other, they will produce a fringe pattern with a spatial frequency of $2k\sin\gamma$. Thus, the frequency of the fringe pattern is (in small angle approximation of γ)

$$f_x = 2k\sin\gamma = 4(k - k_L)\tan(\theta_L), \quad (2.7)$$

where f_x is the frequency of the fringes known as the Fizeau fringe frequency. In interferometers, the intensity pattern and the fringe frequency are related through the following equation, where x is the pixel position along the X

axis of detector, considering detector is in XY plane,

$$I(x) = I(1 + \cos(2\pi f_x x)) . \quad (2.8)$$

Equation. 2.8 shows no differentiation between wavelengths that are lower or higher than heterodyne wavelength since the interference pattern depends upon $|k - k_L|$. The degeneracy in estimating whether the wavelength is bluer or redder than the Littrow wavelength can be mitigated by slightly tilting the grating by an angle $\frac{\phi}{2}$ in a direction perpendicular to the plane of interference, which creates a vertical fringe pattern with frequency (Dawson et al., 2009) $f_y = \phi k$ and has a dependency on wavelength. Section 3.2.3 details about this with a simulation.

Therefore, the fringe pattern can be represented as a function of x and y for SHS system as in Eq. 2.15. For the more general case, where the incoming wave consists of more than one wavenumber, we use Eq. 2.10,

$$I(x) = B(1 + \cos[8\pi(k - k_L) \tan \theta_L x + 2\pi\phi ky]) , \quad (2.9)$$

$$I(x) = \int_{-\infty}^{\infty} B(k) (1 + \cos[8\pi(k - k_L) \tan \theta_L x + 2\pi\phi ky]) dk . \quad (2.10)$$

Eq. 2.10 indicates that the intensity distribution on the detector is the Fourier cosine transform of the spectra. Hence, the spectra can be retrieved by taking the inverse Fourier cosine transform of the generated interferogram. Assuming $\phi = 0$, the eq. 2.10 can be rewritten as eq. 2.11

$$I(x) = 2 \int_0^{\infty} B(k) dk + 2 \int_0^{\infty} B(k) \cos[8\pi(k - k_L) \tan \theta_L x] dk \quad (2.11)$$

The intensity of the central fringe can be found by equation $x = 0$ as in eq. 2.12

$$I(0) = 4 \int_0^{\infty} B(k) dk \quad (2.12)$$

The eq. 2.11 can be then rewritten as in eq. 2.13.

$$I(x) - 0.5I(0) = 2 \int_0^{\infty} B(k) \cos [8\pi(k - k_L) \tan \theta_L x] dk . \quad (2.13)$$

Taking the Fourier transform relation

$$B(k) = 2 \int_0^{\infty} (I(x) - 0.5I(0)) \cos [8\pi(k - k_L) \tan \theta_L x] dx . \quad (2.14)$$

In eq. 2.12, x does not take value from zero to infinity, since the size of the detector is limited. Hence the eq. 2.12 can be modified by limiting the value of x from 0 to x_{max} , the size of the detector. Thus what we obtain is $B_c(k)$ which is

$$B_c(k) = 2 \int_0^{x_{max}} (I(x) - 0.5I(0)) \cos [8\pi(k - k_L) \tan \theta_L x] dx . \quad (2.15)$$

Substituting the eq. 2.13 in eq. 2.15

$$B_c(k) = 4 \int_0^{x_{max}} \int_0^{\infty} B(k') \cos [8\pi(k' - k_L) \tan \theta_L x] dk' \cos [8\pi(k - k_L) \tan \theta_L x] dx \quad (2.16)$$

$$B_c(k) = \int_0^{\infty} B(k') R(k', k, x_{max}) dk' \quad (2.17)$$

where $R(k', k, x_{max})$ is given in eq. 2.18 and applying trigonometric product formula it changes into eq. 2.19.

$$R(k', k, x_{max}) = 4 \int_0^{x_{max}} \cos [8\pi(k' - k_L) \tan \theta_L x] \cos [8\pi(k - k_L) \tan \theta_L x] dx \quad (2.18)$$

$$= 2 \int_0^{x_{max}} \cos [4\pi(k' + k - 2k_L) \tan \theta_L x] + \cos [4\pi(k' - k) \tan \theta_L x] dx .(2.19)$$

Integrating the eq. 2.19 and applying the limit and multiplying and dividing by x_{max} the equation becomes as eq. 2.20

$$= 2x_{max} \left[\frac{\sin [4\pi(k' + k - 2k_L) \tan \theta_L x_{max}]}{4\pi(k' + k - 2k_L) \tan \theta_L x_{max}} + \frac{\sin [4\pi(k' - k) \tan \theta_L x_{max}]}{4\pi(k' - k) \tan \theta_L x_{max}} \right] (2.20)$$

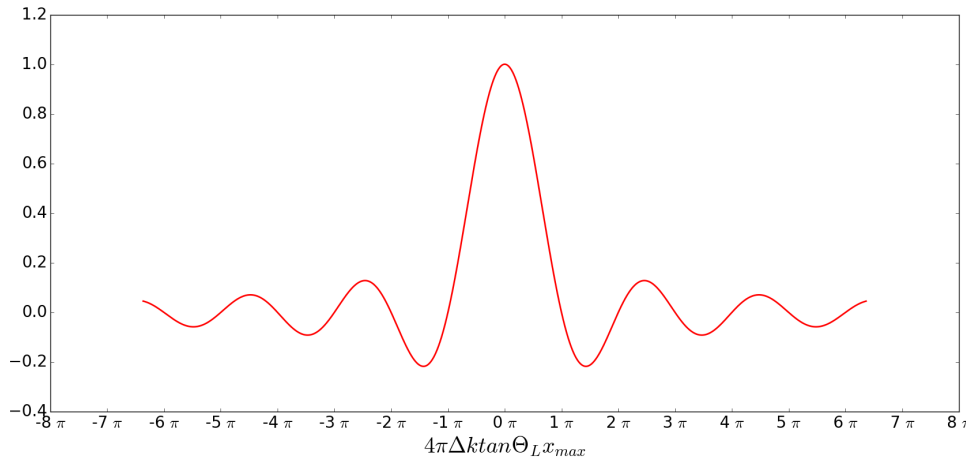


Figure 2.2: A sinc function

Equation. 2.20 represents the addition of two sinc function. The first minimum of sinc function (refer Fig. 2.2) in the second part of eq. 2.20 occurs when

$$4\pi(k' - k) \tan \theta_L x_{max} = \pi \quad (2.21)$$

but $x_{max} = W \cos(\theta_L)$ (Fig. 2.3, and $k' - k = \Delta k$, substituting this in eq. 2.21,

$$4\Delta k W \sin(\theta_L) = 1 \quad (2.22)$$

where W is the illuminated grating width. The resolving power (R) of the system is defined by $R = \frac{k_L}{\Delta k}$. Hence the eq. 2.22 can be modified as

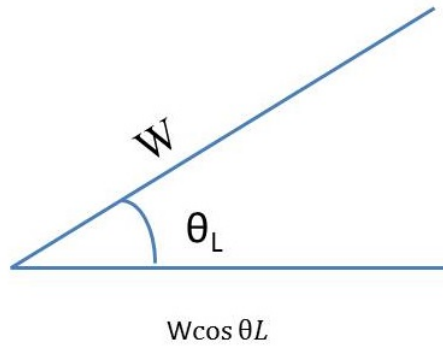


Figure 2.3: The image of the grating with W as illuminated area. On the detector this area gets reduced to $W \cos \theta_L$. Hence x_{max} is $W \cos \theta_L$.

$$R = 4k_L W \sin(\theta_L) \quad (2.23)$$

Substituting eq. 3.1 in eq. 2.23 then R becomes as

$$R = \frac{2 \times m \times W}{d}, \quad (2.24)$$

Hence it is clear from the eq. 2.24 that the resolving power of the SHS system depends on the illuminated grating width W , the order of the grating m and pitch of the grating d

2.2.1 Limitations of SHS

The SHS has advantages over a grating and Fourier transform spectrometers such as compactness, sensitivity, and ruggedness. SHS does not have any slits allowing the instrument to collect more light. Therefore the sensitivity of the instrument is high compared to grating spectrometers. Thus, this instrument is suited well for studies of faint extended sources. Since the resolving power of SHS depends on the illuminated grating width, grating groove density and order of the grating (Eq. 4.1), larger optics (to accommodate large beam width and higher orders) or gratings with higher groove density are needed for higher resolving power. Such high resolving power narrows the observable

bandpass, which another disadvantage. For example: if the resolving power of the SHS instrument is 24000 at the heterodyne wavelength of 650 nm, then the resolution ($\Delta\lambda$) of the instrument is 0.027 nm (650/24000). Therefore, an input beam having an absolute wavelength deviation $p\Delta\lambda$ from the Littrow wavelength (here 650 nm) should produce p fringes, where p is an integer. If a 1024×1024 detector is used to image the fringes, then from the Nyquist criteria the maximum number of fringes imaged is 512. Therefore the bandpass of SHS is

$$BW = 2 \times \Delta\lambda \times N, \quad (2.25)$$

Where BW is the bandwidth in nm, and N is the number of fringes. Hence, the bandwidth of the above configuration is 27 nm. This limitation of the SHS can be mitigated by either using a tunable SHS (Hosseini et al., 2012) (TSHS), or a Multi-Order SHS (Harlander et al., 2010).

2.3 Summary

In this chapter, we discussed the fundamental concepts of the spatial heterodyne spectrometer (SHS). We have also described the system mathematically and derived the equation for resolving power of the instrument. We briefly reported the limitations of SHS instrument and how these limitations can be mitigated.

Chapter 3

Simulation of SHS system in Zemax and MATLAB

Nirmal K, Sridharan Rengaswamy, Sripadmanaban Nadar Sriram, Jayant Murthy, et al., J. Astron. Telesc. Instrum. Syst. 4(2) 025001 (17 May 2018)

3.1 Introduction

This chapter provides an overview of the simulations and mathematical modeling we have done. These models are used to study various aspects of the system which in turn helped us in finalizing the components.

3.2 Modeling of SHS system in Zemax[®]

We have modeled a tunable SHS (Fig. 3.1) using Zemax[®]. The model includes a beam splitter (BS) where half the light is transmitted, and half reflected, two holographic gratings (G1, G2) of groove density (1/pitch) 1200 lines/mm, and a detector (D) of size 12 mm × 12 mm with 512×512 pixels. Initially, the gratings are tilted to a Littrow angle of 15.6643°, which corresponds to a Littrow wavelength of 450 nm. The collimated beam of 10

mm diameter is allowed to fall on the beam splitter. The reflected and the transmitted beams are incident on the gratings G1 and G2, respectively, and are combined after leaving the beam splitter. Since the incoming beam has only one wavelength of 450 nm, there are no fringes on the detector (Fig. 3.2, middle panel) as there is no path difference between the rays coming from two arms of the SHS instrument.

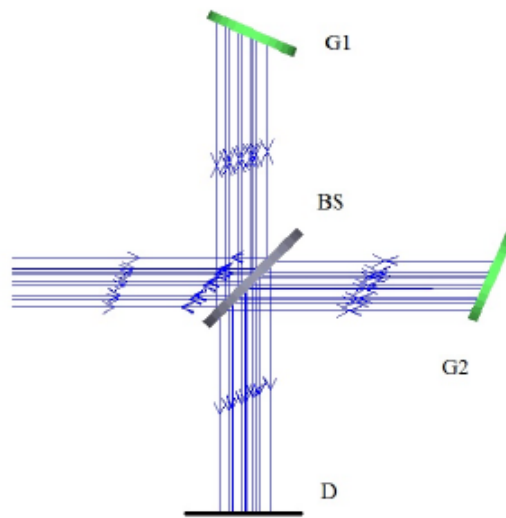


Figure 3.1: A conceptual diagram of a tunable SHS modeled in Zemax[®]. G1, G2 are the gratings, BS is the beam splitter, and D is the detector.

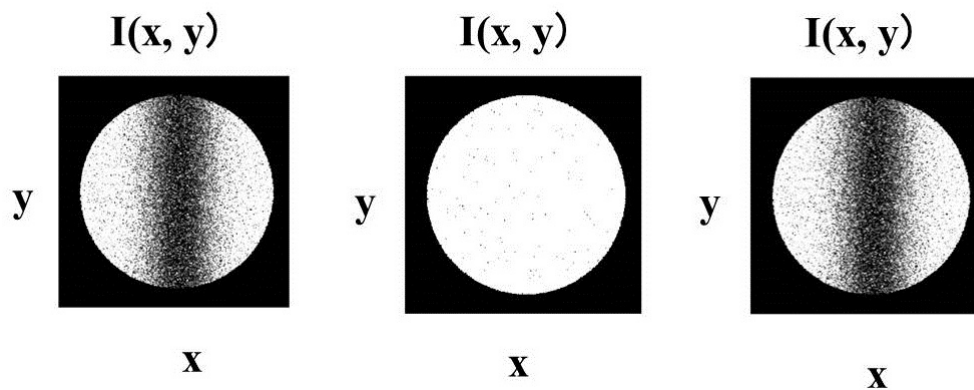


Figure 3.2: The simulated detector view: generated interferogram in x and y positions, $I(x, y)$ is displayed when the incoming beam constituted of only the wavelength 450.0187 nm (*Left*), 450 nm (Littrow) (*Middle*) and 449.981 nm (*Right*). The size of the detector is 12 mm \times 12 mm, having 512 \times 512 pixels. The white circular patch (10 mm beamwidth) is the illuminated area of the detector. These images have been processed to enhance the fringe contrast.

In this configuration, the resolving power R of the system (Eq.1.24) is 24000, which means that one fringe is generated on the detector for a change of 0.0187 nm ($\frac{450}{24000}$) in the wavelength. In order to verify this, we changed the incoming wavelength to 450.0187 nm in Zemax[®] model and obtained one fringe (Fig. 3.2, *Left*) on the detector. Similarly, the other fringe is generated on the detector at 449.981 nm (Fig. 3.2, *Right*).

3.2.1 Tunable SHS

Tuning for different wavelengths in the TSHS is carried out by tilting the grating for different Littrow configurations; i.e. changing the Littrow wavelength (central wavelength of the bandwidth). The relation between the Littrow angle and the Littrow wavelength is given by Eq. 3.1, where θ_L is the Littrow angle, $k_L = 1/\lambda_L$ is the wavenumber in cm^{-1} , m is the grating order, d is the grating groove density.

$$\sin(\theta_L) = \frac{m}{2k_L d}, \quad (3.1)$$

We have found the Littrow angle for different heterodyne wavelengths for the grating we have used (holographic grating 1200 lines/mm), and plotted in Fig. 3.3. In the Zemax[®] model, we tilted the grating for different Littrow configuration and obtained the fringes.

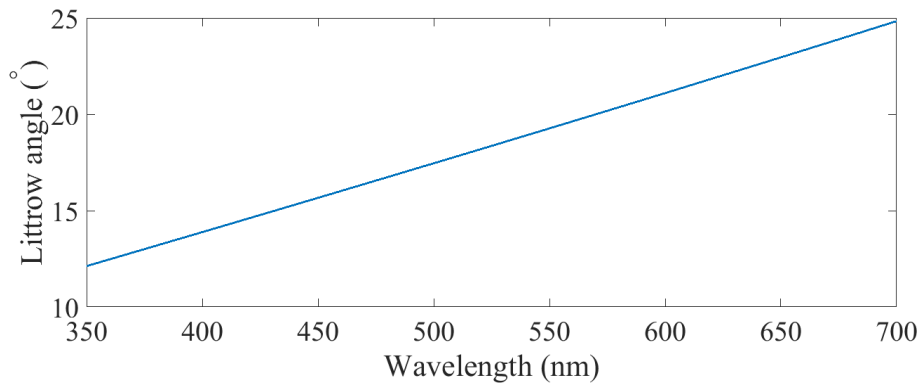


Figure 3.3: The relation between the Littrow angle and wavelength for the holographic grating with 1200 lines/mm.

3.2.2 Tunability of the system

In order to check the tunability of the TSHS system, the Littrow angles of gratings G1 and G2 were changed to 19.269° , which corresponds to a Littrow wavelength of 550 nm. Since all other configurations were the same, one fringe should be obtained on the detector at a wavelength change of 0.023 nm. Fig. 3.4 (*Middle*) shows the detector view for a Littrow wavelength of 550 nm, with the images for wavelengths of 549.977 nm and 550.023 nm shown on left and right, respectively.

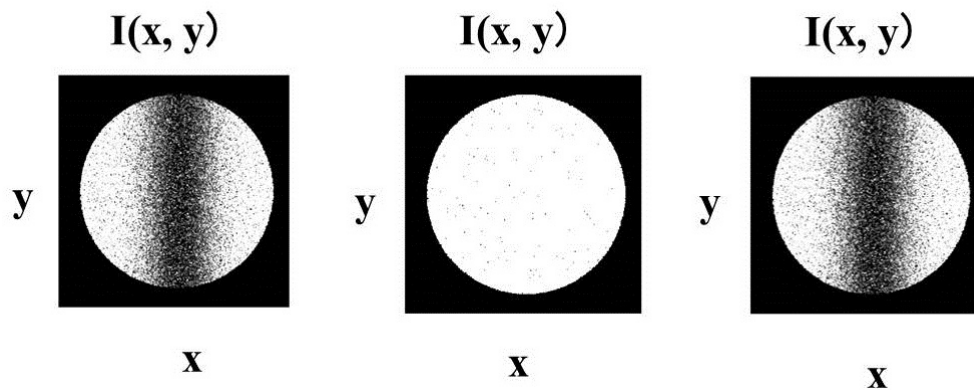


Figure 3.4: Simulated detector view: generated interferogram in x and y positions, $I(x, y)$ is displayed when the input beam constitutes only the wavelength 549.977 nm (*Left*), 550 nm (Littrow) (*Middle*) and 550.023 nm (*Right*). The size of the detector is 12 mm \times 12 mm, having 512 \times 512 pixels. The white circular patch (10-mm beamwidth) is the illuminated area of the detector. These images have been processed to enhance the fringe contrast.

3.2.3 Identifying the wavelength

Wavelengths on either side of the Littrow wavelength will generate interferograms with the same spatial frequency: the same number of fringes will be formed by the wavelengths $\lambda_o + \Delta\lambda$ and $\lambda_o - \Delta\lambda$ (Fig. 3.2). Hence, it is essential to differentiate between fringes formed by $\lambda_o + \Delta\lambda$ and $\lambda_o - \Delta\lambda$. This can be done by tilting the grating in a direction perpendicular to the direction of Littrow angle. This arrangement creates fringes aligned in different direction as in Fig. 3.5 for $\lambda_o + \Delta\lambda$ and $\lambda_o - \Delta\lambda$.

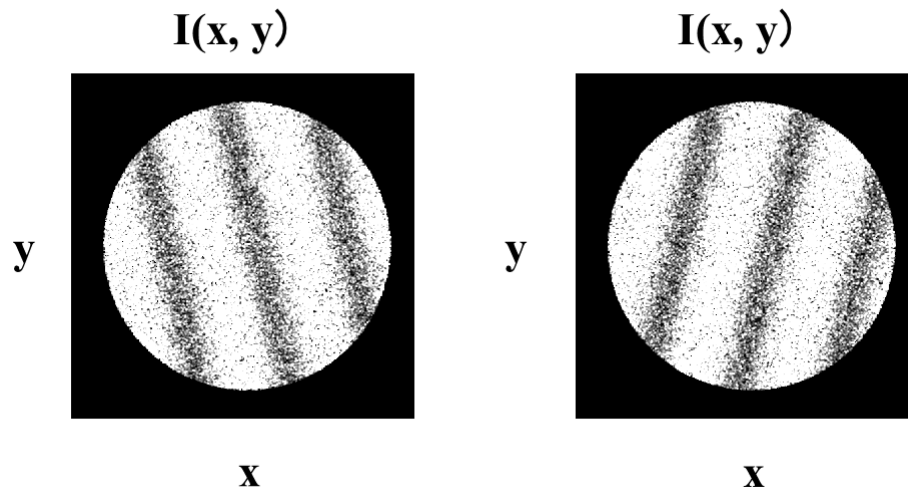


Figure 3.5: Simulated fringes obtained for wavelength 450.0562 nm (*Left*) and for 449.944 nm (*Right*), when the grating G1 is tilted 0.001° in the direction perpendicular to the Littrow angle. The Littrow wavelength for this setup is 450 nm. These images have been processed to enhance the fringe contrast.

3.3 Interferogram with more than one emission line

A set of the interferogram is generated in the SHS corresponding to each resolution element. Resolution element is the minimum wavelength that can be resolved by the instrument. Hence if the input source has two strong emission lines, then two sets of interferograms are generated. On the detector, it is seen as the superposition of two interferograms. If the source contains many resolution elements, the fringe visibility also reduces depending upon the number of interferograms generated. We have simulated this condition in Zemax. We assumed the source contains two emission lines having the same intensity at 650.1nm and 650.3nm as shown in Fig. 3.7. The interferogram for each line is separately simulated in Zemax as shown in Fig. 3.6. In this simulation, the Littrow wavelength was selected as 650nm which corresponds to a Littrow angle of 35.803 degrees for a holographic grating having groove density 1800 lines/mm. We also introduced a tilt of 0.01 degree to one of the gratings in a direction normal to the Littrow angle. The beam-width or the

part of the grating illuminated by the incoming light was fixed as a circular region of 8mm diameter. In the same configuration, we then input a source having both the emission lines. The interferograms generated on the detector are shown in Fig. 3.8. Figure. 3.8, Left shows the interferogram generated on the detector if the gratings do not have any tilt in any other direction other than Littrow angle. However a more realistic case is shown in Figure. 3.8, Right, where one of the gratings has a tilt in a direction perpendicular to Littrow angle tilt.

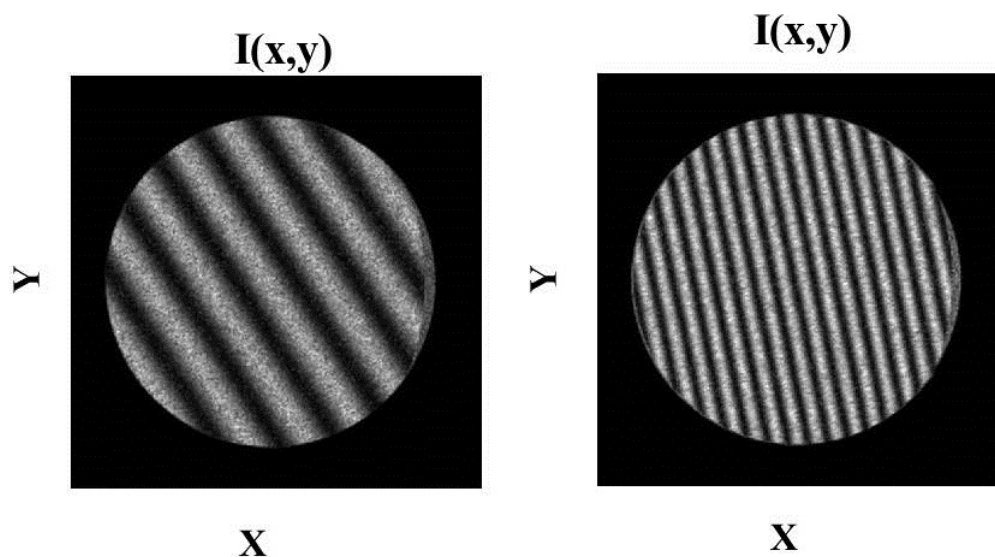


Figure 3.6: Simulated detector view: generated interferogram in x and y positions, $I(x, y)$ is displayed when the input beam constitutes of wavelength 650.1 nm (*Left*), and 650.3 nm (*Right*). The size of the detector is 10 mm \times 10 mm, having 512 \times 512 pixels. The white circular patch (8-mm beamwidth) is the illuminated area of the detector.

An enlarged version of the two dimensional Fourier transform of the Fig. 3.8, Right is shown in Fig. 3.9. The central bright spot corresponds to the zero frequency value and the other two spots on the right of zero frequency corresponds to the emission line strength of 650.1nm and 650.3 nm respectively and the two spots left of zero frequency value are the corresponding negative frequencies.

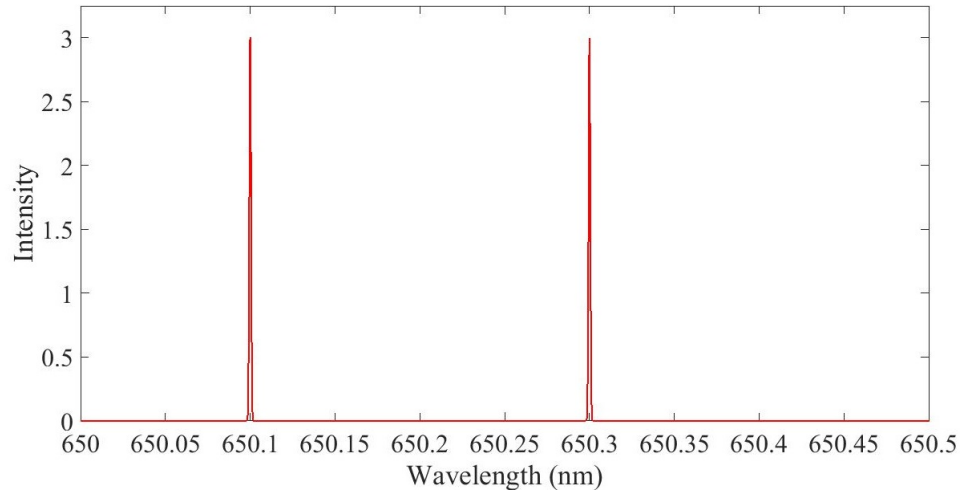


Figure 3.7: A pictorial representation of the spectrum input to the Zemax simulation.

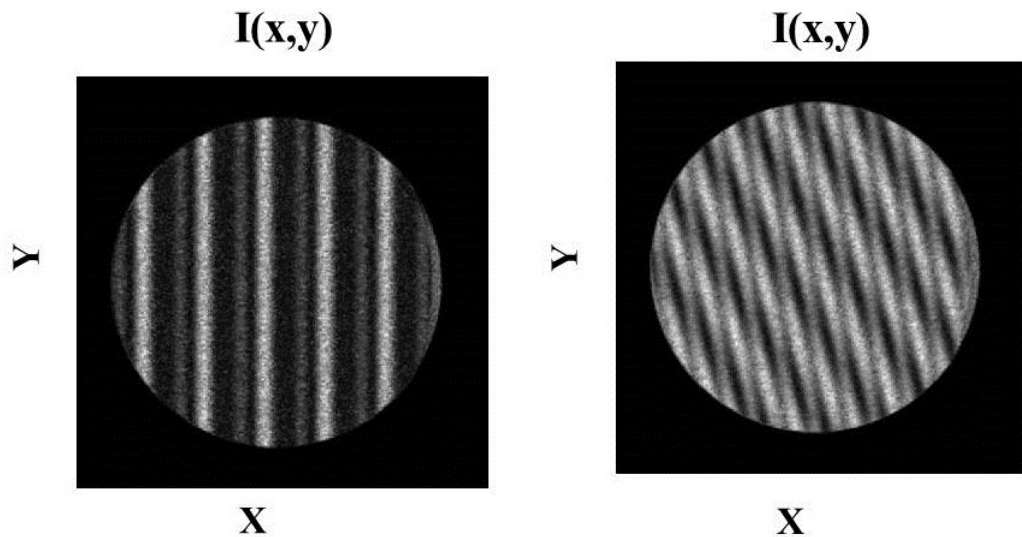


Figure 3.8: Simulated detector view: generated interferogram in x and y positions, $I(x, y)$ is displayed when the input beam constitutes of wavelength 650.1 nm and 650.3 nm. *Left* shows when the gratings doesn't have any tilt other than Littrow angle and *Right* shows when of the grating has a tilt of 0.01 degrees in a direction perpendicular to the littrow angle. The size of the detector is 10 mm \times 10 mm, having 512 \times 512 pixels. The white circular patch (8-mm beamwidth) is the illuminated area of the detector.

3.4 Simulation of SHS system in MATLAB

Even though the Zemax SHS model gave a fair idea about the system, it would indeed be a tedious process to include a wide range of wavelengths with different intensities with the non-sequential mode that we used for the simulations. Hence we modeled the SHS system in MATLAB- a high level

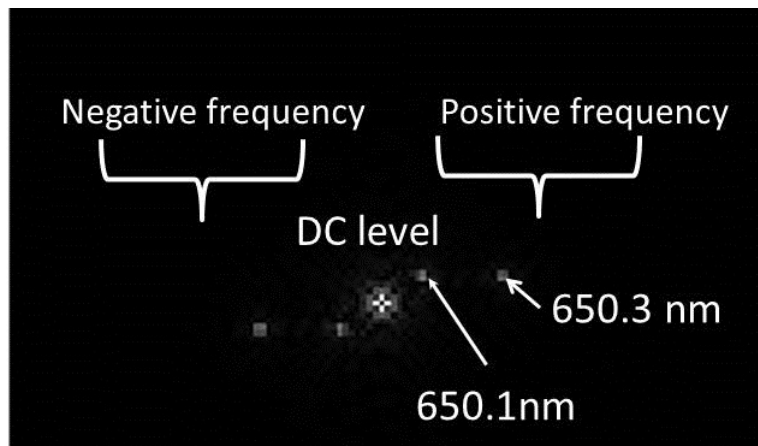


Figure 3.9: An enlarged version of the FFT of the interferogram generated for emission lines 650.1nm and 650.3nm (Fig. 3.8, Right). The central bright spot corresponds to the zero frequency value and the other two spots on the right of zero frequency corresponds to the emission line strength of 650.1nm and 650.3 nm respectively and the two spots left of zero frequency value are the corresponding negative frequencies

interpreted language to examine SHS performance for a polychromatic input beam. Figure. 3.10 shows the different blocks in SHS model (Perkins et al. (2013)). This model takes a spectrum provided by the user and generates an interferogram considering the system parameters.

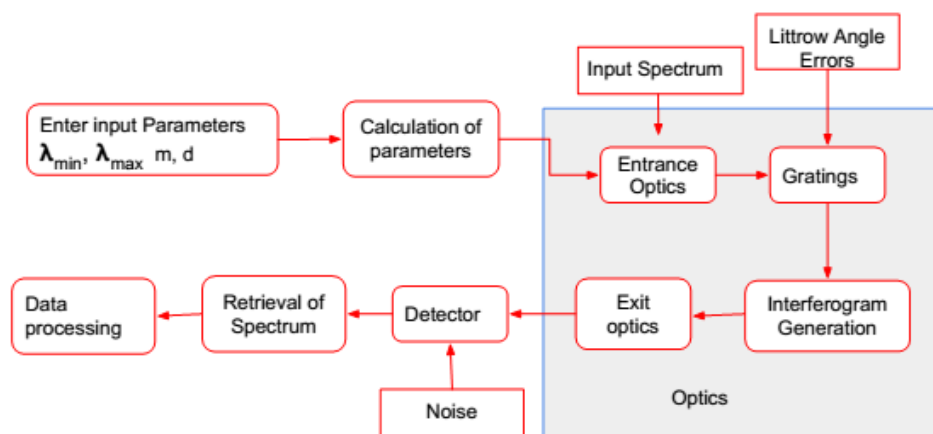


Figure 3.10: The block diagram representing the simulated model of SHS in MATLAB.

The spectrum, for which the interferogram is to be calculated is given to the first block in the SHS model, which also takes parameters such as wavelength extremes of the spectrum (λ_{min} , λ_{max}), the order of the grating m and the pitch of the grating d . The model then calculates the Littrow angle

for this range of wavelength using the equation. 3.1 by assuming λ_{min} as Littrow wavelength the block in Fig. 3.10 calculation of parameters indicate it. The entrance optics block in the model considers the effect of field of view (FOV) and the transmission of entrance optics on the input spectrum as in eq. 3.2.

$$B'(k) = \Omega \times T_1(k) \times B(k) \quad (3.2)$$

Where (Ω) is the FOV, $T_1(k)$ is the transmission, $B(k)$ and $B'(k)$ are the sampled spectrum and output respectively.

The loss of signal strength due to the effect of grating efficiency (eq. 3.3) is calculated in the grating block.

$$B''(k) = 1/2 \times \eta B'(k) \quad (3.3)$$

where $B''(k)$ the output spectra after considering the grating efficiency η .

An interferogram is generated in the interferogram generation block (eq. 3.4) and the effect of exit optics (eq. 3.5) on the generated interferogram is considered in exit optics block.

$$I(x) = \sum_{k=1}^{\infty} (B(k)(1 + \cos[8\pi(k - k_o)x \tan(\theta_L)]))dk \quad (3.4)$$

$$I'(x) = \Omega \times T_2(k) \times I(x) \quad (3.5)$$

Where $T_2(k)$ is the exit optics transmission.

In our model, we gave different spectrum profiles and obtained corresponding interferograms. We used a Gaussian profiles having different FWHM as our spectrum profiles and obtained interferogram corresponding to the

spectrum profile. Figure. 3.11, The left panel shows the spectrum input to the SHS model Figure. 3.11, Right shows the generated interferogram. Figure. 3.11 indicate that the FWHM of the spectrum becomes narrower fringes are formed more area of the illuminated region.

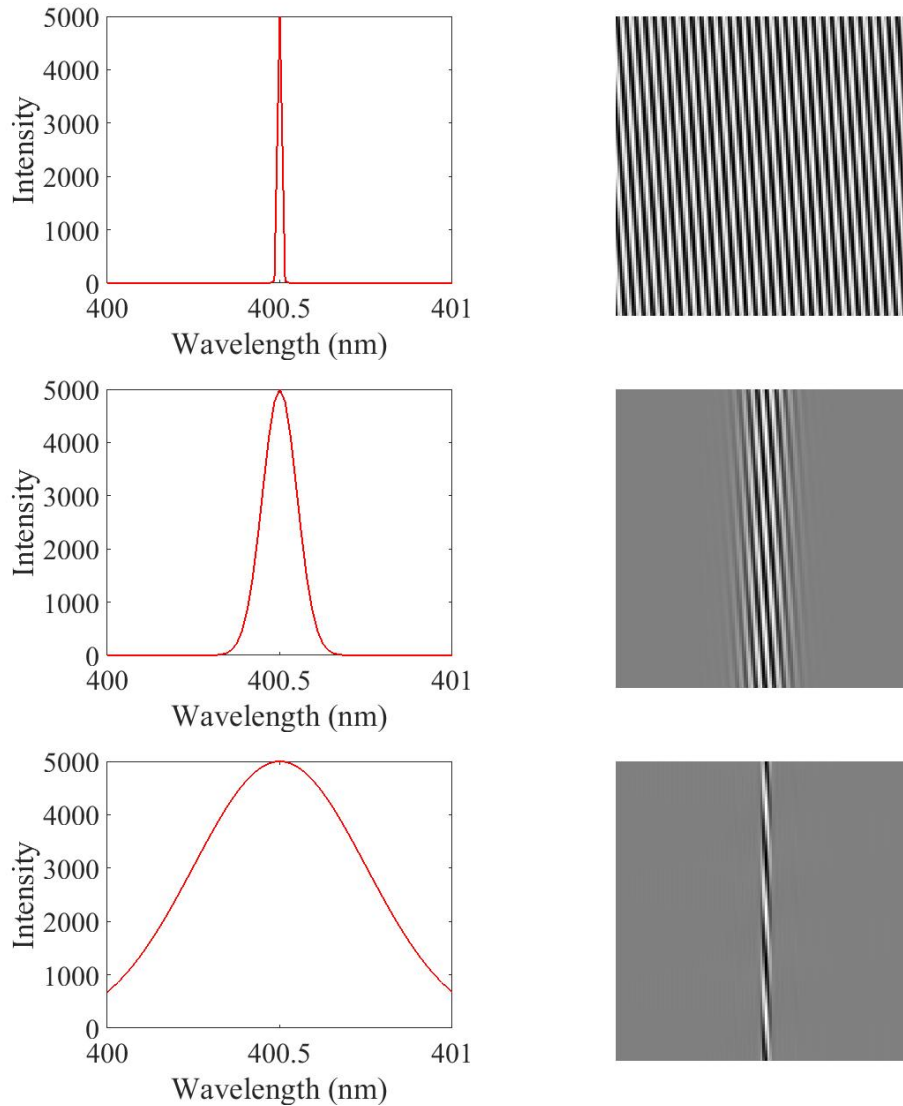


Figure 3.11: *Left:* The spectrum profiles that is fed to the system. The spectrum profiles are Gaussian function having different FWHM. Top left panel shows an emission line with FWHM of 0.005nm, Middle left panel shows an emission line with FWHM 0.05 nm, and bottom left panel shows an emission line with FWHM of 0.25nm. The simulated detector view corresponding to each spectrum profile is shown in the right panel.

3.5 Summary

This chapter reports the simulation and mathematical modeling of the SHS system in Zemax[®] as well as MATLAB. We used this model to study the performance of the SHS instrument under different conditions like how the spectral bandwidth effects the interferogram which we used for the wavelength calibration of the instrument.

Chapter 4

Design Testing and First Light results

Nirmal K, Sridharan Rengaswamy, Sripadmanaban Nadar Sriram, Jayant Murthy, et al., J. Astron. Telesc. Instrum. Syst. 4(2) 025001 (17 May 2018)

4.1 Introduction

In this chapter, we describe the design and the following laboratory setup of the instrument. After integrating the instrument, we tested it using different lamps such as sodium vapor lamp, hydrogen lamp, and Helium lamp. We have checked the effect of line broadening on the interferogram using a continuum source–Halogen lamp and monochromator setup. We have commissioned the instrument at Vainu Bappu Telescope (VBT) of the Vainu Bhappu Observatory (VBO)^a. The first light was on 19th March 2018. We observed *Sirius* and *Betelgeuse* in H_α region of the electromagnetic spectrum. We have presented the first light results in this chapter.

^a<https://www.iiap.res.in/centers/vbo>

4.2 Design considerations of a tunable SHS

Our TSHS system is designed to work as the back-end instrument for a ground-based telescope in the spectral regime between 350 nm to 700 nm. We have commissioned this instrument at the 2.34-m VBT, Kavalur, India. The F -ratio of the beam at the prime focus of the telescope is 3.25, and the light is collected from the prime focus and fed to our system through a 100 μm diameter optical fiber. We selected two holographic gratings of pitch (d) as 1/1200 lines per mm for the system. The maximum theoretical resolving power of the system was fixed to be 24000, which requires the width of the grating to be illuminated as 10 mm for order $m = 1$ (c.f. Eq. 4.1).

$$R = \frac{2 \times m \times W}{d}, \quad (4.1)$$

4.2.1 Entrance Optics and Collimation

As the minimum expected size of the beam on the grating was 10 mm, we fixed 10 mm as our beam width at the entrance optics, thereby accounting for the beam divergence. The F -ratio of the incoming beam is ~ 3 , and the focal length f of the collimating lens is found as follows,

$$f = F\# \times \Phi \quad (4.2)$$

$$f = 3 \times 10 = 30 \text{ mm},$$

where $F\#$ is the F -ratio of the incoming beam, and Φ is the diameter of the collimated beam.

4.2.2 Gratings and beam splitter

We used a one-inch grating operating in the first order (± 1) since the size of the beam is fixed at 10 mm. A cube beam splitter of $40 \times 40 \times 40$ mm size is selected accounting the divergence of the beam.

4.2.3 Exit Optics

The fringe localization plane (FLP) is where the interference fringes viewed with maximum clarity. Hence, at this plane, the fringes can be obtained at maximum contrast. The distance z_0 of the FLP from the beam splitter is found using Eq. 4.3 as in Hosseini et al. (2015), where L is the average optical path inside the TSHS.

$$z_0 = \frac{L}{2 \cos^2(\theta_L)}, \quad (4.3)$$

The position of the FLP depends on the source as well as on the instrument. The FLP of a point source is unlocalized and has greater contrast, compared with the FLP of an extended source which is localized with less visibility. The exit optics re-images the FLP onto the detector. We have kept the exit optics on a linear stage whose position can be changed to obtain clear fringes on the detector. The diameter of the beam at the FLP is same as the illuminated grating width. Therefore, a standard 25-mm aperture lens with 50 mm focal length is selected to re-image FLP onto the detector. Our selected components are listed in Table 4.1, and we have completed a lab setup of the system on an optical breadboard (Fig. 4.2).

4.3 Alignment of the instrument

Initially, we aligned the spectrograph with a diode laser of wavelength 650nm. The laser is mounted on a two-axis tip-tilt stage and checked whether the system has any tip or tilt by marking the beam position closer to the laser diode and far away from the laser diode. If there is a tip or tilt in the arrangement, then the spot position varies depending on the screen position. We have adjusted the tip-tilt of the laser mount in such a way that the spot positions remains the same whether the screen is nearby or far away. The entrance optics (the collimating lens) is aligned next. The lens is fixed on a tip-tilt correction mount for the adjustment. The beamsplitter is mounted on the optical breadboard and ensured the mount does not have

Table 4.1: The components procured for building TSHS instrument.

Components	Description
Grating	Holographic gratings, 1200 lines/mm visible (bare aluminum coating)
Beam splitter	Standard cube beam splitter (50:50) 40 × 40 × 40 mm
Rotational stages	Newport URS50BPP 0.00022° resolution 0.0005° minimum incremental motion.
Detector	Sony IMX249 CMOS camera 1920 × 1200 8-bit camera 5.86 × 5.86 μm pixels
Entrance optics	convex lens $f = 30$ mm 10 mm diameter
Exit optics	convex lens $f = 50$ mm 25 mm diameter

any tip or tilt. The transmission path and reflection path of the beamsplitter is identified using a screen. The rotational stages are fixed on the reflecting and transmitting path, and a tip-tilt correction system is mounted on these rotational stages. The gratings are mounted on the tip-tilt mount, and the rotational stages are homed such a way that the laser beam normally falls on the grating. At this position grating merely acts as a mirror and reflects the beam back. A re-imaging lens and a screen are then placed on a rail on the other end of the beamsplitter. An interferogram is obtained on the screen. The rotational stage is then adjusted to the Littrow angle corresponding to 650 nm which corresponds to the wavelength of the diode laser. Another interferogram (refer Fig. 4.1) is obtained on the screen. The fringe frequency can be adjusted by adjusting the tip-tilt stage of the grating or the angle of the rotational stage. By changing the rotational stage angle, the system can be aligned to another central wavelength. However, we used a hydrogen lamp and Helium lamp to test the tunability of the system. These two lamps have distinct emission lines in the visible region of the electromagnetic spectrum. For the observation, we used a hydrogen lamp and aligned the system for H_α

emission line.

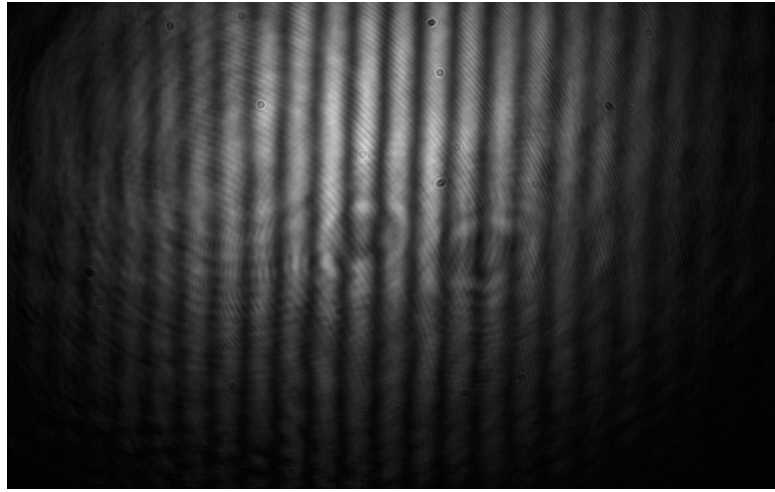


Figure 4.1: Raw fringes obtained for a laser diode of wavelength 650nm.

4.4 Experimental setup and first results

We have used a sodium vapor lamp as our source with the sodium D lines at 589 nm and 589.6 nm and tuned the system to those wavelengths. The light from the source is fed to our TSHS system through an optical fiber cable of core diameter 100 μm .

Since the source contains two emission lines, the interferogram also contained fringes of two different spatial frequencies as can be seen in Fig. 4.3. However, the first fringe we obtained of reduced visibility (refer Fig. 4.3) and the fringes were localized. We have suspected two reason behind this: first due to a mismatch in the path length between two arms, second due to the poor imaging of the Fringe localization plane. Therefore we have introduced a linear stage in each arm of the TSHS to adjust the grating position as well as the OPD. A liner stage is also introduced at the imaging section to adjust the imaging lens and detector position. The final result obtained after making these changes can be seen in Fig. 4.5, where the fringe visibility is improved, and the fringes are contained in the entire area of the beam width.

The spectrum is retrieved by applying a two-dimensional Fourier trans-

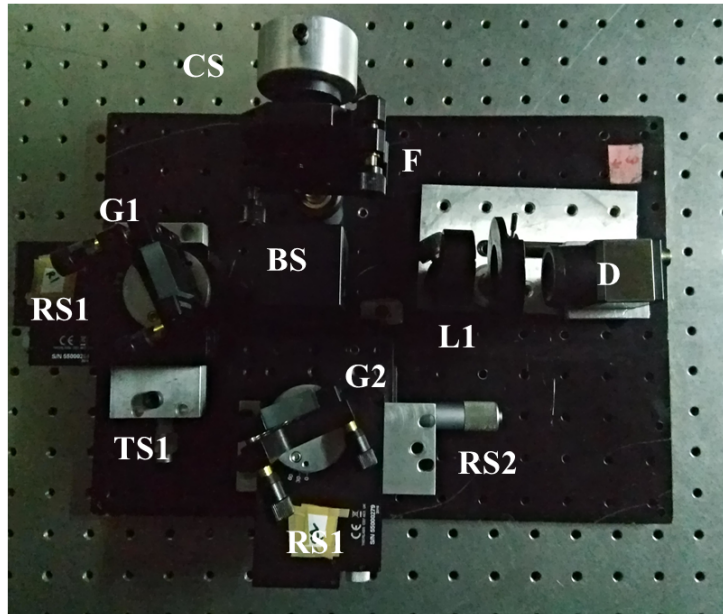


Figure 4.2: The TSHS setup arranged on a bread board (top view). CS is the collimator setup, F is the filter, L1 is the imaging lens, BS is the beam splitter, D is the detector, RS1 and RS2 are the rotational stages, and TS1, TS2 are the translational stages.

form (Fig. 4.4) on the interferogram. The spectrum is shown in Fig. 4.5 is obtained by taking a line cut of the two-dimensional interferogram.

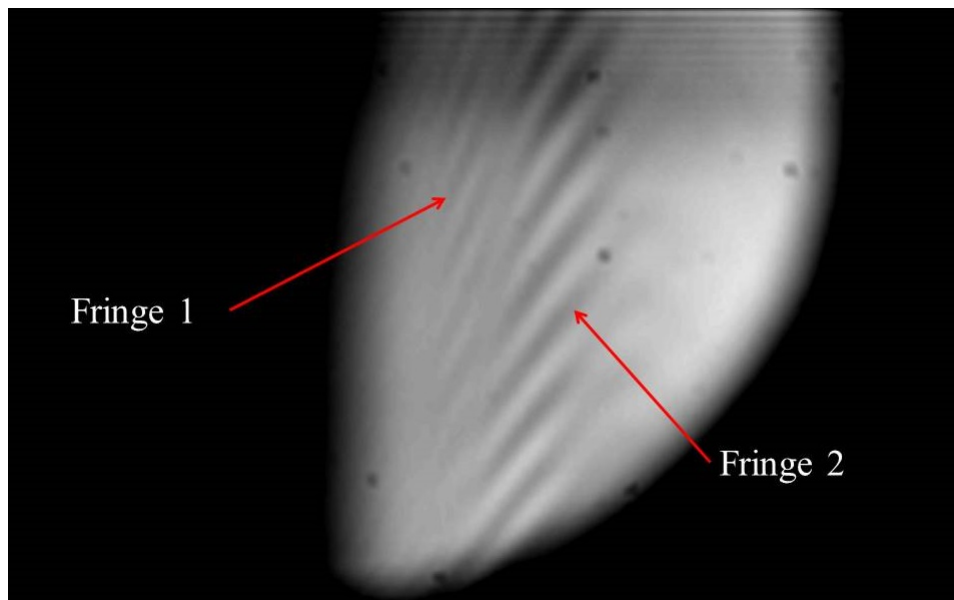


Figure 4.3: First result obtained using a sodium vapor lamp. Two distinct fringes can be seen in the image corresponding to wavelengths 589 nm and 589.6 nm. However the fringe contrast is very poor due to mismatch in path length and poor imaging.

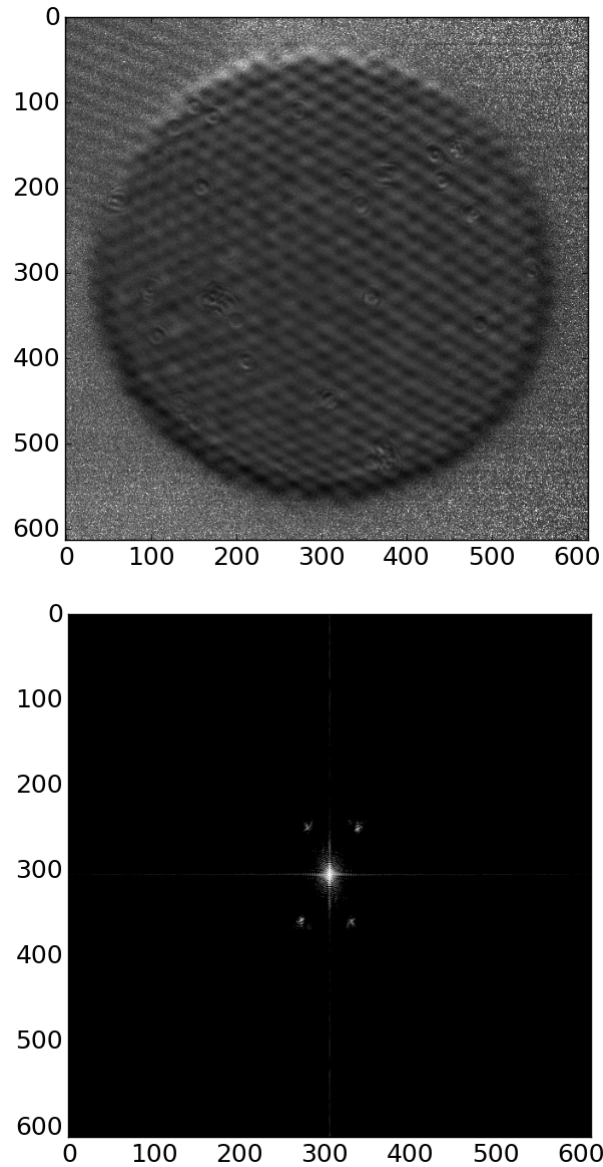


Figure 4.4: *Top:* The fringe obtained from the sodium vapor lamp. Two distinct fringes can be seen in the image corresponding to wavelengths 589 nm and 589.6 nm, respectively. *Bottom:* The two-dimensional FFT of the flat-corrected interferogram.

4.4.1 Estimation of Resolving Power (R)

The two sodium D lines were fitted using Gaussian profiles (Fig. 4.6, Table 4.2). Before the fitting, we have interpolated the data to 1001 points and smoothed using a Savitzky-Golay filter. The difference in the wavelength of sodium emission lines (here 0.6 nm) corresponds to $289.232 - 319.019 = 29.787$ fringe frequency (resolution elements) (Table 4.2), and one fringe fre-

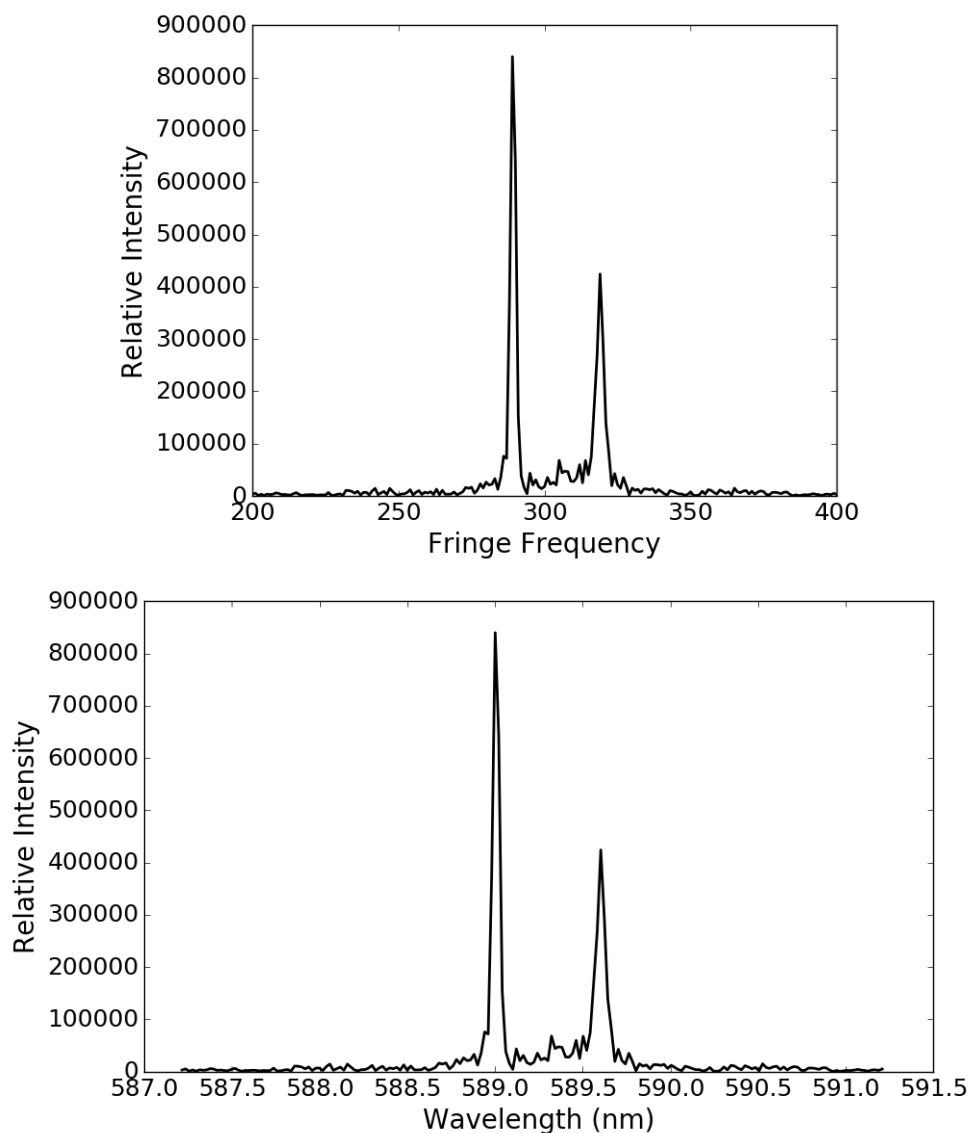


Figure 4.5: The spectrum of the sodium vapor lamp retrieved from the interferogram, (*Top:*) in pixel scale and in (*Bottom:*) in wavelength scale.

quency corresponds to a wavelength of $\frac{0.6}{29.787} = 0.020$ nm. Therefore, the resolving power of the instrument is $R = \frac{589}{0.020} = 29450$, giving the FOV solid angle at the grating (Ω) of the instrument as $2.13 \times 10^{-4} sr$.

Table 4.2: Parameters obtained from the fitting of emission lines.

Parameter	Peak 589 nm	Peak 589.6 nm
Amplitude	$1.4226 \times 10^6 \pm 2.75 \times 10^4$	$5.5331 \times 10^5 \pm 1.61 \times 10^4$
Central fringe frequency	289.232291 ± 0.021386	319.019890 ± 0.030433
FWHM	0.95939241 ± 0.021386	0.90398182 ± 0.030433

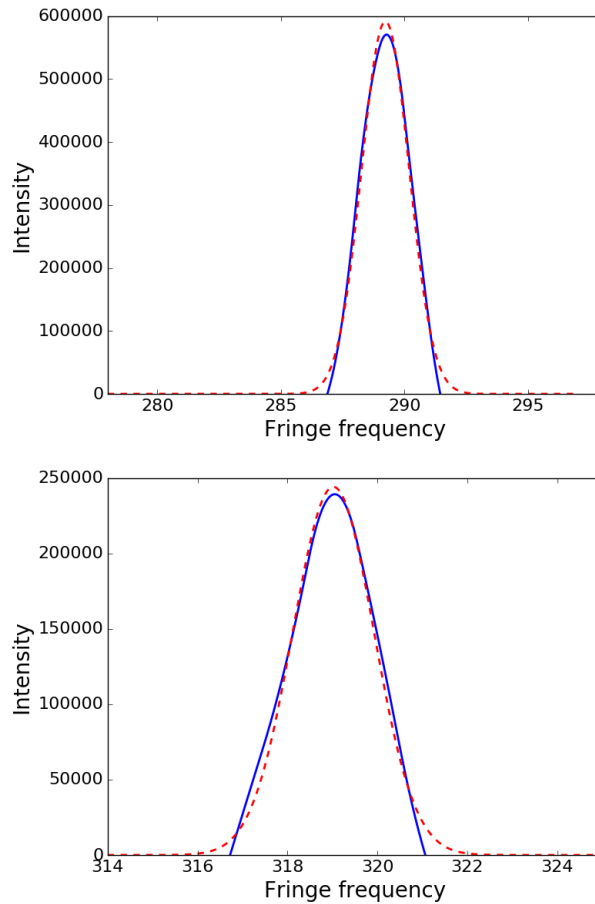


Figure 4.6: *Top:* The emission line corresponding to 589 nm (continuous line) and the fitted Gaussian curve (dotted line). *Bottom:* The emission line corresponding to 589.6 nm (continuous line) and the fitted Gaussian curve (dotted line).

4.4.2 Checking the tunability of the system

We have used a helium lamp source to test the tunability of our system. A visible spectrum of the Helium lamp is given in Fig. 4.7. The TSHS instrument is tuned for these emission lines, and interferogram is recorded on the detector. The interferograms obtained are given in Fig. 4.12.

4.4.3 Interferogram from a continuum source

A passband filter is usually used in the SHS system to limit the spectrum to one SHS sideband or to limit the spectral range, in order to minimize the shot noise contribution. However, we have not used a spectral filter in our lab setup. Instead, we tested the tunability of the system using a

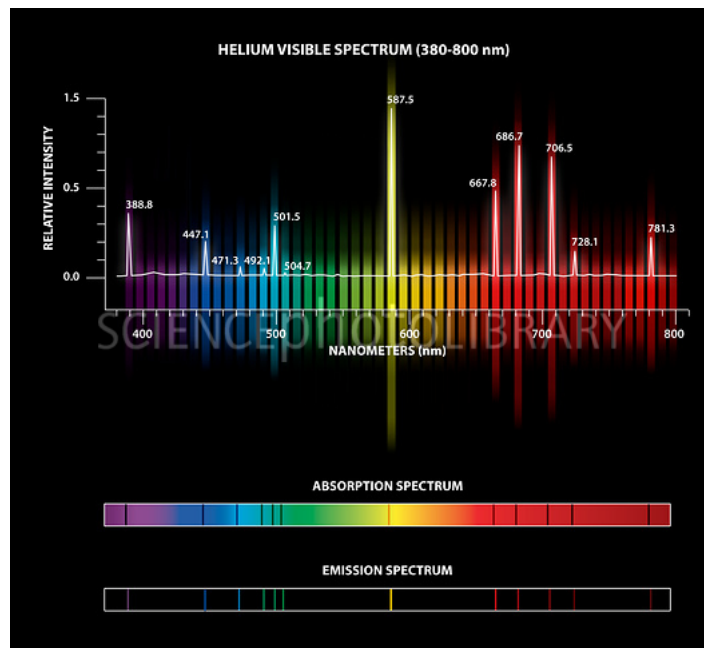


Figure 4.7: The visible spectrum of a Helium lamp. Image courtesy: <https://www.sciencephoto.com>

halogen lamp monochromator Andor SHAMROCK–SR-303I (Fig. 4.9), for which we selected a band around 588 nm. The light from the source is fed to the monochromator and the required wavelength, as well as the bandwidth, is selected by adjusting the monochromator’s parameters. It has an $F/4$ aperture and a focal length of 303 mm, giving a wavelength range from 170 nm to $10\ \mu\text{m}$ and a wavelength resolution of 0.05 nm. The fringes obtained for this particular setup are shown in Fig. 4.11. Since the halogen lamp spectrum is a broadband source, the interferogram is only modulated in a small region around the zero OPD location (Fig. 4.11). The fringes obtained for the wavelength centered at 587 nm are tilted as shown in Fig. 4.11 (*Left*), while the fringes from the wavelength centered at 589 nm are tilted in the opposite direction (Fig. 4.11, *Right*), in agreement with our simulation (Section.3.2.3). Fringes obtained for the Littrow wavelength (588 nm) do not show any tilt as expected (Fig. 4.11, *Middle*).

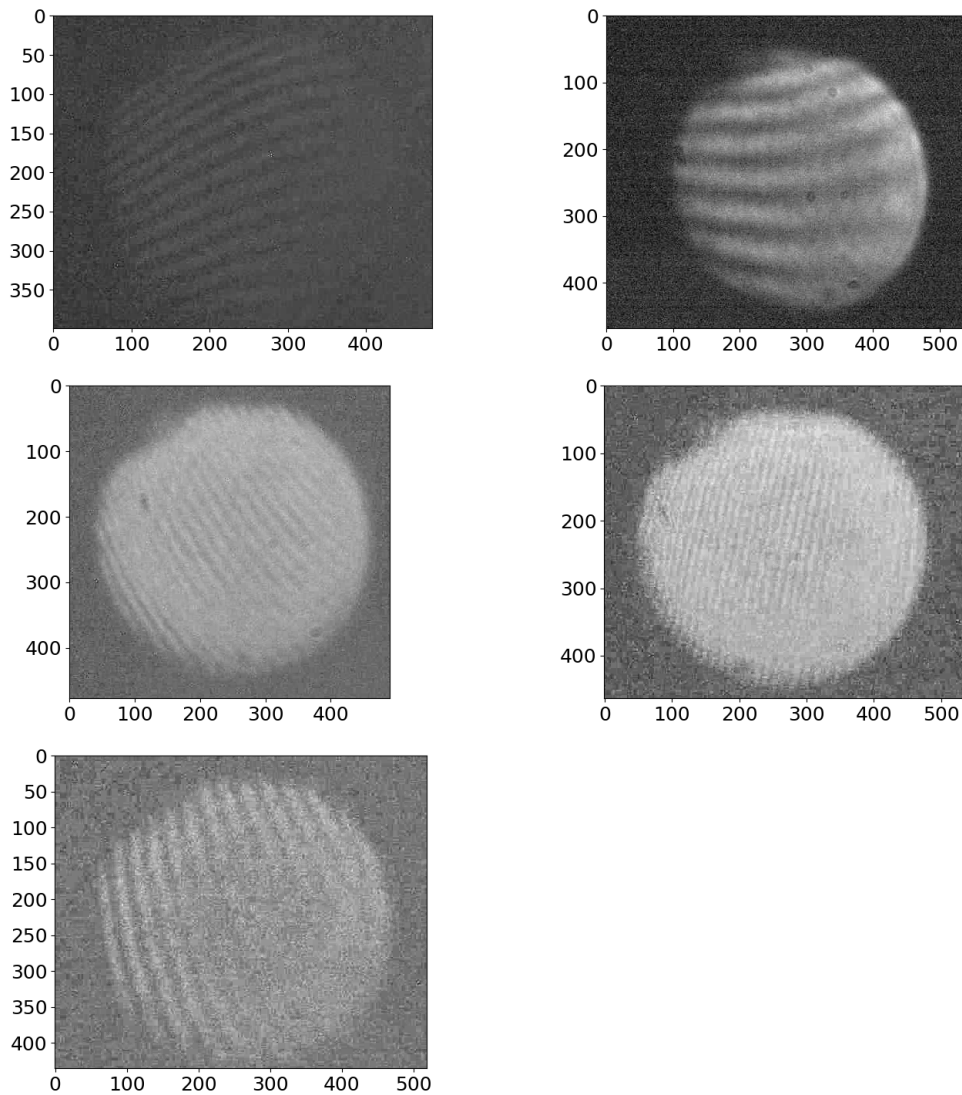


Figure 4.8: Fringes obtained for different emission lines in the Helium lamp spectra. The emission line for each fringes follows the order 438.793 nm, 447.148 nm, 501.567 nm, 587.562 nm, and 667.815nm

4.5 Effect of line broadening on the interferogram

In our calibration setup, we passed only a part of the input spectra through the SHS with the help of the monochromator. The interferogram covered the entire illuminated area when the source consists of a strong emission line narrow full-width half maximum (FWHM). However, when the emission line becomes broadened the interferogram gets confined to a narrow region in

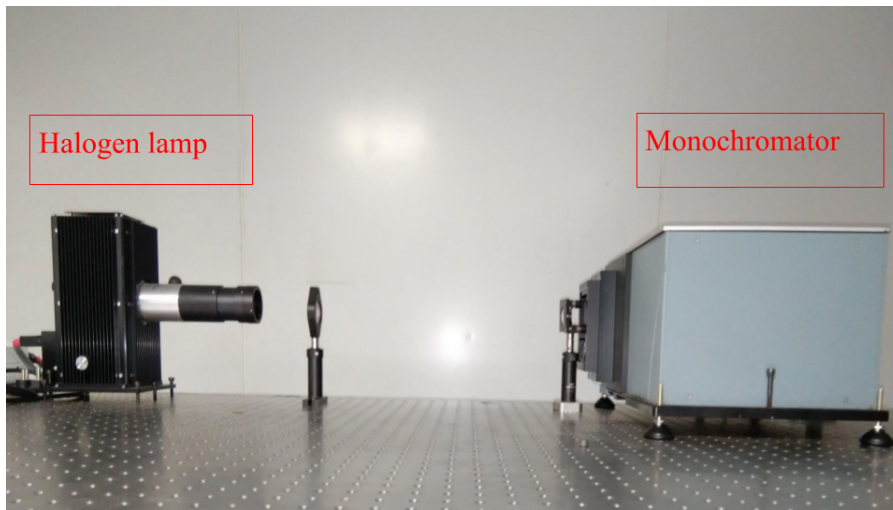


Figure 4.9: The setup of monochromator Andor SR-303IA and halogen lamp. A halogen lamp produces a continuous spectrum. The monochromator is used to select a particular wavelength region.

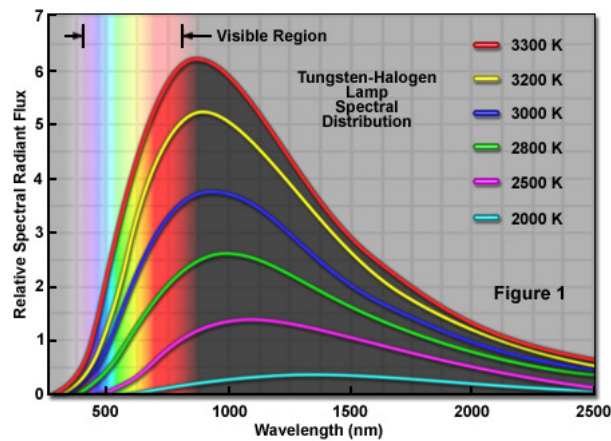


Figure 4.10: The spectral distribution of a halogen lamp. Image courtesy: <http://zeiss-campus.magnet.fsu.edu/articles/lightsources>

the illuminated area. We have also tested this experimentally using the SHS monochromator setup. We adjusted the input slit width of the in different steps such that it limits the spectral bandwidth that enters in the SHS. The results are shown in Fig. 4.12. From this, we assumed that the input spectra from the monochromator are broadened Gaussian profile with features superimposed upon it.

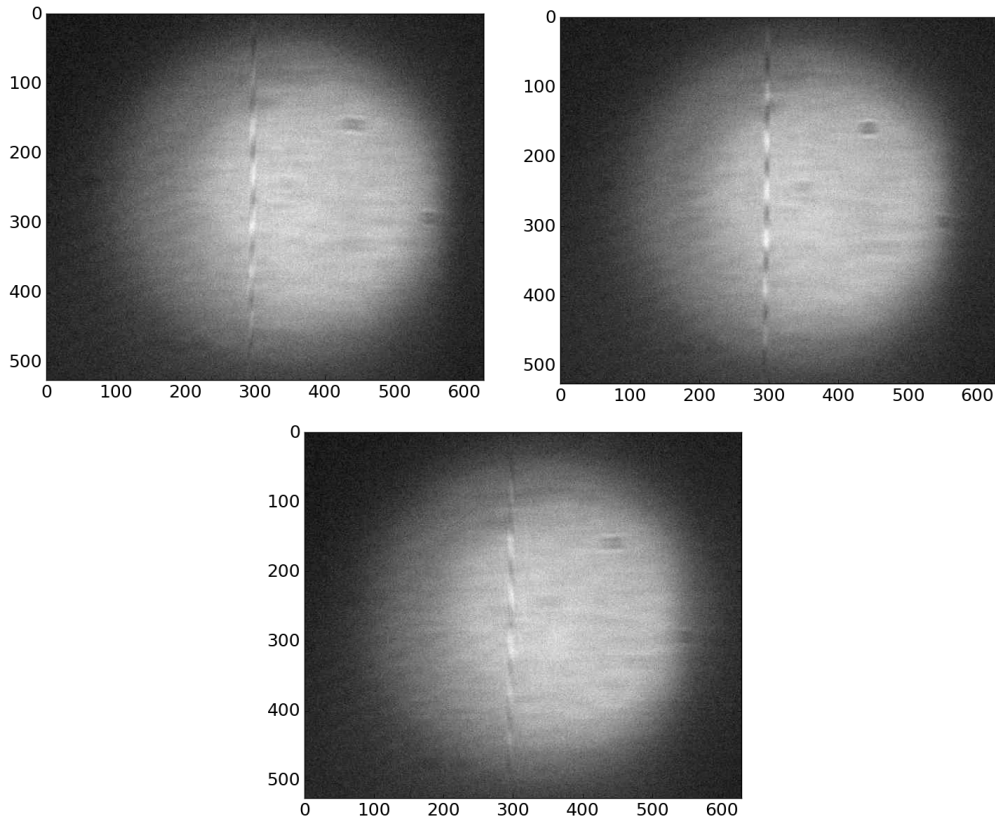


Figure 4.11: Fringes obtained for a continuum source – halogen lamp. The central wavelength is changed using the monochromator. *Top Left:* Fringes obtained for a wavelength band centered at 587 nm. *Top Right:* Fringes obtained for a wavelength band centered at 588 nm. *Bottom:* Fringes obtained for a wavelength band centered at 589 nm. As the wavelength moves away from the central wavelength, there is a change in fringe frequency.

4.5.1 Effect of vibration on the system

The Coudé room where the TSHS housed was maintained at a temperature of 18°C using an air conditioning unit. However, this has created vibrations in the optical bench where TSHS was kept since the bench was not floated. Therefore the obtained fringes were of less visibility (Fig. 4.13, *Left*), and the visibility degraded with the exposure. Therefore, we had to keep the air-conditioner unit switched off during the TSHS observations.

4.5.1.1 Observation of the celestial object

Due to the low sensitivity of the current detector we could not observe objects fainter than magnitude 1. Therefore, we selected Sirius (α CMa) and Betel-

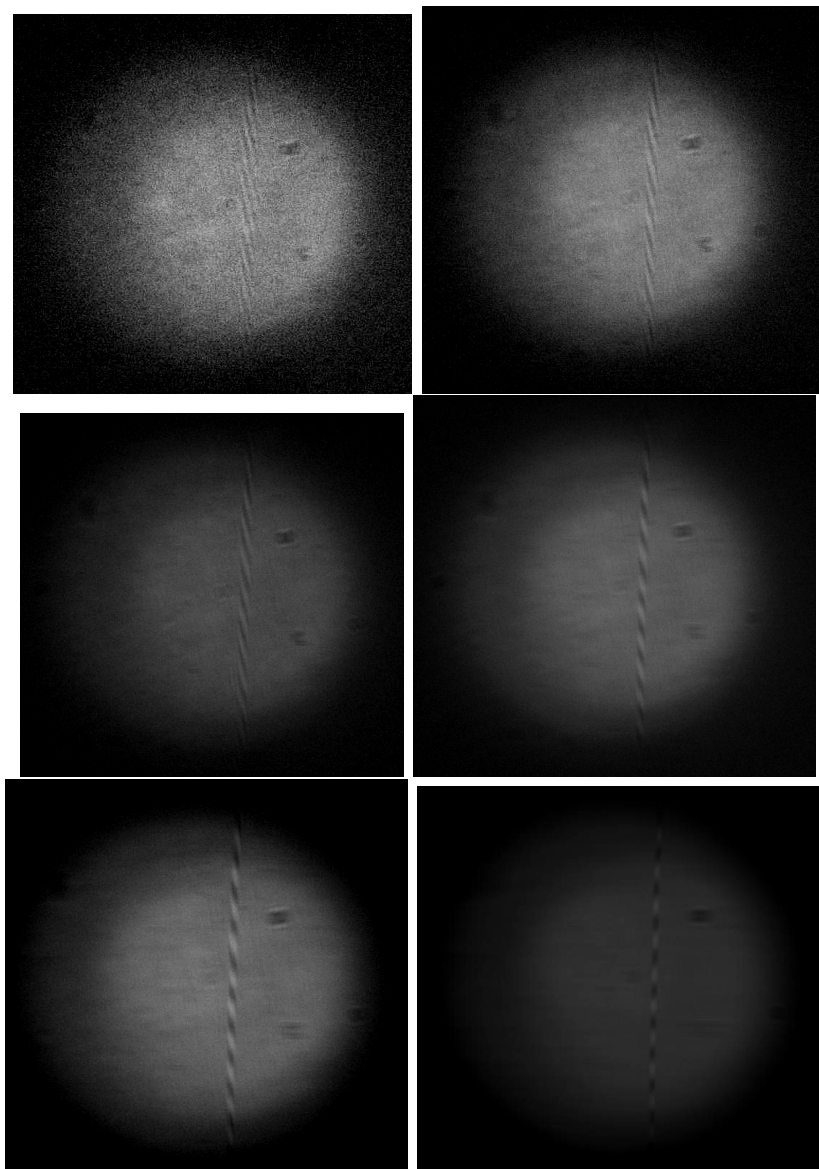


Figure 4.12: The variation in the interferogram with the output slit width of the monochromator. All the other parameters of the monochromator like the input slit width, the central frequency (589nm) are all kept the same except the output slit width. The output slit width of the monochromator corresponding to each fringe is as follows: from the top left corner, $200\mu m$, $400\mu m$, $500\mu m$, $1000\mu m$, $2000\mu m$ and $2500\mu m$

geuse (α Ori) with magnitudes -1.45 and 0.45 (Table. 4.3), respectively for the testing of our instrument. A calibration interferogram was taken using the

Table 4.3: Details of Observations conducted on 20 March 2018

Object	RA	Dec	UT	Exposure(s)
Betelgeuse	05:55:10	$7^{\circ}24'26''$	13:41	12
Sirius	06:45:09	$-16^{\circ}42'58''$	13:52	8

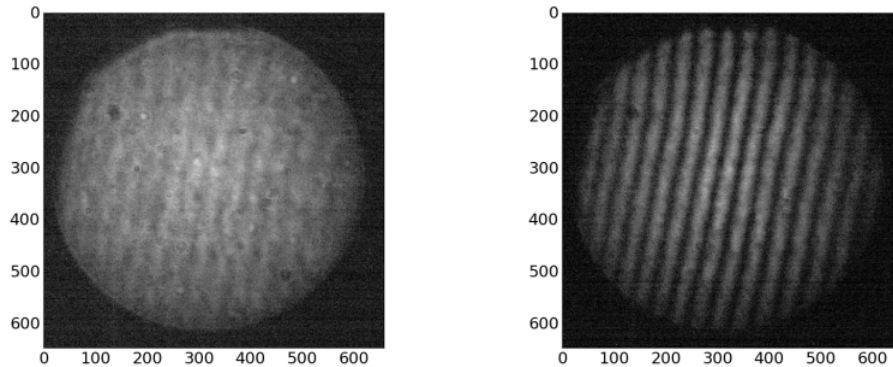


Figure 4.13: Variation in the visibility of fringes in the presence of vibration. *Left:* Fringes corresponding to the H_{α} line of the hydrogen lamp taken with one-second exposure. The air conditioner was on during the exposure. The vibration caused by the air conditioner reduced the visibility of the fringes. *Right:* Same observation but with air conditioner switched off during the exposure.

hydrogen lamp before the observations, and then the telescope was pointed towards the source. The resultant interferograms and the two-dimensional Fourier transform of the interferogram for Betelgeuse and Sirius are shown in Top, Left and Right panels of Figs. 4.14 and 4.15, respectively. The retrieved spectra, along with the spectra from the ELODIE archive (Moultaka et al., 2004) for comparison (red dashed line), are shown in the Bottom panels of Figs. 4.14 and 4.15, respectively.

4.6 Summary

In this chapter, we have discussed the testing as well as the first light result from the SHS instrument. We have carried out different testing on the instrument using Hydrogen and Helium lamps. The spectrum of these lamps contains different emission lines. We have tuned the instrument for each emission line and obtained the interferogram. The first light results were obtained with VBT, and the selected stars were Betelgeuse and Sirius. We have also tested the effect of line broadening on the fringes with a continuum source monochromatic setup.

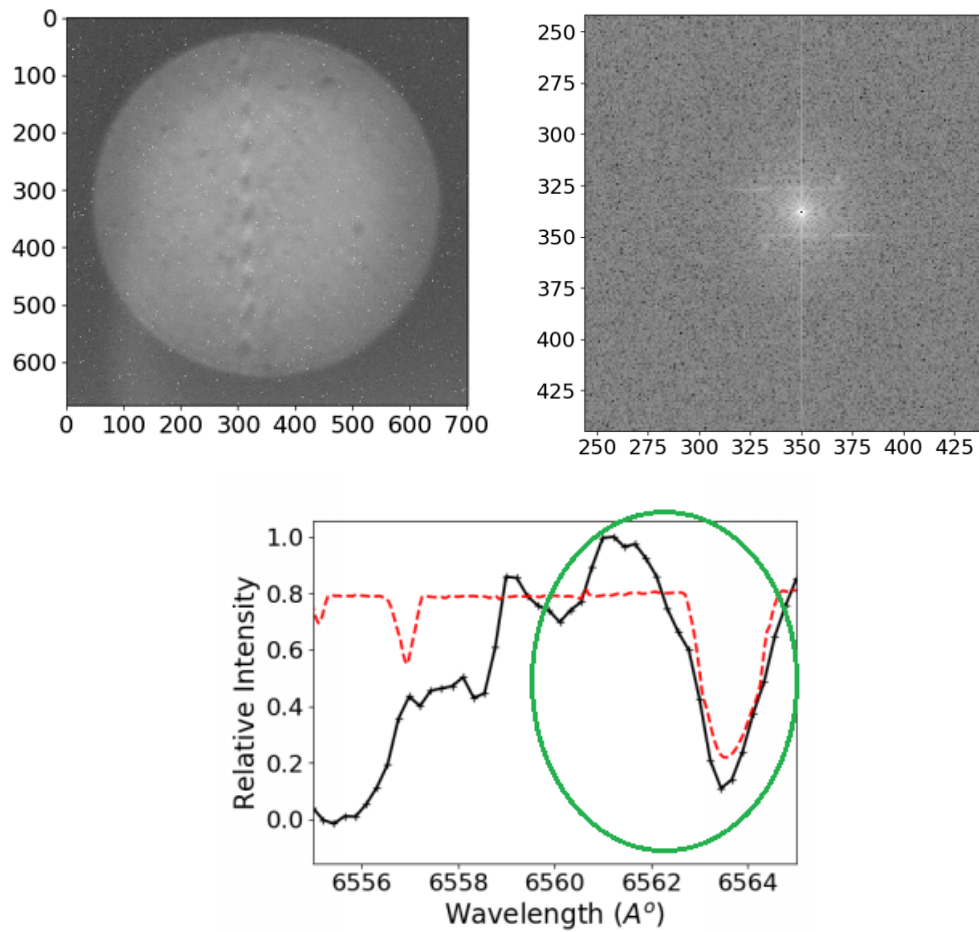


Figure 4.14: *Top, Left:* The interferogram obtained for the Betelgeuse. The circular patch is the illuminated area of the grating imaged on to the detector. The fringes are visible in the central part of the illuminated area. *Middle:* The zoomed version of the 2D Fourier transform of the interferogram where spectrum is visible. The retrieved spectrum of the star (solid black line) along with the spectrum obtained from the ELODIE archive (red dashed line) is plotted together for comparison. The transfer function of the filter is not removed from the spectrum. The wavelength covered (FWHM) by the filter is shown in the green circle.

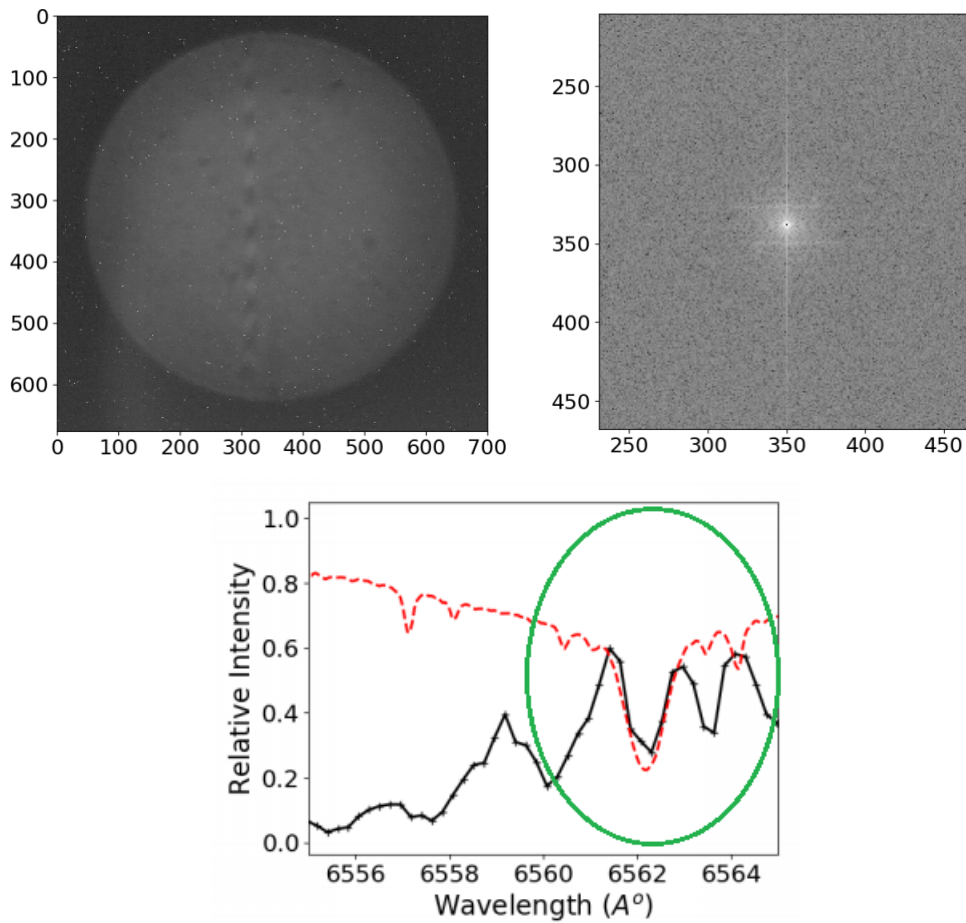


Figure 4.15: *Left:* The interferogram obtained for the Sirius. The circular patch is the illuminated area of the grating imaged on to the detector. The fringes are visible in the central part of the illuminated area. *Middle:* The zoomed version of the 2D Fourier transform of the interferogram where spectrum is visible. *Right:* The retrieved spectrum of the star (solid black line) along with the spectrum obtained from the ELODIE archive (broken red line) are plotted together for comparison. The transfer function of the filter is not removed from the spectrum. The wavelength covered (FWHM) by the filter is shown in the green circle.

Chapter 5

Wavelength calibration and implementation of a pipeline.

K. Nirmal, Sridharan R., S. Sriram, Suresh Ambily, Joice Mathew, Mayuresh Sarpotdar et al., Proc. SPIE 10702, Ground-based and Airborne Instrumentation for Astronomy VII, 107024V (6 July 2018);

5.1 Introduction

In this chapter, we describe the wavelength calibration procedure of the Tunable SHS instrument. Also, we describe the pre-spectral retrieving procedures such as bias correction and flat correction and spectrum retrieval from the interferogram through a Fast Fourier transform. We have illustrated the application of windowing functions such as Hamming and Hanning for the removal of the side lobes from the spectrum. We have incorporated these techniques into our data reduction procedure and implemented a spectra reduction pipeline for the tunable SHS using Python. The chapter details the pipeline also.



Figure 5.1: Image of a Thorium-Argon lamp. Image courtesy <https://www.photronlamp.com/products/p858a-thorium-argon>

5.2 Wavelength Calibration

Wavelength calibration in a conventional grating spectrometer is done with the help of emission line source such as a metal halide lamp like Thorium argon lamp (Fig. 5.1). A metal halide lamp has many unevenly spaced emission lines. Generally, the wavelength calibration is carried out by illuminating the input slit of the spectrograph with a thorium argon lamp. A comparison spectrum as shown in Fig. 5.2 is obtained on the detector.

Each spot in Fig. 5.2 correspond to each emission line in the Thorium-Argon lamp. A relation between the pixel position and the wavelength of the emission line is found from this comparison spectrum, which is used for the wavelength calibration of the spectrum of the celestial source. This calibration procedure is carried out every time before taking the spectrum.

The detector output of SHS only gives the interferogram, unlike an echelle spectrum (Fig. 5.2). The spectrum is retrieved by taking 2D Fourier transform of the interferogram. One dimensional spectrum is generated from the 2D Fourier transform is by taking a line cut (column wise or row wise depending upon the orientation of the interferogram). However, the X-axis of the one-dimensional spectrum is in fringe frequency or resolution elements.

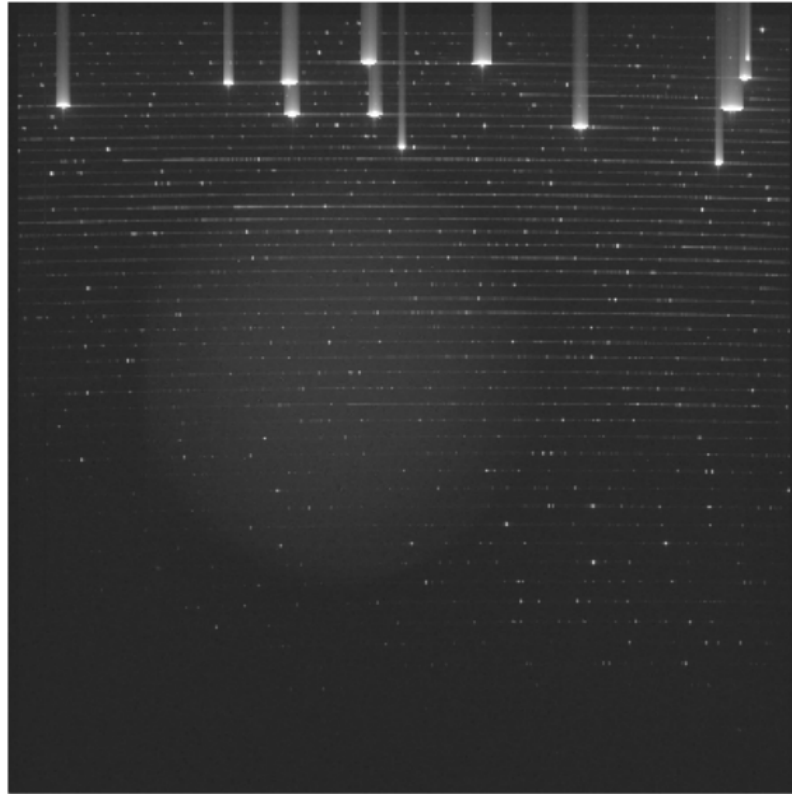


Figure 5.2: The echelle spectrum of the Thorium Argon lamp. The bright dots represents the emission line in different orders.

Hence there should be some mapping between the fringe frequency and the wavelength, and it is necessary to wavelength calibrate the spectrum before the retrieval of any useful information.

In case of Tunable SHS, wavelength calibration in the entire wavelength range 300 nm to 700 nm is difficult, since, in order to calibrate TSHS, the system should be aligned to a Littrow wavelength of interest, the lamp source should contain emission lines in that region, and a narrow band filter is required to get good fringe visibility. Therefore to calibrate the instrument in the entire wavelength range from 350 nm to 700 nm one requires a large number of filters. A passband filter is usually used in the SHS system to limit the spectrum to one SHS sideband or to limit the spectral range, in order to minimize the shot noise contribution.

5.3 Wavelength Calibration setup

We calibrated the TSHS system using a halogen lamp monochromator Andor SHAMROCK–SR-303I (Fig. 5.3) setup. The light from the halogen lamp is fed to the monochromator through a two lens system. One of the lenses focuses the diverging beam and the other lens re-image the spot on to the slit of the monochromator. (Fig. 5.3) Moreover, the required wavelength, the bandwidth, is selected by adjusting the monochromator’s parameters. The monochromator has an F/4 aperture and a focal length of 303 mm, giving a wavelength range from 170 nm to 10 μm and a wavelength resolution of 0.05 nm. The procedure explained here can be followed to the entire optical wavelength regime, but here we limited to a small chunk of wavelength centered around 650 nm. In this procedure, we have mitigated the need for different narrow band filters by using a monochromator setup.

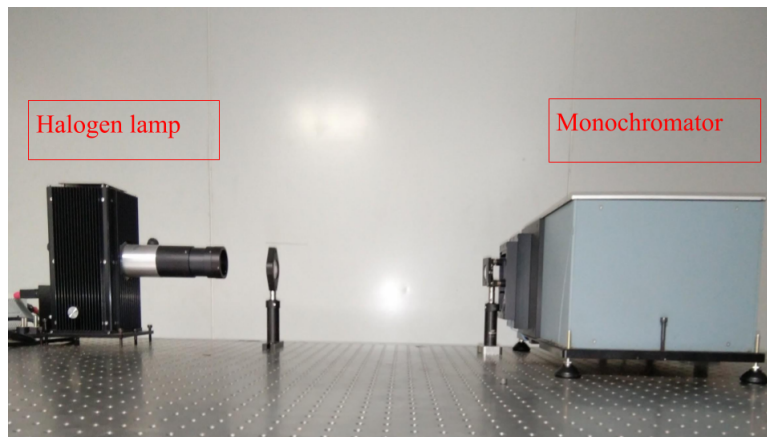


Figure 5.3: The halogen lamp monochromator setup for wavelength calibration.

Initially, we aligned the TSHS system using a laser diode of 650nm. The grating of the TSHS system is tilted in such way that the beams from each arm of the TSHS overlap at the detector. The laser diode is removed and is replaced by the monochromator output. The monochromator output is fed to the TSHS with a 100 μ optical fiber. The parameters of the monochromator (central wavelength, input slit width, output slit width) are adjusted such that the output of the monochromator is also at 650 nm. An interferogram is

recorded on the detector in this condition. We have made two assumptions: The first assumption is that the monochromator output can be considered as broadened emission line spectrum and can be fitted with a Gaussian profile. The second assumption is that the central wavelength of the monochromator corresponds to the peak of the Gaussian profile. Hence in order to understand the effect of a broadened emission line we have modeled the SHS system in MATLAB (Perkins et al., 2013). We used this model for understanding how the shape of the spectrum and the size of the interferogram are related. In our model, we gave different spectrum profiles and obtained corresponding interferograms. We used a Gaussian profiles having different FWHM as our spectrum profiles and obtained interferogram corresponding to the spectrum profile as explained in section 3.4.

5.4 Calibration procedure

We adjusted the input and output slit width of the monochromator such that a clear interferogram is obtained on the detector. To start with, the output wavelength of the monochromator was kept at 650nm and interferogram is recorded. The output wavelength of the monochromator is changed in 1 nm steps (ascending and descending orders) by adjusting the monochromator's parameters. The interferogram for each condition (Fig. 5.4) is recorded. The two dimensional Fourier transforms of these interferograms were estimated, and the one-dimensional spectra were retrieved by taking a line cut in the 2D Fourier transformed interferogram. A Gaussian profile is fitted to each one-dimensional spectrum retrieved from the interferogram (Fig. 5.5). The fringe frequency corresponding to the peak of the Gaussian profile (mean value of the Gaussian profile) and the width of the Gaussian profile (standard deviation of the Gaussian profile) are estimated.

We have plotted the central wavelength of the monochromator output against the fringe frequency corresponding to the peak of the Gaussian profile (Fig. 5.6). We found out that in wavelength chunk from 647 nm to 653nm

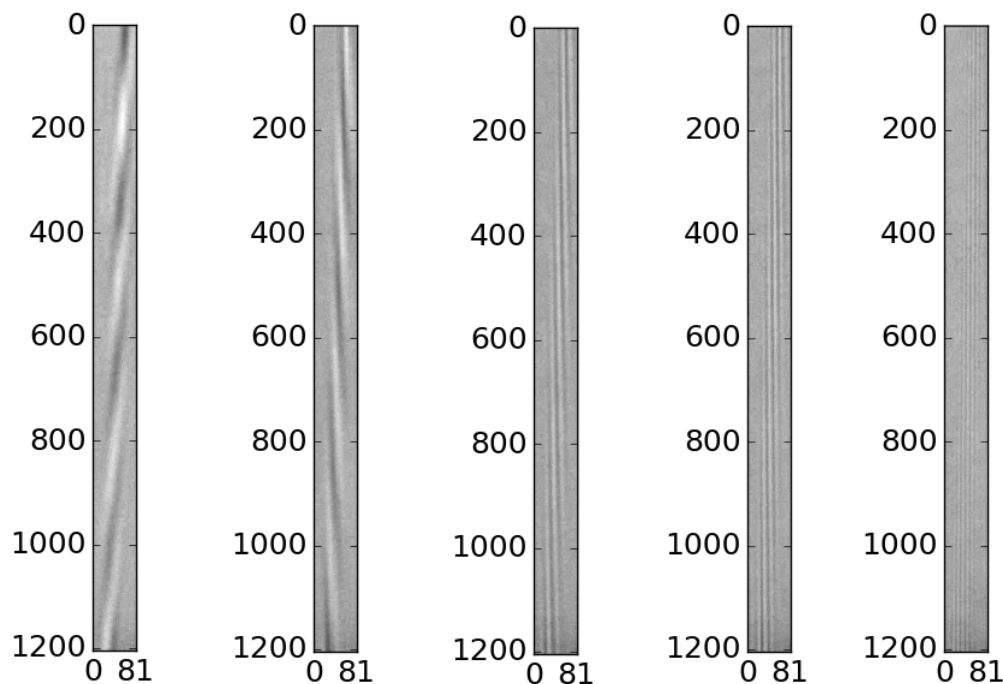


Figure 5.4: The interferogram obtained for different central wavelengths—649nm, 650nm, 651nm, 652nm, and 653nm

the fringe frequency and the central wavelength of the monochromator output follow a linear relation. A straight line is fitted to the data, and the parameters of the fit are found. Thus, the linear relation can be written as in Equation 5.1, where λ is the central wavelength of the monochromator output. This procedure can be followed to other wavelength chunks by aligning the SHS for the wavelength in consideration and adjusting the monochromator parameters.

$$\lambda = 0.085 \times \text{fringe frequency} + 646.23 \quad (5.1)$$

5.5 Dark correction

A photosensitive device such as charge coupled device or photodiode should give a zero signal when not exposed the light. However, this is not the case since there is a small amount of current flowing through the device. This

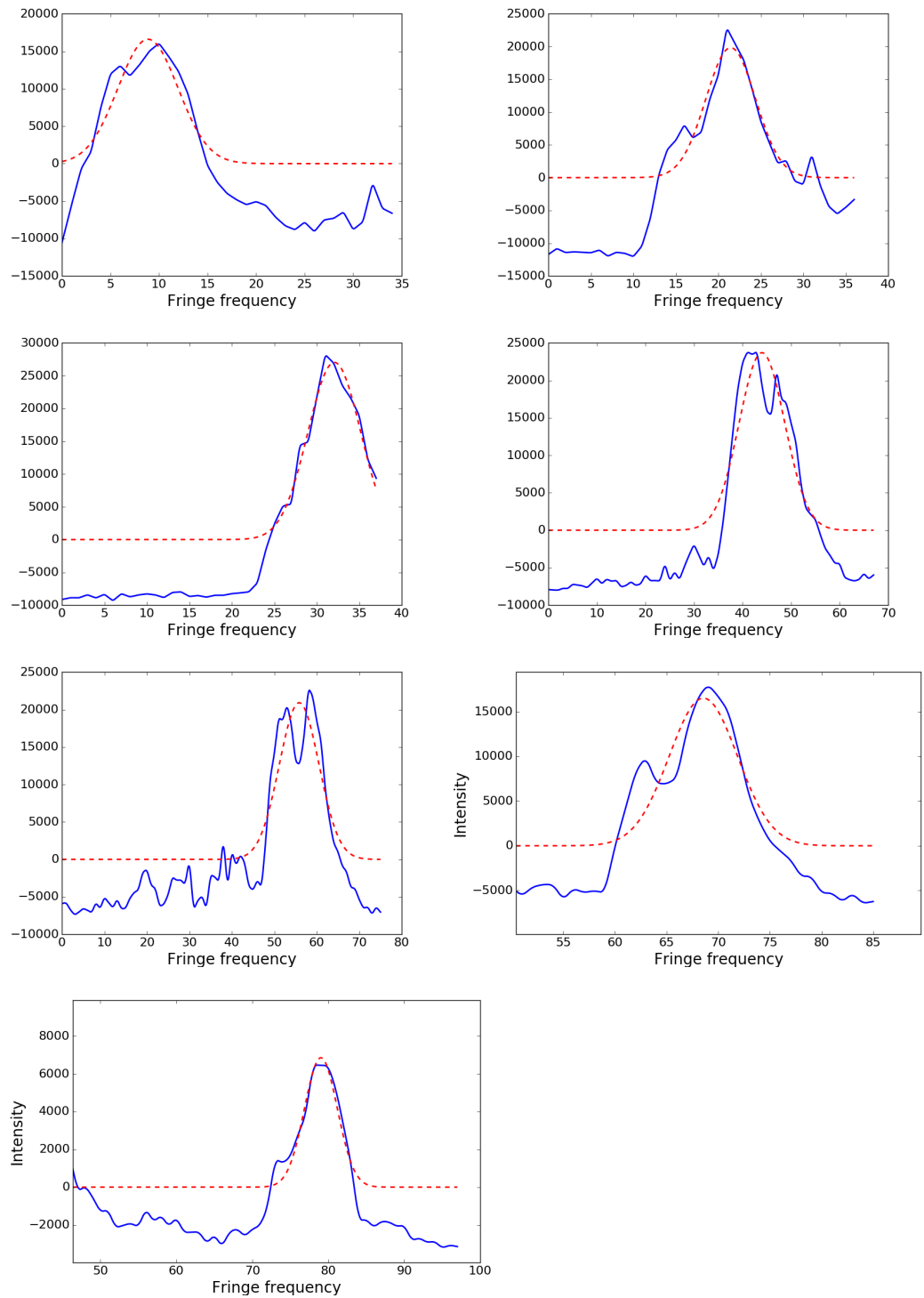


Figure 5.5: The retrieved one dimensional spectrum (continuous line) from the interferogram corresponding to a monochromator central wavelength of 647 nm, 648 nm, 649 nm, 650 nm, 651 nm, 652 nm and 653 nm in the order from top Left. The fitted Gaussian profile is shown in broken line.

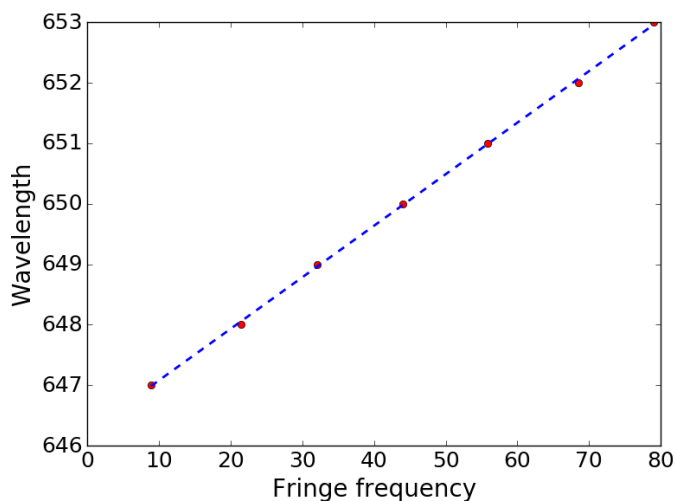


Figure 5.6: A graph showing the relationship between the fringe frequency and the central wavelength of the monochromator output.

current generally known as the dark current is generated by the random creation of electron-hole pair in the depletion region. Dark current is one of the noise sources in image sensors. Its effect is prominent when the sensor is exposed more. Dark current can affect the image quality in two ways, by giving temporal variation in the signal value and as a fixed pattern noise. Visible fixed pattern noise is caused by hot pixels which have higher than normal dark current compared to other pixels. When prolonged exposure is given these pixels can be seen as bright pixels in the image and hence known as hot pixels. The effect of dark current can be reduced from the image by subtracting the dark frame from the actual image signal electronically as in eq. 5.2, where $I_{dark_corrected}$ is the dark current corrected image, I_{dark} is the dark frame and I_{actual} is the actual image. A dark frame is generated by not exposing the image sensor to the light but giving the same integration of the actual signal. A dark frame generated from our current sensor with 12 seconds exposure is shown in the Fig. 5.7.

$$I_{dark_corrected} = I_{actual} - I_{dark} \quad (5.2)$$



Figure 5.7: (Top:) A dark frame generated from our image sensor by giving an exposure of 12s in log scale. The hot pixels are visible in the image.

5.6 Flat-fielding

The data recorded by the instrument (or the detector) is affected by the presence of dust on the optical components and the detector, as well as by the intrinsic non-uniformity (insensitivity) of the detector, and this will be seen in the interferogram. In order to get the flat field (uniform illumination on the detector), after obtaining the fringe, one arm of the interferometer was closed, and this uniform illumination was imaged with the same detector. This process was repeated by closing the other arm of the SHS (Fig. 5.8). A master flat was generated from these flats, and the flat correction was done as explained in Englert et al. (2006) as in eq. 5.3 where I_{flat} is the flat and $\overline{I_{flat} - I_{dark}}$ is the average of the dark corrected flat. In Fig. 5.8, we show the flats obtained by closing each arm of the interferometer and Fig. 5.9, Left shows uncorrected interferograms and Fig. 5.9, Right shows flat corrected interferograms.

$$I_{flat_{corrected}} = \frac{(I_{actual} - I_{dark})}{(I_{flat} - I_{dark}) / [\overline{(I_{flat} - I_{dark})}]} \quad (5.3)$$

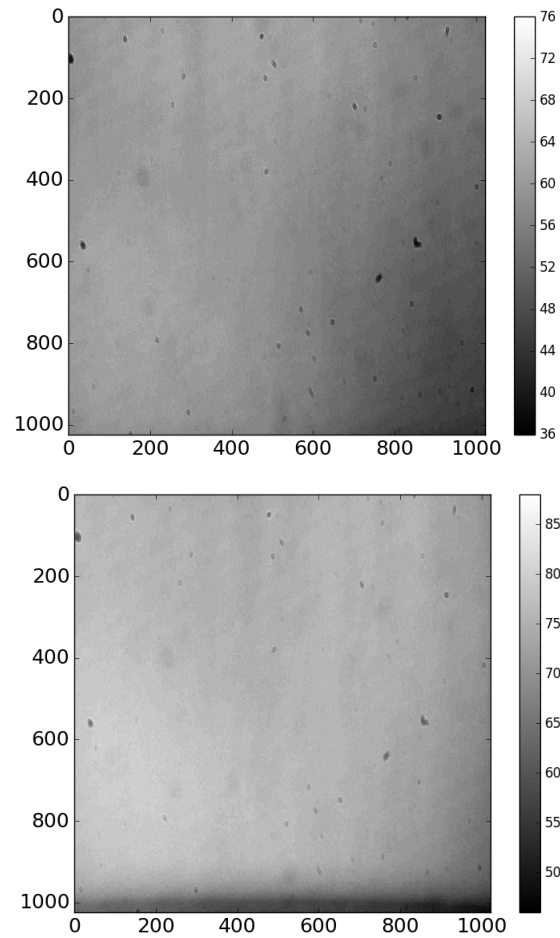


Figure 5.8: Flats obtained by closing each arm of the interferogram. There is a slight intensity difference in each individual flat which is due to the ratio at which the beamsplitter splits light into each arm of the SHS.

5.7 Spectral leakage correction in SHS

The interferogram obtained from SHS instrument is the Fourier transform of the spectrum. The interferogram comprises different fringe frequencies which are proportional to the number of resolution elements. The spectrum is calculated by taking the Fourier transform of the interferogram. A weighting function known as apodization function is used to multiply the interferogram before computing the Fourier transform. The limited resolving power corrupts the spectrum derived from any spectrometer which is valid for all the spectrometer including FTS and SHS. The estimated spectrum is the convolution of the actual spectrum with a sinc function known as the Instrumental

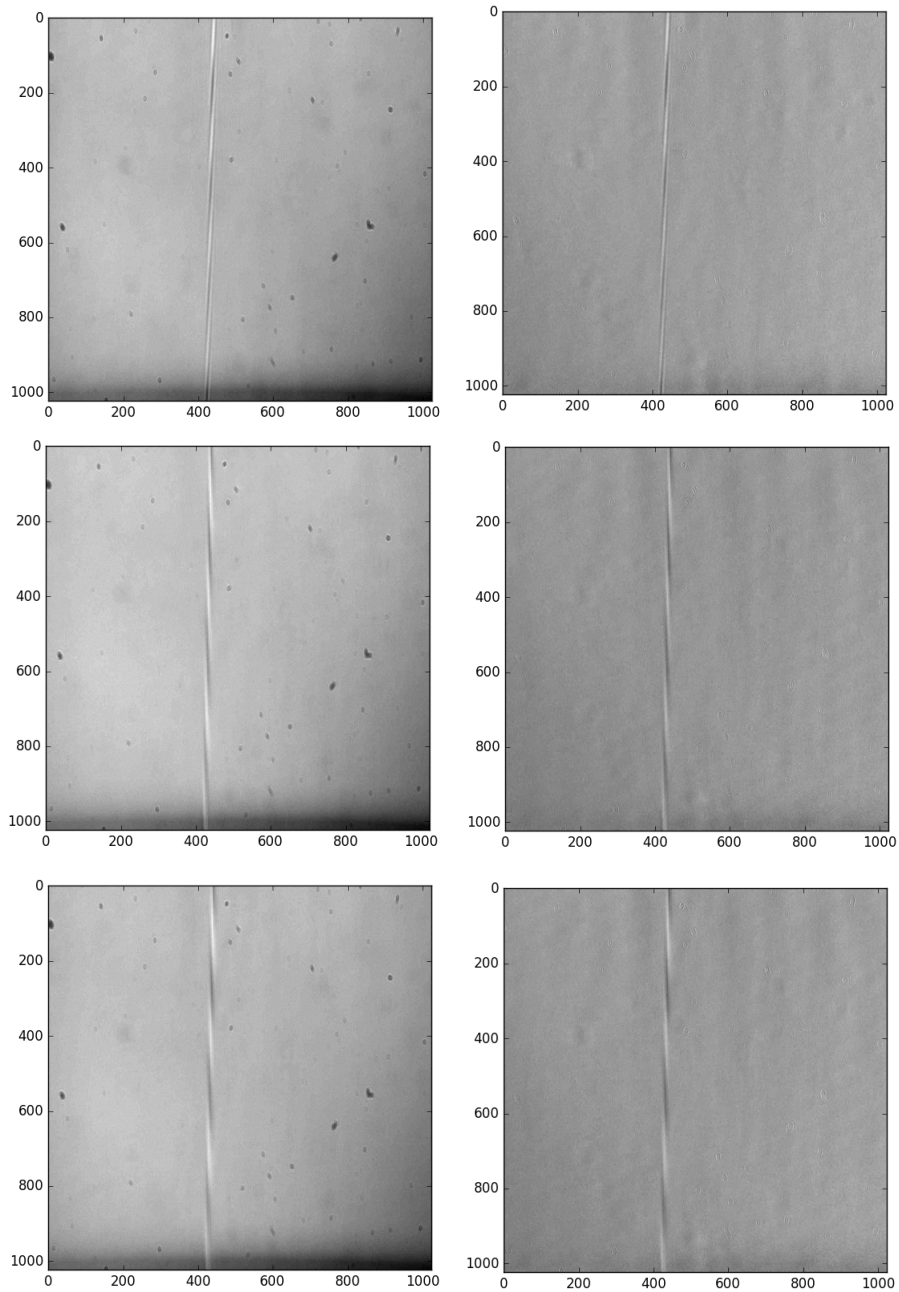


Figure 5.9: Flat fielding applied to different signal. (Top, Left) The uncorrected interferogram corresponding to 648.5nm and (Top, Right) corrected interferogram corresponding to central wavelength 648.5nm. (Middle, Left) The uncorrected interferogram corresponding to 648.5nm and (Middle, Right) corrected interferogram corresponding to central wavelength 650.2nm. (Bottom, Left) The uncorrected interferogram corresponding to 648.5nm and (Bottom, Right) corrected interferogram corresponding to central wavelength 650 nm.

line shape. In SHS, the interferogram is present only on the part where the beam is present (for an emission line source and is localized inside the beam for a continuum source). It is the same as the interferogram multiplied by a square function. In Fourier domain, it becomes the actual spectrum (Fourier transform of the interferogram) convolved with a sinc function (Fourier transform of the square function). When an FFT algorithm is used to retrieve the spectrum it assumes that the signal is infinite, the signal fed to the FFT algorithm repeats itself, and there are discontinuities in the signal which are not there. Sharp discontinuity has broad frequency spectra; this will cause the energy, which should be concentrated on one frequency leaks into other frequencies and can be seen in the Fourier transform as secondary harmonics as seen in Fig.5.10. The energy in the main lobe is leaked into the secondary lobes which reduce the strength of the main harmonics which can be avoided by making the signal fall smoothly at every end of the measurement, by reducing the discontinuity using a window function so that it will not suffer from spectral leakage.

Apodization functions are multiplied with the interferogram to reduce the side lobes (ringing) in Fourier Transform spectroscopy. Multiplying with a proper apodization function helps to get the most accurate instrumental line shape. However, multiplying the interferogram with an apodization function has some adverse effect on the spectrum. Multiplying with an apodization function tends to increase FWHM of the main lobe hence reducing the resolution of the spectrum. Hence proper care should be taken by choosing an apodization function such that it optimizes the trade-off between resolution and spectral leakage error.

We have checked the performance of different apodization function by multiplying the apodization function with the interferogram and retrieving the spectrum. The top panel of the Fig. 5.12 shows the retrieved sodium vapor lamp spectrum after the multiplication of the window function. We have shown a zoomed version of the emission lines in the bottom panel of the Fig. 5.12. The window functions gave an almost similar result (refer

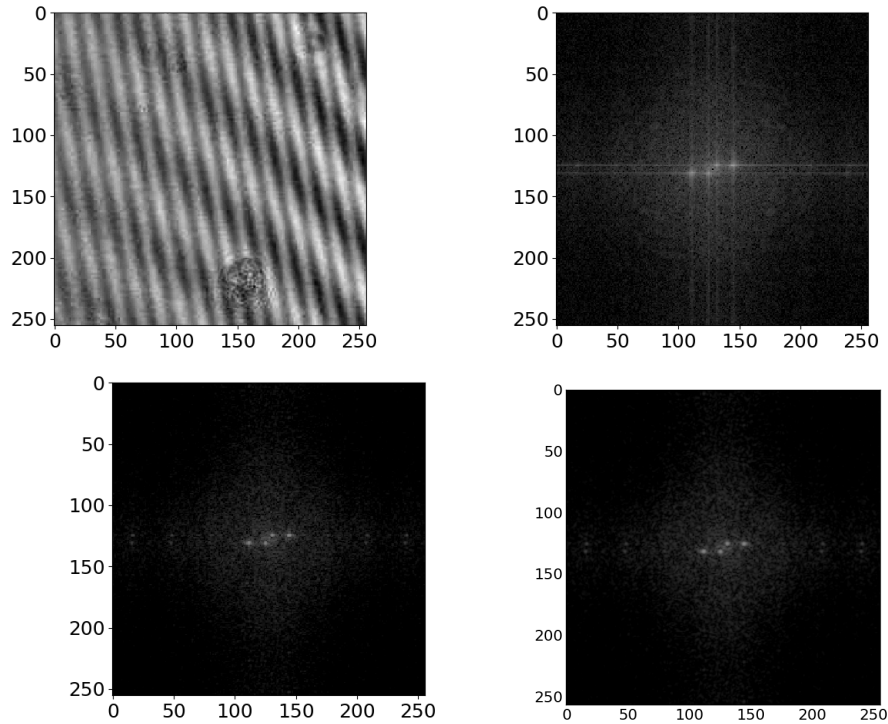


Figure 5.10: *Top Left:* The fringes obtained on the detector for the sodium vapor lamp. The original fringes are cropped to get 256×256 pixel as in figure. *Top Right:* The two dimensional Fourier transform of the obtained fringes. *Bottom:* The Fourier transform of the apodized fringes with a triangular window (Left) with a hamming window (right).

Fig. 5.12), however in the Hanning window the intensity is preserved compared with other windows. Hence we selected the Hanning window as the default apodization function in our pipeline.

5.8 A Python-based pipeline for SHS

We have implemented a python based pipeline for SHS (Fig. 5.14). This pipeline takes the interferogram image in *.jpeg* or *.png* format. The basic corrections on the interferogram such as bias and flat fielding can be done in the pipeline by selecting suitable correction files. The pipeline then calculates the two dimensional Fourier transform of the interferogram. There is a proficiency in the pipeline to select the suitable windowing function for apodization. The one-dimensional spectrum can be obtained from the two dimensional Fourier transform by taking a line cut along the vertical or hori-

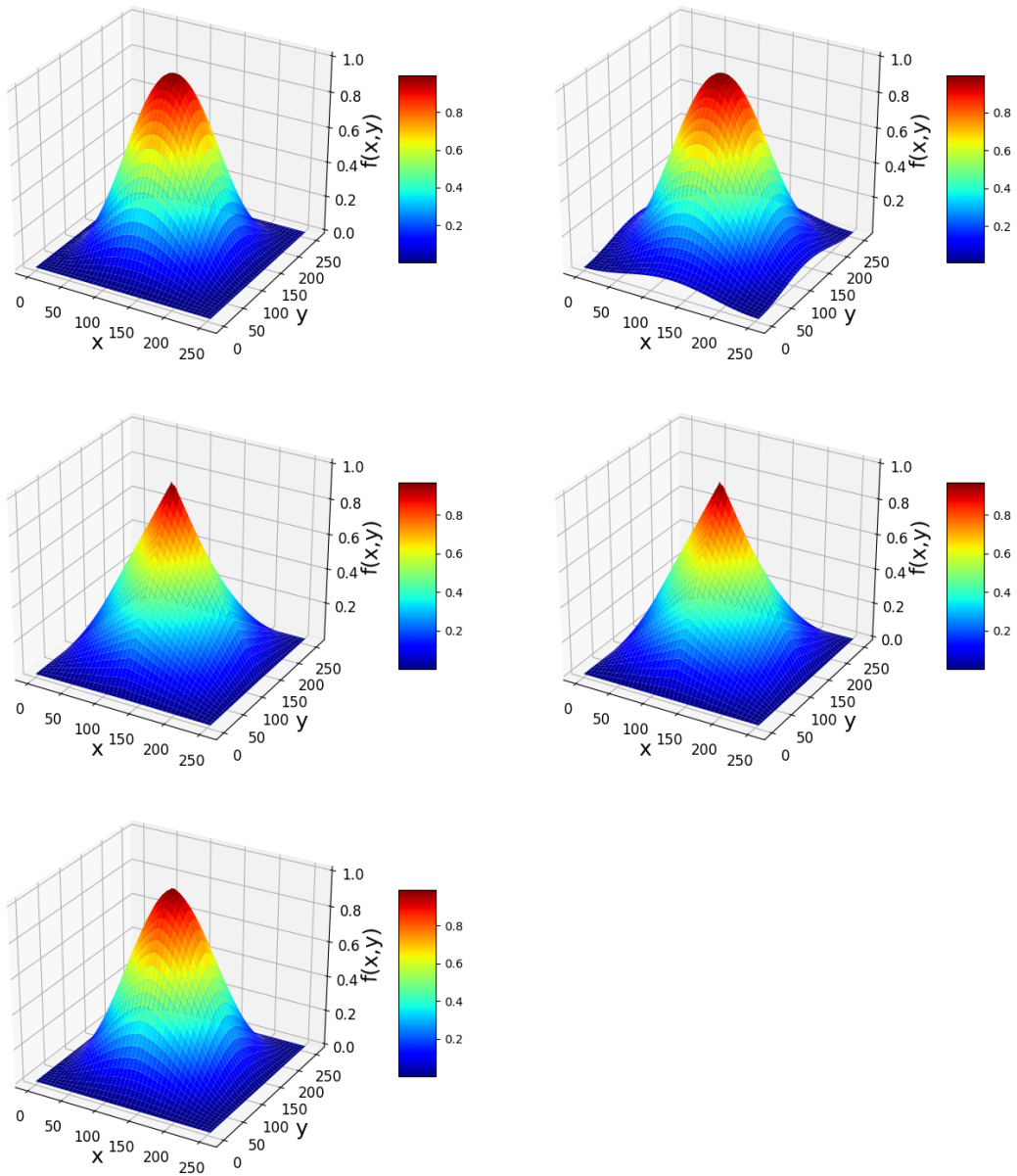


Figure 5.11: Different windowing function used to correct the spectral leakage. (Top, left) Hanning window, (Top, right) Hamming window, (Middle, left) triangular window, (Middle, right) Bartlett window, (Bottom) Barthann window

zonal axis depending upon the orientation of the interferogram. A flow-chart of the pipeline is given in Fig. 5.13.

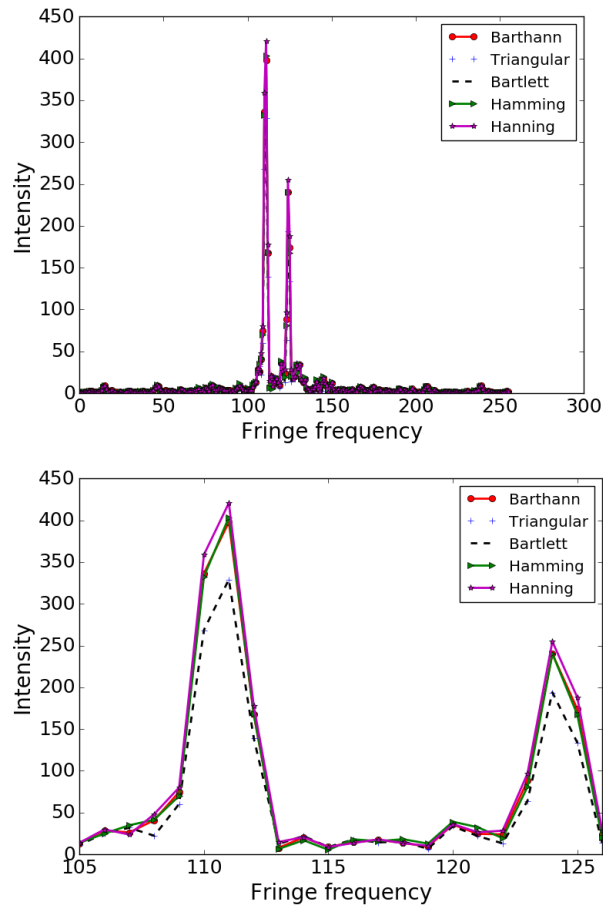


Figure 5.12: *Top:* The retrieved sodium vapor lamp spectrum after the multiplication of the window function. A zoomed version of the spectrum around the emission line is shown in the bottom panel.

5.9 Summary

In this chapter, we discussed the wavelength calibration of the tunable SHS instrument. This chapter also describes the basic processing procedures such as dark subtraction and flat correction. We have explored the effect of spectral leakage and how it can be corrected with a proper window function.

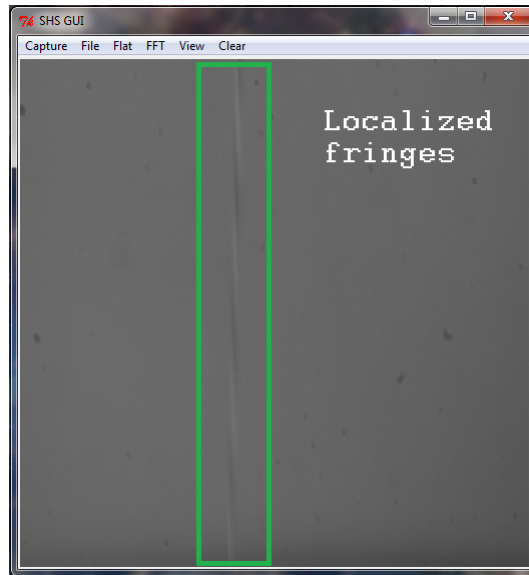


Figure 5.13: The Graphical user interface of the python based pipeline of the SHS instrument. The localized fringe is shown in the rectangle.

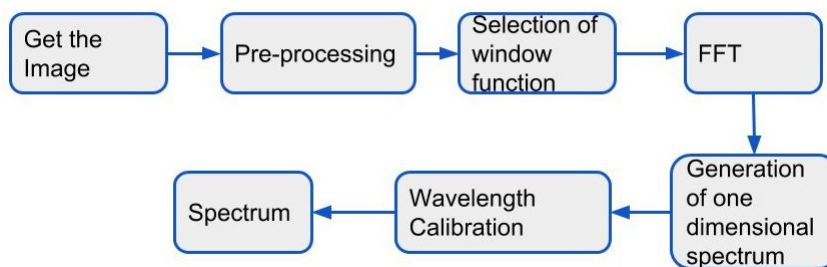


Figure 5.14: A block diagram showing the SHS python pipeline.

Chapter 6

Pointing system for balloon borne telescope

Nirmal K, A. G. Sreejith, Joice Mathew et al., Journal of Astronomical Telescopes, Instruments and Systems, Vol. 02, issue. 04, 047001. & Nirmal K., Sreejith A. G et al., Proc. SPIE 9912, Advances in Optical and Mechanical Technologies for Telescopes and Instrumentation II, 99126W (22 July 2016);

6.1 Introduction

In this chapter we describe the development of a pointing system using off the shelf components. We have developed this pointing system for the balloon-borne scientific payloads. This system was built using Dynamixel Mx series servomotors^a), Arduino controller and Micro Electro Mechanical System (MEMS) based Inertial measurement units (IMU). We have discussed how the system was built, tested from the ground as well as tethered launch, and how the system performed during different tests. This chapter also deals with how IMU is used to estimate the elevation and azimuth of the payload and

^a<http://www.robotis.us/mx-series/>

control algorithm used to correct the system for balloon platform.

6.2 Basic Principle and Realization of the System

Real-time communication with the payload on small balloons is difficult because of weight and radio-licensing constraints, and pointing mechanisms must, therefore, be autonomous. We have built the system with off-the-shelf electronic components and light-weight high-precision digital servomotors, where the user sets the pointing direction in the controller (Arduino Uno^b) in inertial coordinates Right Ascension (RA) and Declination (Dec) before the flight, and the pointing system is responsible for maintaining this direction regardless of balloon motion. In ground-based pointing and tracking systems, equatorial mounts are usually better suited for tracking celestial objects. However, such mounts require a fixed polar axis which is difficult to maintain in the generally unstable balloon flight. In such an environment, it is easier to use an alt-az mount, where we measure the angular displacement in the vertical direction from the horizon (0° altitude or elevation), and the angular displacement in the horizontal direction from the magnetic north (0° azimuth) (refer Fig. 6.1).

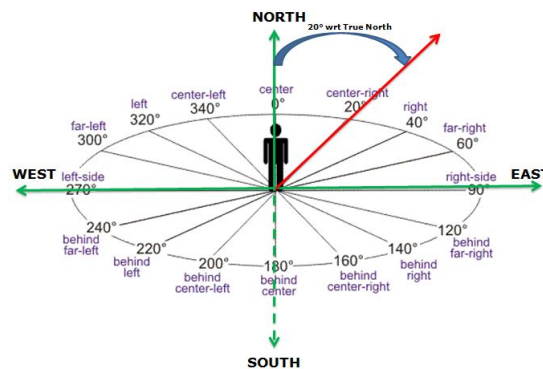


Figure 6.1: The azimuth with respect to magnetic north represented on a horizontal plane. Image courtesy: <http://directionaldrilling.blogspot.com>

^b<http://www.Arduino.cc>

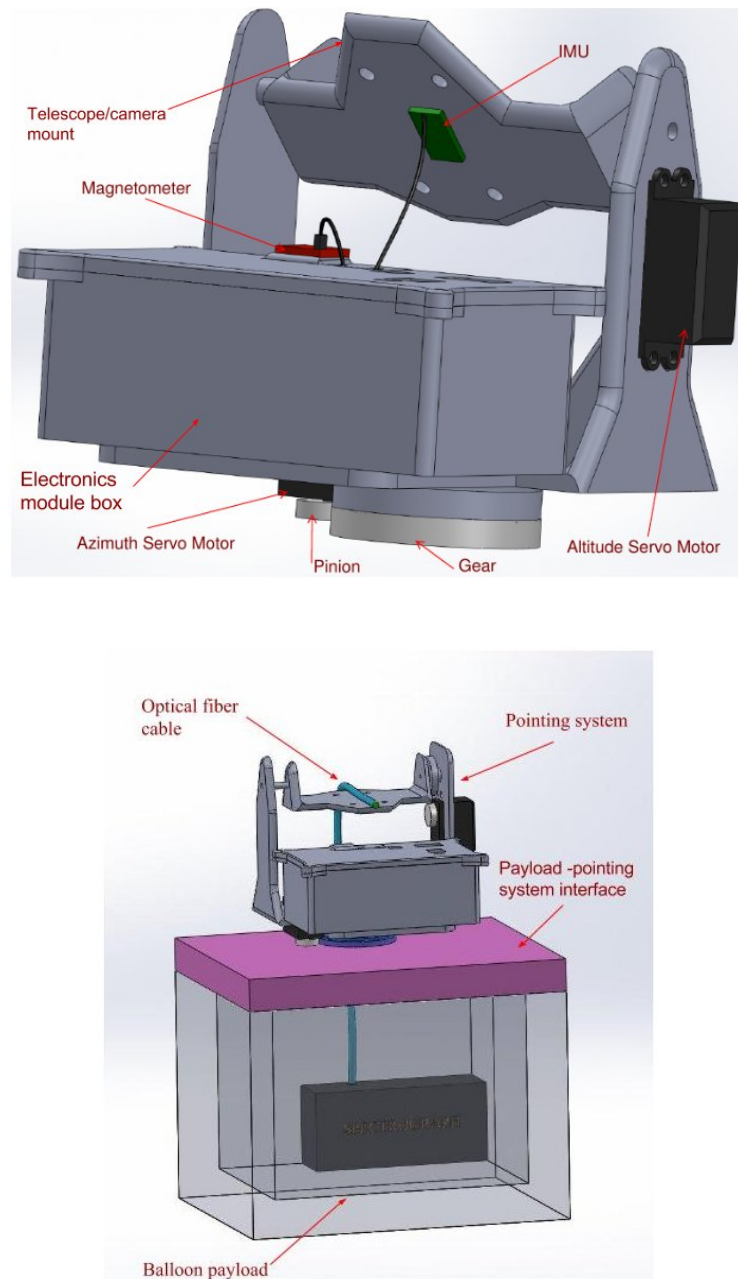


Figure 6.2: *Top:* Mechanical structure of pointing system. *Bottom:* Pointing system mounted on the payload.

We have designed the mechanical structure of the pointing system driven by the need to keep the weight low. The structure consists of an inner frame which slews in elevation, and an outer frame which slews in azimuth (Fig. 6.2, *Top*). A continuous-servomotor controls each frame. The shaft of these motors can be moved accurately to the desired angle using an internal

electronic circuit, which identifies the current angle of the motor shaft from a reference point and then moves the shaft to the desired position. The rotation is limited to $0^\circ - 85^\circ$ range to avoid ‘gimbal locking’ of the IMU (Savvidis et al., 2010) used to determine the attitude (Fig. 6.2, *Top*). However, the outer frame requires rapid rotation from 0° to 360° in azimuth, thus requiring a continuous servomotor^c.

The mechanical and structural design of the system (inner and outer frames, Fig. 6.2, *Top*) was performed with SolidWorks 3D modeling software^d. The complete balloon payload–pointing system assembly is shown in Fig. 6.2, *Bottom*.

6.3 Control Mechanisms

The Attitude Control System (ACS) (Fig. 6.3) comprises an Arduino Uno controller, a set of microelectromechanical system (MEMS) sensors, actuators and a GPS unit^e. The Arduino Uno controller is an open-source electronics platform based on easy-to-use hardware and software, developed at the Interaction Design Institute Ivrea, Italy. We have chosen this controller over its alternatives (Teensy^f, BeagleBone^g and Raspberry Pi^h) because of its extensive library of available software (Ham et al., 2012).

ACS functions can be divided into three parts:

1. Finding the pointing direction;
2. Estimation of the current position of the pointing system regarding the azimuth and the elevation using IMU and magnetometer output;
3. Calculating the difference between the desired and the actual pointing directions and moving the platform (telescope) to the desired position.

^cDynamixel MX-28T <http://www.trossenrobotics.com>

^d<http://www.solidworks.in>

^eiWave Systems SiRF StarIII GSC3f GPS receiver, iWave Systems, India (<http://www.iwavesystems.com>)

^f<https://www.pjrc.com/teensy>.

^g<http://beagleboard.org/bone>.

^h<https://www.raspberrypi.org>.

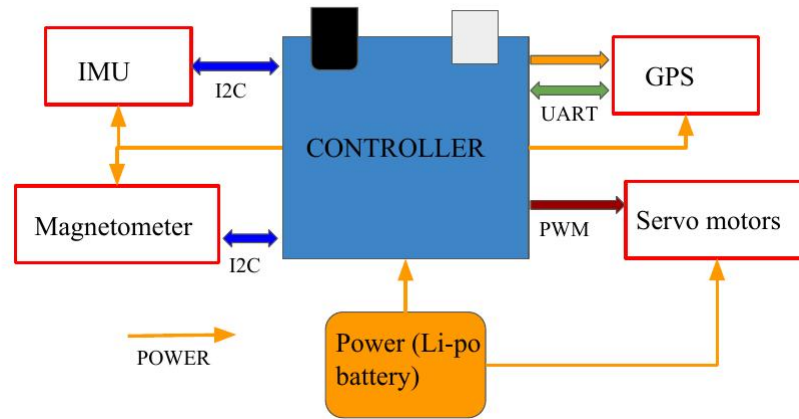


Figure 6.3: A block diagram of the Attitude Control System (ACS).

The first step is performed by converting the user-provided equatorial coordinates (RA and Dec), into elevation (ALT) and azimuth (AZI) using Eq. 6.1.

6.3.1 Conversion of Equatorial coordinates into horizontal coordinates

In our controller we converted the RA and Dec of the source into elevation and azimuth using the following formula,

$$\begin{aligned} \sin(ALT) &= \sin(Dec) \sin(LAT) + \cos(Dec) \cos(LAT) \cos(HA), \\ \cos(AZI) &= \frac{\sin(Dec) - \sin(ALT) \sin(LAT)}{\cos(ALT) \cos(LAT)}, \end{aligned} \quad (6.1)$$

where LAT and HA are the latitude and the hour angleⁱ, respectively. The controller updates the calculation of the desired azimuth and elevation every second, using the latitude and longitude of the platform as determined by the on-board GPS.

ⁱHour Angle – time elapsed after a celestial body transited over observer’s meridian. It is expressed in terms of local sidereal time (LST) and RA as $HA = LST - RA$.

6.3.2 ACS computation

The accuracy of ACS computation was checked by calculating the position of the Sun every second for about 30 minutes and comparing it with the actual values. The equatorial coordinates of the Sun do not change noticeably over the duration of the observation, but the position in the sky will change by 8° due to the Earth's rotation, and its apparent position will change by another 0.833° due to atmospheric refraction. We programmed the initial position of the Sun, time, date and location of the observation (Table 6.1) into the ACS. The values of altitude and azimuth calculated by the controller using Eq. 6.1 were compared with the actual values obtained from NOAA^j. The errors in this calculation were $\pm 0.006^\circ$, within our desired precision.

Table 6.1: ACS programmed parameters.

Date	18/06/2015
Time (IST)	8:00 am
Location	Hoskote
Latitude	13.113° N
Longitude	77.811° E
Programmed RA of Sun	86.269°
Programmed Dec of Sun	23.390°

6.3.3 Estimation of the attitude

We placed an IMU (MPU-9150) on the inner frame (Fig. 6.2, *Left*) to measure the elevation of the pointing system. The MPU-9150 comprises an inbuilt 3-axis magnetometer (AK8975), a combination of a 3-axis accelerometer and a 3-axis gyroscope (MPU-6050), and a digital motion processor capable of motion fusion^k. We have achieved better accuracy by fusing the data from the individual sensors (Emilsson et al., 2012), and we have used the accelerometer and gyroscope combined output to measure the elevation.

^jData provided by NOAA ESRL Global Monitoring Division, Boulder, Colorado, USA (<http://esrl.noaa.gov/gmd>).

^kIMU gives the Euler angles (roll, pitch, and yaw) of rotation as an output.

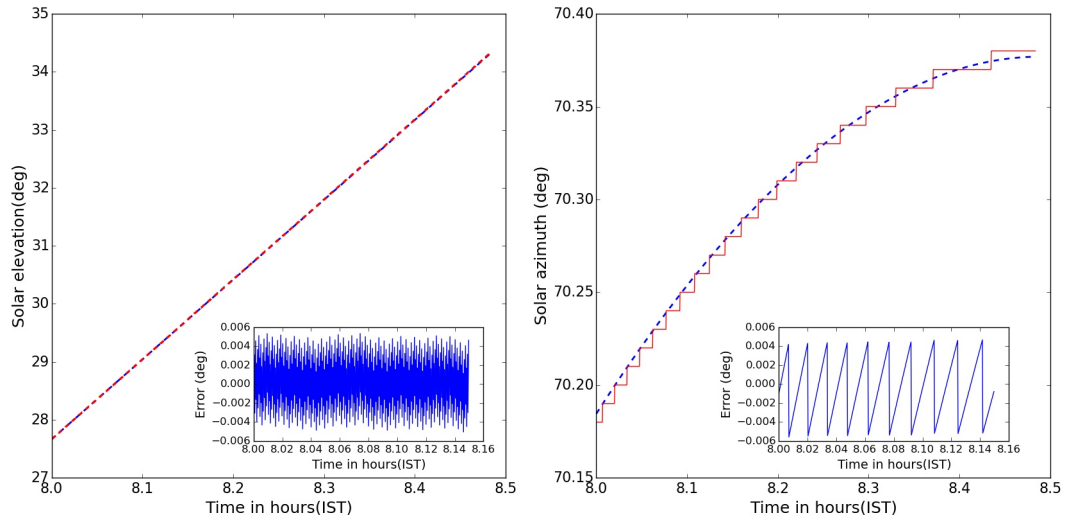


Figure 6.4: *Left:* Results of the ACS calibration, on June 18, 2015. Difference between solar elevation obtained from NOAA (blue line) and elevation calculated using Eq. (1) (red line). Inlet: Zoom on the calculated elevation to show the error bars. *Right:* Difference between solar azimuth obtained from NOAA (blue line) and calculated azimuth using Eq. (1) (red line). Inlet: Zoom on the calculated azimuth to show the error bars.

Although MPU-9150 includes a magnetometer, we did not use it for azimuth estimation. In our system MPU-9150 moves in elevation due to its location on the inner frame and thus the readings are unreliable. We, therefore, mounted another magnetometer (HMC5883L) on the outer frame (Fig. 6.2), which moves around an axis perpendicular to the Earth’s magnetic field, to measure the azimuth.

This magnetometer consists of high-resolution magneto-resistive sensors with an application-specific integrated circuit, containing an amplifier, automatic degaussing strap drivers, and offset cancellation circuits. The analog data from the magneto-resistive elements are digitized using an inbuilt 12-bit ADC. Any drift in the sensor measurements can be calibrated out by using its self-test mode, which internally excites the sensor with a nominal magnetic field.

We connected the magnetometer and the IMU to the Arduino I2C port, which is a multi-master serial single-ended computer bus through which low-speed peripherals are attached to the controller. The in-built MEMS gyroscope consists of vibrating solid state resonators that maintain their plane of

vibration even if the gyroscope is tilted or rotated. This type of gyroscope is known as Coriolis vibratory gyroscope (CVG) and is common in consumer electronics such as tablets and mobile phones. A voltage, proportional to the angular velocity of the IMU, is generated in the gyroscope and is digitized using a 16-bit ADC, whose full scale reading corresponds to 3.3 V. Thus, the analog voltage generated for an angular velocity of $1^\circ/\text{sec}$ is $3.3 \text{ mV}/(^\circ/\text{sec})$ ¹, corresponding to an ADC value of $\frac{3.3 \text{ mV}}{3.3 \text{ V}} \times (2^{16} - 1) = 65.535$. The gyroscope generates a bias voltage, which is measured when the IMU is stationary, and this bias is subtracted from the ADC value to get the actual response. The angular velocity rate in degrees per second is calculated using the following formula:

$$\text{Angular velocity rate}(\omega) = \frac{(V_{\text{ADC}} - V_{\text{bias}})}{\text{sensitivity}} (^\circ/\text{sec}), \quad (6.2)$$

moreover, the angular displacement is calculated by multiplying the rate by the period Δt ($\theta = \omega \times \Delta t$).

The accelerometer measures the acceleration (g) in X , Y and Z axes and generates a voltage proportional to the acceleration, which is digitized by the 16-bit ADC and read by the Arduino controller through its I2C port. The bias voltage (1.5 V), which is inherent in the accelerometer ADC output, is subtracted from the accelerometer output to get the voltage corresponding to the acceleration. The elevation in degrees is found from acceleration values using the equation

$$ALT = \arctan \left(\frac{V_{\text{accy}}}{V_{\text{accz}}} \right) + \pi, \quad (6.3)$$

where V_{accy} , V_{accz} are the bias-subtracted accelerometer, ADC outputs corresponding to acceleration in Y and Z axes, respectively.

The gyroscope gives precise values over short time duration but drifts for more extended observations (Sreejith et al., 2014), while the converse is

¹<https://www.invensense.com/wp-content/uploads/2015/02/MPU-9150-Datasheet.pdf>

true for the accelerometer: there is negligible drift over long periods of time, but a significant jitter occurs on short time scales (0.330° in 100 ms bins). We can reduce this jitter by combining the data from the gyroscope and the accelerometer using a Kalman filter^m. Figure. 6.5 shows the performance of the Kalman filter, where the top panel shows the elevation, calculated from only the accelerometer and the bottom panel shows the elevation from the fusion of the two sensors. The elevation jitter reduced to 0.143° per 100 ms.

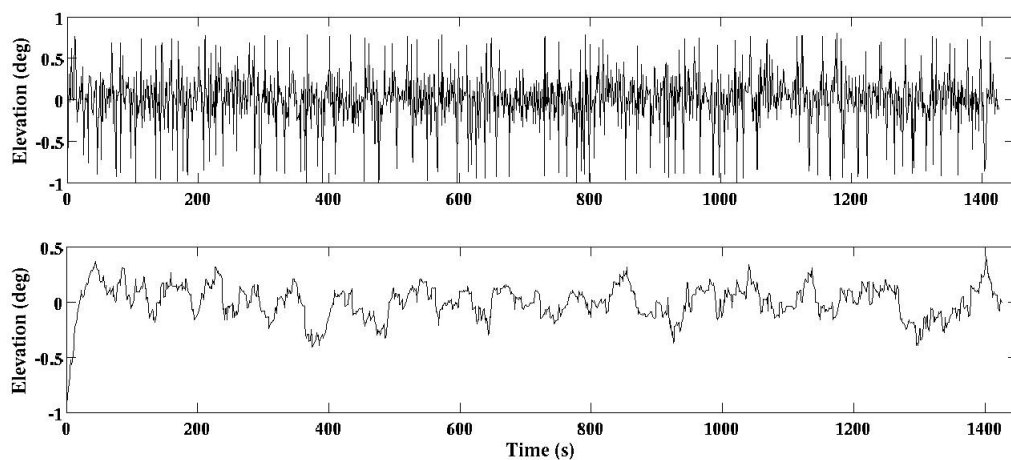


Figure 6.5: *Top:* Elevation calculated from the accelerometer shows considerable scatter. *Bottom:* The sensor-fused elevation data from accelerometer and gyroscope using Kalman-filter is much smoother.

6.3.4 Estimation of azimuth

We have estimated the azimuth of the balloon telescope using a magnetometer (HMC5883l) as in eq. 6.4, Where h_x and h_y are the magnetic field strength in x and y-axis of the magnetometer respectively. However, magnetic elements near to the magnetometer such as metal screws, the battery or electronics components may introduce hard-iron biases to the measurements. There are two main categories of measurement distortion sources: instrumentation errors and magnetic interferences. These biases must be compensated through calibration, since, uncalibrated hard-iron distortions will cause sig-

^m<https://github.com/TKJElectronics/>

nificant errors in the magnetometers estimated azimuth(Fig. 6.6).

$$AZI = \tan^{-1}\left(\frac{-h_y}{h_x}\right) \quad (6.4)$$

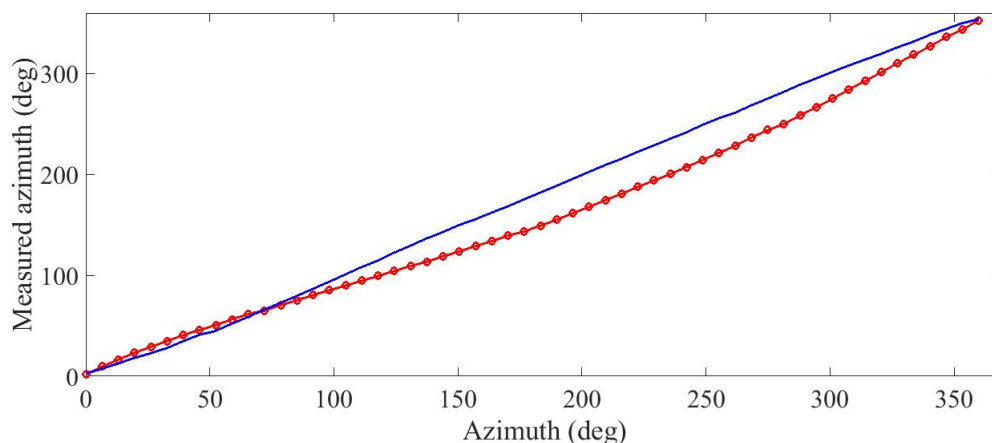


Figure 6.6: The figure shows the nonlinearity in magnetometer reading. The heading calculated from uncalibrated magnetometer measurements (line) and the heading calculated from calibrated magnetometer measurement (dots).

The measured magnetic field strength h_m from a magnetometer can be represented as in eq. 6.5, where A is a matrix which combines the effect scale factors, misalignments and soft-iron, b is the bias vector, and h is the actual magnetic field strength.

$$h_m = Ah + b \quad (6.5)$$

Hence the actual magnetic field h can be retrieved from the measured magnetic field as in eq. 6.6.

$$h = A^{-1}h_m - b \quad (6.6)$$

The earth's magnetic field at any location can be represented using a three dimensional vector. The locus of all these vectors measured on a location forms a sphere of radius F , where F is the magnetic field strength. An ellipsoid can be represented as in eq. 6.8 where $a, b, c, d, e, f, g, h, p, q$ and

r are the coefficients of the second degree polynomial S .

$$S : aX^2 + bY^2 + cZ^2 + 2fYZ + 2gXZ + 2hXY + 2pX + 2qY + 2rZ + d = 0 \quad (6.7)$$

We calibrated the magnetometer by rotating it many times and measuring the magnetic field strength in the three axes of the magnetometer. Figure. 6.7 shows the magnetic field strength in Earth centered inertial (ECI) frame and the ellipsoid fitⁿ. The matrices A^{-1} and b are found from the ellipsoid fit as in eq. 6.8 and eq. 6.9, where

$$M = \begin{bmatrix} a & f & g \\ f & b & h \\ g & h & c \end{bmatrix}$$

$$n = \begin{bmatrix} p \\ q \\ r \end{bmatrix}$$

and d are found from the ellipsoid fit.

$$b = M^{-1}n \quad (6.8)$$

$$A^{-1} = \frac{FM^{0.5}}{\sqrt{n^T M^{-1}n - d}} \quad (6.9)$$

We implemented the magnetometer calibration in the controller as in eq. 6.10, where a_{ij} and b_{ij} are the parameters estimated from ellipsoid fit, h_x, h_y , and h_z are the magnetic field strength measured by the magnetometer

ⁿ<http://in.mathworks.com/matlabcentral/fileexchange/23377-ellipsoid-fitting?requestedDomain=www.mathworks.com>

in x, y and z axis of the magnetometer respectively, h_{xx} and h_{yy} are the calibrated magnetic field strength in x and y axis.

$$h_{xx} = a_{11}h_x + a_{12}h_y + a_{13}h_z - b_{11} \quad (6.10)$$

$$h_{yy} = a_{21}h_x + a_{22}h_y + a_{23}h_z - b_{12}$$

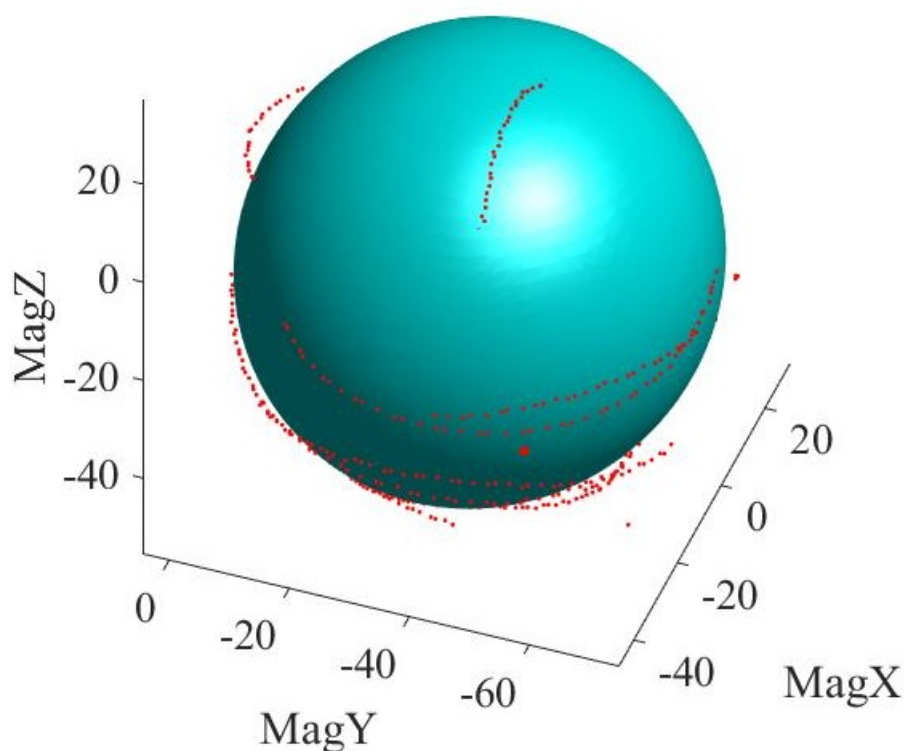


Figure 6.7: The magnetic field strength measured using the MEMS magnetometer. MagX, MagY, and MagZ are ADC readings correspond to the measured magnetic field strength in x, y, and z-axis of the magnetometer respectively. The red dots are the measured magnetic field strengths, and the green sphere is the ellipsoid fit.

Figure. 6.6 shows the difference in the azimuth (heading) calculated from the uncalibrated magnetometer readings and calibrated magnetometer readings. We were able to remove the nonlinearity in the azimuth estimation using the calibration (refer Fig. 6.6) and the error in azimuth calculation after calibration was found to be an RMS value of $\pm 0.1652^\circ$.

The magnetometer is tested and calibrated in the ground as explained in the previous section. However, the readings obtained from magnetometer may vary with altitude and may produce erroneous readings. Since we wanted

to use our pointing system at an altitude above 30 Km, it is necessary to know the variation of the magnetic field above that height. Therefore we obtained the variation of the earth's magnetic field with altitude from the model given by NOAA website^o. We found how the magnetic field (x,y component), declination angle (the difference between magnetic north and true north) and inclination angle (the angle made by horizon with Earth's magnetic field lines) with altitude. We have found this variation and plotted in Figure. 6.9. This analysis indicated that the variation in the magnetic field measurement

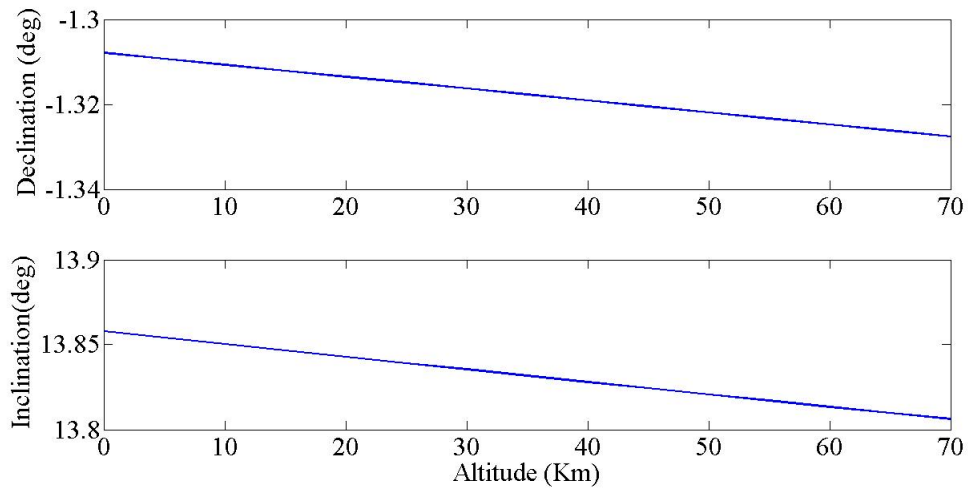


Figure 6.8: Variation in magnetic inclination and declination with altitude.

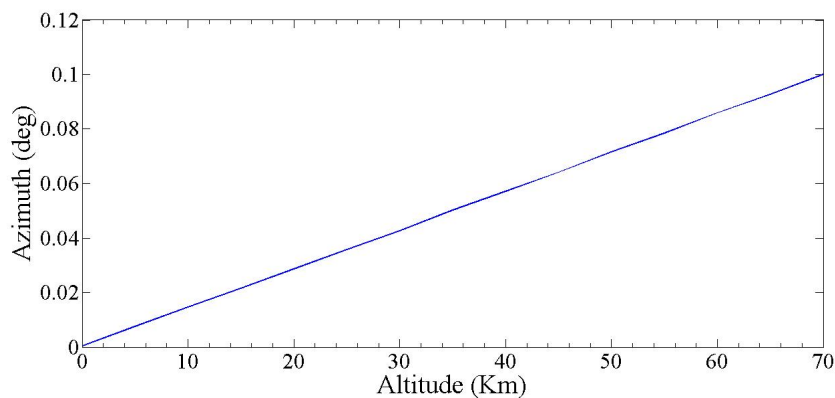


Figure 6.9: Variation in azimuth estimated from the magnetometer readings with altitude.

with altitude could affect the azimuth estimation in two ways.

1. As the altitude increases the declination angle changes. Hence a fixed

^o<http://www.ngdc.noaa.gov/geomag-web/>

declination angle cannot be used for azimuth correction.

2. There is a variation in the magnetic field strength with the altitude. Even though the pointed azimuth did not change, but the sensor reading might prompt different azimuth estimation.

However, from the analysis, we found that the variation in declination angle is $0,02^\circ$ and the variation in azimuth is 0.12° when the altitude changed from 0 to 70 Km which are within our required precision and neglected.

6.4 Checking the magnetometer calibration

We have checked the performance of the system on the ground by pointing it towards Moon. The equatorial coordinate of the Moon for the day of the experiment as well as the starting time of experiment was programmed into the controller, and the system is then taken to a convenient location and switched on. A camera was mounted on the system to take the pictures of Moon every 10 seconds during the experiment. We tested our system without any magnetometer calibration. The Moon's image obtained were far off from the center of the field of the camera (Fig. 6.10, *Top*). However, after magnetometer calibration, we got the Moon's image and the center of the field of view of the camera (Fig. 6.10, *Bottom*).

6.5 Correcting the pointing position

Before the implementation of a control system for pointing position correction, an estimate of the amount of the payload motion during the flight is required. Because light balloons are in constant motion, the payloads are usually subject to violent jerks and rotations, and other disturbances that the pointing control must reject. We have flown our attitude sensor (AS) in different balloon flights and estimated the payload motion in roll, pitch and yaw axes (tilt, elevation, and azimuth) during the flights. We inferred the



Figure 6.10: *Top:* One of the images taken during the ground test when the magnetometer was not calibrated. *Bottom:* The image of the Moon taken during the ground test where the magnetometer is calibrated for hard iron and soft iron biases. The position of the Moon is marked in a rectangle.

prerequisite of the pointing correction mechanism from this data and simulated a realistic model of our system in MATLAB. We have implemented a proportional-integral-derivative (PID) loop feedback algorithm in the simulation, and in the real system, to correct for the difference between the actual pointing and the desired pointing in a closed loop. We found that the results obtained from the simulation and the actual measurements were comparable.

6.5.1 Estimation of disturbances on the payload

We inferred from the AS data that our balloon flights have a turbulent phase while ascending, and a stable phase at high altitudes (above 19 km) (Fig. 6.11, Fig. 6.12), especially at float altitudes (~ 30 km) (Safonova et al., 2016). The motion of the payload during these stages is tabulated in Table. 6.2. The prerequisite parameters for our control system, such as settling time,

maximum peak overshoot and steady state error, are derived from this data.

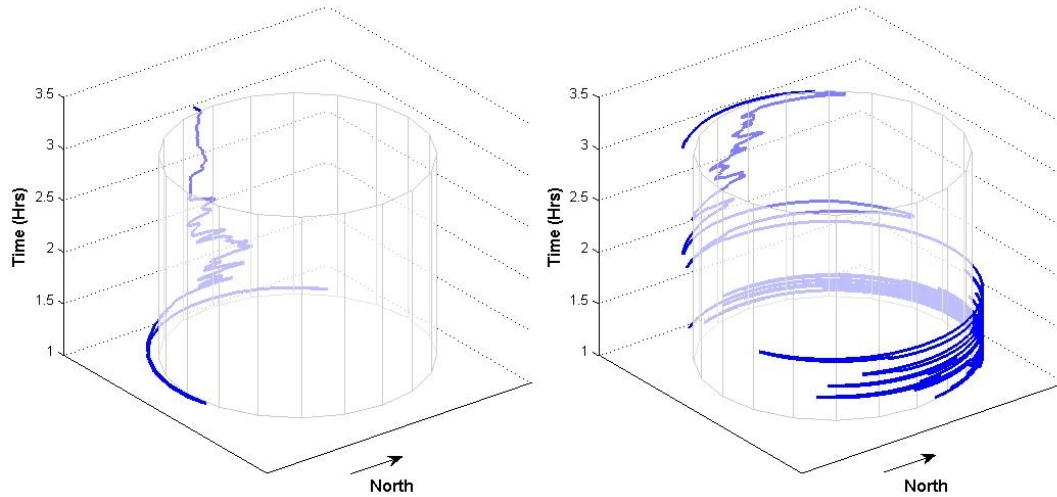


Figure 6.11: Wind direction (*Left*) and movement of the payload in azimuth (*Right*) after reaching the stratosphere. Time axis shows time in hours elapsed since launch. The float altitude was reached at about 2 hrs after launch. The plots clearly show the difference between the rapid variation of payload azimuth before reaching the final float altitude and less variation of payload azimuth after reaching the float altitude.

Table 6.2: Motion of the payload in elevation, azimuth and tilt.

Axis	Condition	RMS velocity ($^{\circ}/s$)
Azimuth	Turbulent	25.74
	Floating	0.20
Elevation	Turbulent	1.35
	Floating	0.01
Tilt	Turbulent	3.87
	Floating	0.01

1. The settling time of the system is 2 s.
2. The steady-state error of the system is zero.
3. The maximum peak overshoot is less than 20% of the required value.

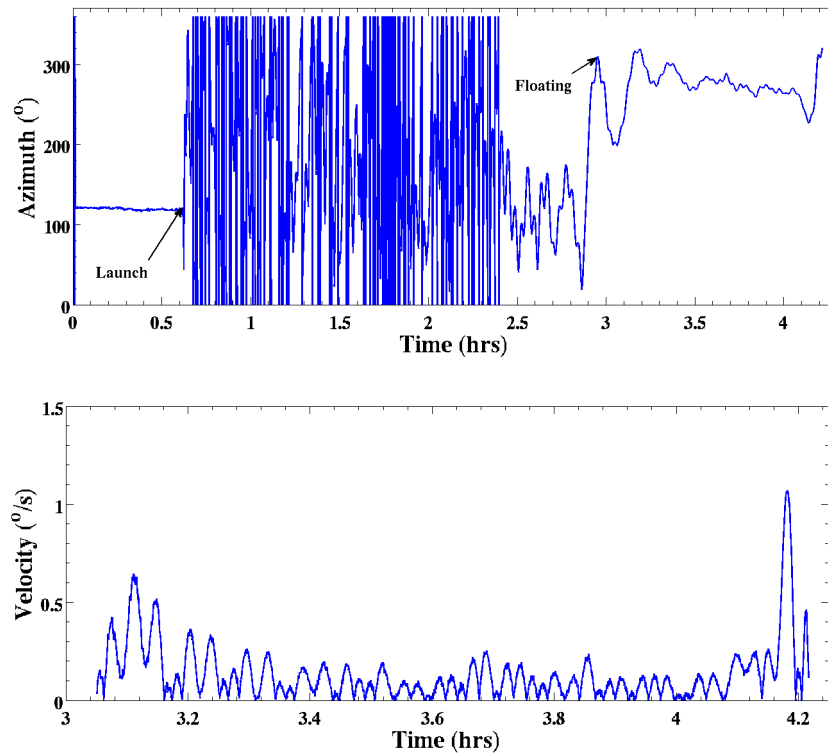


Figure 6.12: *Top:* The motion of the payload in azimuth during the balloon flight. *Bottom:* The rms velocity ($^{\circ}/s$) of the payload in azimuth.

6.5.2 Simulation of control system

Figure 6.13 shows control system model of our pointing system. The model constitutes an actuator and external gears, and the load is acting on the system. We used servomotor as an actuator in our system. Hence, a realistic model of a servomotor was simulated (Eq. 6.11), considering different internal parameters such as encoder gain, gear ratio, and DAC gain. The parameters of the servomotor used in Eq. 6.11 are tabulated in Table 6.3. The transfer function of the system is obtained after substituting all other external parameters, including gears and load (Eq. 6.12). The closed-loop step response (the response of the system when the motor shaft is forced to move by 1 rad) of the system is shown in Fig. 6.14, *Top*. However, this response did not satisfy our design requirements (Table 6.4). Therefore, an external proportional-integral-derivative (PID) algorithm was introduced in the feedback path of the system (Fig. 6.13) to correct for the difference between the

actual pointing and the desired pointing in a closed loop.

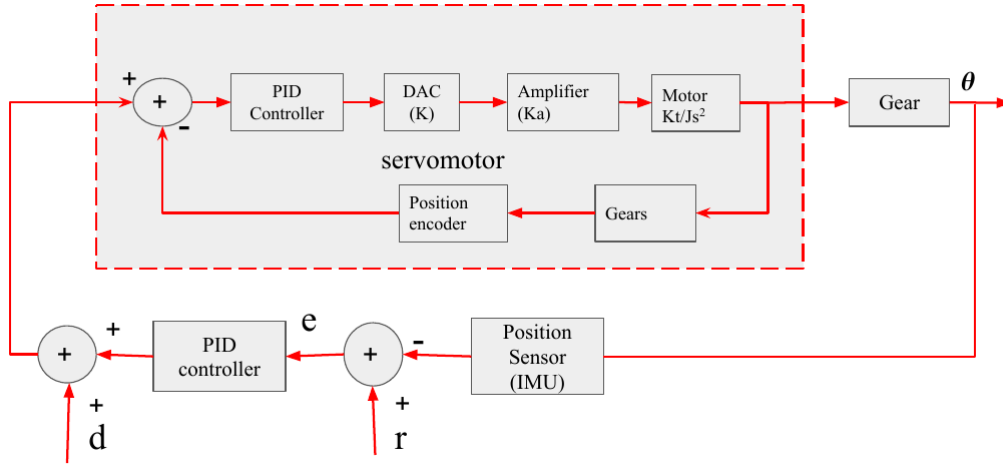


Figure 6.13: A block diagram of control system model, where \mathbf{r} is the control signal, \mathbf{d} is the disturbance (load), \mathbf{e} is the error signal and θ is the angle rotated by the motor shaft.

$$\frac{\theta(s)}{V(s)} = \frac{K_t \times G \times K_G \times K_{DAC}}{s((J_r s + b)(Ls + R) + K_t^2)}. \quad (6.11)$$

Table 6.3: ACS programmed parameters.

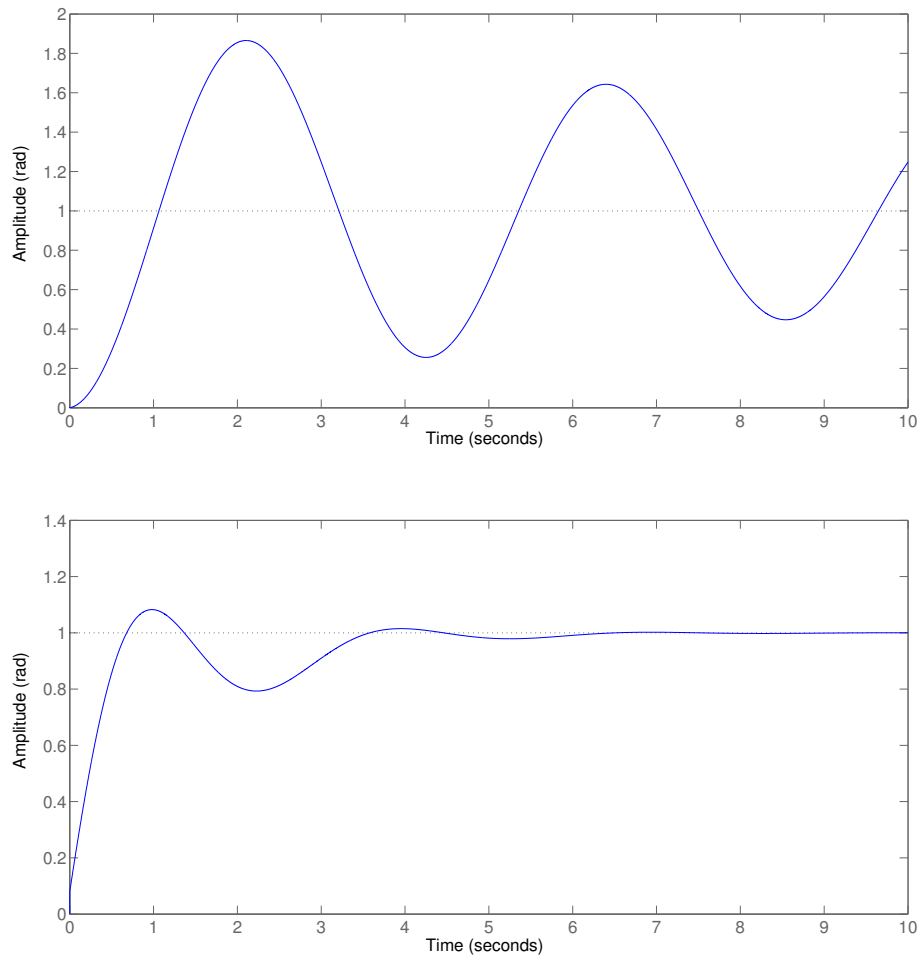
J_r	Moment of inertia of the rotor	$0.993 \times 10^{-7} \text{ kg m}^2$
b	Motor viscous friction constant	$72.4 \times 10^{-6} \text{ N m sec}$
K_b	Electromotive force constant	0.011 V/rad/sec
K_t	Motor torque constant	0.0112 N m/A
R	Electric resistance	11.4Ω
L	Electric inductance	$343 \times 10^{-6} \text{ H}$
G_{in}	Internal gear ratio	$1/193$
G_{ex}	External gear ratio	$1/2$
G	Total gear ratio	$1/386$
K_G	Encoder gain	651.8 unit/rad
K_{DAC}	Gain of DAC	0.0468 V/unit

The system response depends on the values of the constants K_p , K_i and K_d – gains of the proportional, integral and differential error, respectively. In our simulation, we have tested different gain values, and obtained a satisfactory result (Table 6.4) for $K_p = 2$, $K_d = 1$ and $K_i = 2$ for the load simulating the real load intended on the system (star sensor of $\sim 500 \text{ g}$). The comparison of the step response of the system without the external PID controller and with the controller is given in Fig. 6.14.

Table 6.4: The closed loop step response parameters without and with an external PID

Parameter	no PID	with PID
Rise Time (sec)	0.73	0.53
Settling Time (sec)	56	5.4
Overshoot (%)	86.3	8.2
Peak (rad)	1.86	1.1

$$\frac{\theta(s)}{V(s)} = \frac{887 \times 10^{-6}}{3.098 \times 10^{-07}s^3 + 0.0103s^2 + 0.0009509s}. \quad (6.12)$$

**Figure 6.14:** The closed loop step response of the system. *Top:* without the PID controller, *Bottom:* with the PID controller of gain $K_p = 2$, $K_d = 1$ and $K_i = 2$. The settling time is reduced to the satisfactory value.

6.5.3 Hardware implementation of the PID algorithm.

We implemented a PID control algorithm in the Arduino controller as depicted in Fig. 6.15. The step response of the system for different PID gains is given in Fig. 6.16. Fast and stable response achieved with gain values $K_p = 2$, $K_i = 1$, $K_d = 2$ (*Middle*), similar to the gain values obtained from the modelling under load condition.

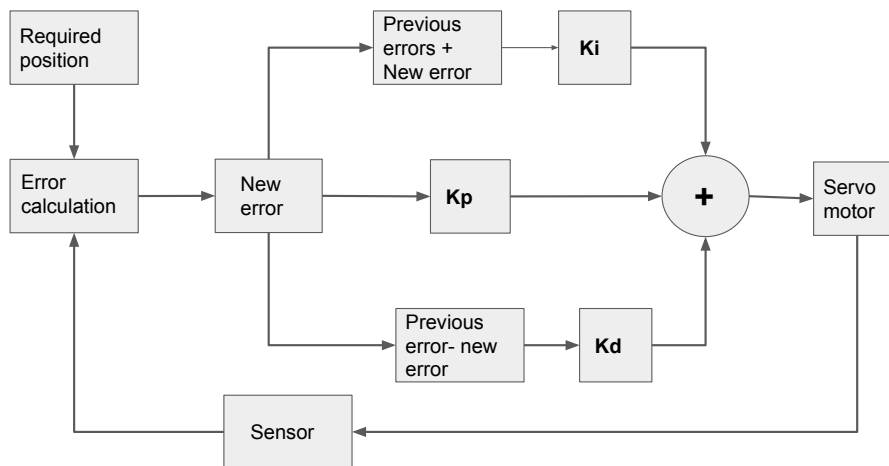


Figure 6.15: Block diagram of the PID algorithm implemented in the controller.

6.6 Pointing System Program Flowchart

The flowchart (Fig. 6.17) shows the program flow inside the controller. We have done the programming on the Arduino platform.

6.7 Performance tests

The calibration and testing of the individual sensors and the attitude sensor as a complete unit have been discussed in Sreejith et al. (2014). In the next sections, we describe the testing of the pointing system for pointing

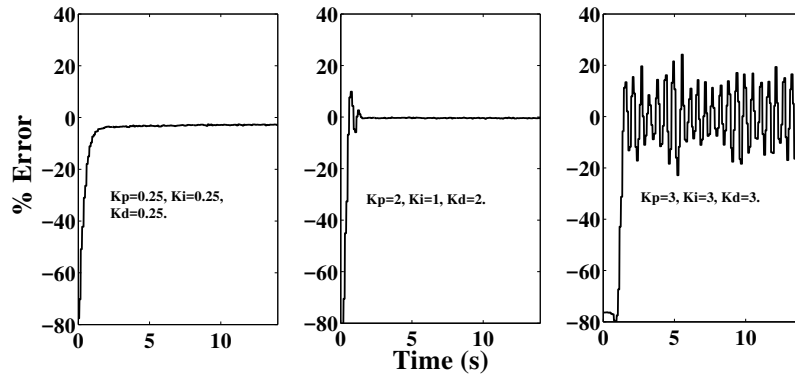


Figure 6.16: The response of the PID controller for different proportional, integral and differential gains. Y -axis shows the deviation in percentage between the programmed and current position. For $K_p = 0.25$, $K_d = 0.25$, $K_i = 0.25$, the system response is slow (*Left*). Fast and stable response achieved with gain values $K_p = 2$, $K_i = 1$, $K_d = 2$ (*Middle*). For gains $K_p = 3$, $K_d = 3$, $K_i = 3$, the system becomes unstable and starts oscillating (*Right*).

accuracy and stability performance, both on the ground and in tethered flights. Pointing accuracy is determined as for how accurately the system points towards the actual position of an object. Pointing stability (precision) is determined as for how well the system maintains the pointing position over time.

6.7.1 Ground test

Performance test of our pointing system was done under controlled conditions on the ground. We mounted a camera and an external IMU (x-IMU^P) on the inner frame of pointing system and programmed the system to point towards different celestial objects (Sun, Moon, Sirius and Jupiter) and tracked them for a duration of at least 15 minutes, with the camera recording a video (30 frames per second) of the object under observation. We performed this test on, at least, three nights for each object. Pointing accuracy of the system was found by comparing the pointing direction (elevation and azimuth) calculated by the controller and executed by the pointing system, and the direction measured by the x-IMU. The RMS pointing accuracy was within $\pm 0.28^\circ$.

^P<http://www.x-io.co.uk/products/x-imu/>.

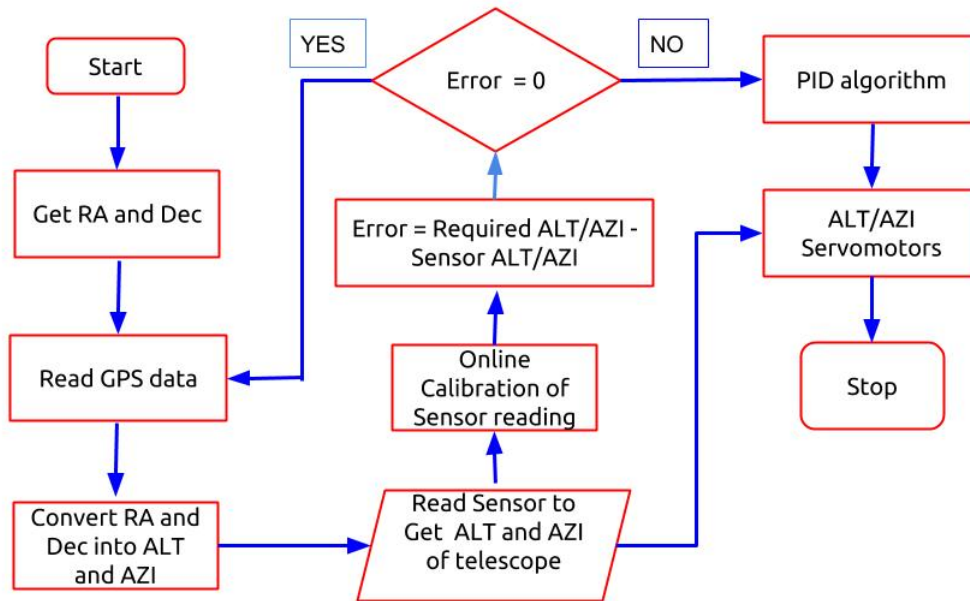


Figure 6.17: A Program flowchart of the ACS.

Stability of the system (pointing precision) was determined by taking the centroid of an object's image (from isophotes) in each 1.5 sec frame and finding the shifts (in degrees) between the centroid in the first frame (reference frame) and all subsequent frames. The average centroid shift for all objects was found to be $\pm 0.13^\circ$.

In Fig. 6.18, we show an example image of the Sun (*Left*), the isophote (*Middle*) of the image, and the shifts between the centroids (*Right*). The RMS of the centroid shift for every tracked object is given in the last column of Table 6.5.

6.7.2 Tethered flights

We simulated conditions similar to the balloon flight using a tethered launch. The payload, containing the pointing system (Fig. 6.21) with mounted attitude sensor, a digital camera, batteries, and a radio tracker, was placed on a star-shaped platform. The platform 'wings' were tied to a parachute by the nylon rope, and the parachute was attached to balloon as shown in Fig. 6.19,

Table 6.5: Ground test results of tracking stability

	Object	Actual RA	Actual Dec	Centroid shift (\pm)
Test1 23/03/2016	Moon	185.223°	-0.853°	0.129°
	Sirius	101.284°	-16.722°	0.172°
	Sun	2.531°	1.099°	0.119°
	Jupiter	167.193°	7.170°	0.112°
Test2 24/03/2016	Moon	196.601°	-4.633°	0.153°
	Sirius	101.284°	-16.722°	0.101°
	Sun	3.443°	1.490°	0.168°
	Jupiter	167.193°	7.170°	0.100°

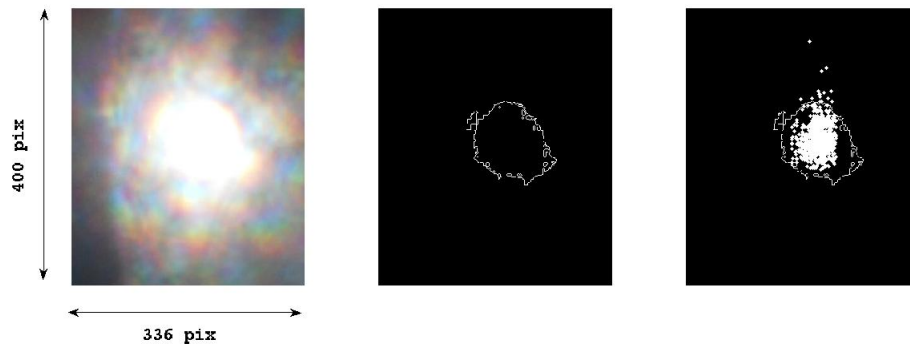


Figure 6.18: *Left:* An image (the Sun) frame extracted from the video capture during the ground test. *Middle:* The isophote of the Sun's image scaled by 250:1. This isophote was used to find the centroid of the image. *Right:* The isophote of the Sun with overlaid centroids calculated for every image frame. The size of an image is marked in pixels.

through a Nylon rope of approximately 7 m in length. Besides, the balloon was tethered through a nylon rope of approximately 200 m, which was fixed to a spindle on the ground. This launch aimed to point at and track the Sun, take images of the Sun and estimate pointing accuracy and stability. The UT starting time of the experiment and equatorial coordinates of the Sun were programmed into the ACS. The operation of the camera was adjusted to take the image every 5 seconds with an exposure time of 0.1 milliseconds. This experiment was conducted three times over a period of four months.

We tested pointing accuracy and stability of our pointing system in three tethered flights. We pointed towards either the Sun or the Moon, depending



Figure 6.19: The star-shaped platform is connected to the balloon through a parachute. The entire system is tethered to a spindle on the ground (not shown in figure) using a nylon tether of approximately 200 m length.

on the time of the day. While these launches do simulate actual flights, they are buffeted by stronger winds than at the high altitudes we usually fly (Manchanda et al., 2011) and thus put greater stress on the pointing system. In each flight, the payload included the pointing system mounted on a star-shaped platform, a camera mounted on the pointing system, and an IMU (x-IMU), mounted on the platform. The camera was programmed to take an image every 5 sec, and the data were stored on-board along with the IMU data (Euler angles of the payload position during the flight).

We have classified these tethered flights into two phases: stable and unstable, based on the motion of the platform. If the payload motion was below $25^\circ/\text{sec}$ in azimuth and $4^\circ/\text{sec}$ in elevation, we classified it as stable, and as unstable otherwise. The winds were particularly bad in one of the flights, and several times the payload hit the surrounding trees and even the ground. However, the pointing system continued to perform throughout the total duration of the test (though sometimes the rotational motion of payload was reaching $90^\circ/\text{sec}$ due to strong winds).

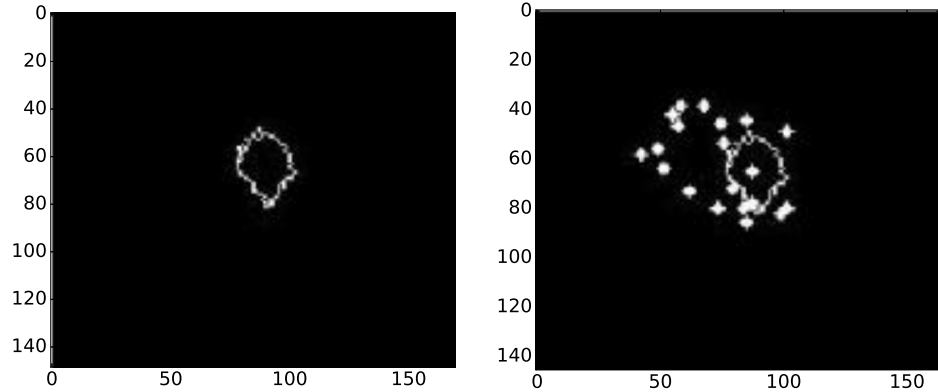


Figure 6.20: *Left:* Isophote of the Sun’s image obtained during a tethered flight. *Right:* Individual centroids of the Sun in each of the 5 second frames are plotted on the over a period of 150 seconds. Scaling is the same as in Fig. 6.18.

The images taken during above mentioned periods were identified from the image time stamp. In order to find the stability of pointing, we applied the same method as in the ground test: took the first frame as the reference frame, and found the Sun’s image centroid. The stability was measured by the shifts (in degrees) in the image centroid on every successive frame concerning the reference frame (Fig. 6.20). In the stable phase, the RMS of the centroid shifts was 0.844° , which is mainly due to the motion of the payload in the third axis (here, tilt), which contributed disproportionately to the pointing precision. During the periods when this motion was small, less than 0.1° (the least winds), the stability improved to within 0.4° . This pointing system is the first step towards building a star sensor-based pointing system, where the system described in the paper acts as a coarse correction for pointing direction, and fine correction will be done after the input from the star sensor which has wide FoV of 10 degrees. Hence, the function of this system is initially to get the object inside the FoV of the star sensor camera. Therefore we find the performance of the system satisfactory.

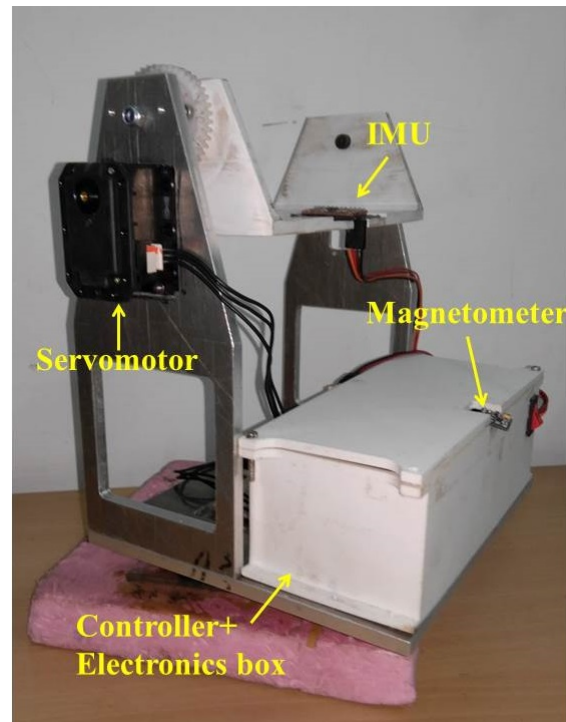


Figure 6.21: The structure of the gimbal system. Different components used and their position on the gimbal is also marked. The azimuth frame is made of Aluminium, and the elevation frame is made of ABS plastic to reduce weight.

6.7.3 Technical Specifications of the Controller

We used the Mega controller in our system. The reason behind using Arduino mega controller is that it is easy to program, there are so many libraries available on the internet. The technical details of the system are given in Table. 6.6.

6.7.4 Power requirement

The power requirement of the system comes from the controller, sensors, and servomotors. We used Lithium polymer batteries for this purpose. The battery decided for this purpose is 11.1 V, 5 Ampere-hour battery. The power requirement for these components are listed below in Table. 6.7

Microcontroller	ATmega2560
Operating Voltage	5V
Input Voltage (recommended)	7-12V
Input Voltage (limit)	6-20V
Digital I/O Pins	54 (15 PWM output)
Analog Input Pins	16
DC Current per I/O Pin	20 mA
DC Current for 3.3V Pin	50 mA
Flash Memory	256 KB, 8 KB bootloader
SRAM	8 KB
EEPROM	4 KB
Clock Speed	16 MHz
Length	101.52 mm
Width	53.3 mm
Weight	37 g

Table 6.6: Technical specification of Arduino Mega controller.

Table 6.7: Power requirement of various components in pointing system

components	Voltage (V)	Current (mA)	power (W)
Arduino controller	5	20	0.1
IMU MPU 9150	3.3	10	0.03
Actuator	12	1.4 A and 100 mA	16
GPS	5	20	0.1
x-IMU	3.5to 6.3	50 to 150	0.975

6.7.5 Data Handling

The communication between different modules (IMU, magnetometer and GPS) and controller is given in the Table. 6.8

Sensor	Communication	pins	Speed
IMU	I2C	SDA,SCL	100Kbps, 400Kbps,1Mbps
Magnetometer	I2C	SDA,SCL	100Kbps, 400Kbps,1Mbps
GPS	UART	Rx,Tx	9600bps
x-IMU	UART	Rx,Tx	9600bps

Table 6.8: Details about data transfer between controller and sensor modules

6.7.6 Technical Specifications about motor

We selected servomotor⁹ for some specific reasons. The size, weight of servomotor is much less compared with the size and weight of stepper motor.

⁹<http://www.trossenrobotics.com/dynamixel-mx-28-robot-actuator.aspx>

The technical specifications of the motor is given in the Table. 6.9.

Table 6.9: Technical specifications of the Servomotor

Details	Value
Operating Voltage	12V
Weight	72g
Stall torque	2.5 N.m
No load speed	55 rpm
Size	35.6 x 50.6 x 35.5 mm
Resolution	0.088°
Reduction Ratio	193 : 1
Operating Angle	0°360° or Continuous Turn
Max Current	1.4A @ 12V
Standby Current	100 mA
Operating Temp	-5°C 80°C
Protocol	TTL Asynchronous Serial
Module Limit	254 valid addresses
Com Speed	8000bps 3Mbps

6.8 Summary

In this chapter, we have discussed the design and development of a lightweight pointing system for balloon platforms. The system was built using off the shelf component such as Arduino microcontroller, Dynamixel MX series servo motors, MPU 9150 IMU and HMC5883L magnetometer. We have also described different tests we have conducted to evaluate the system.

Chapter 7

Summary and Future work

7.1 Summary

SHS is a compact, rugged instrument with high resolving power and a narrow but tunable bandpass. We have recalled the concept and design of a tunable spatial heterodyne spectrometer in refractive configuration, where we use the beam splitter to split the incoming light. Compared with the all-reflective tunable configuration of SHS, our refractive design instrument is simple since we do not use a roof mirror and fold mirror. The instrument can be tuned to cover a wavelength range from 350 nm to 700 nm with a resolving power of approximately 28000 and is designed for the emission line sources. Based on the Zemax[®] simulation of the model, we have procured the components and assembled the instrument on the optical breadboard. We have tested the instrument using a sodium vapor lamp and a halogen lamp monochromator. The spectrum of the sodium vapor lamp was retrieved from the interferogram. We have also carried out ground-based observations using the TSHS with the optical telescope (VBT) and developed a Python-based pipeline for spectrum retrieval. The primary objective of the instrument is to study the H_α lines from red dwarfs and Be stars. However, with our current design and components, we could only observe bright stars, such as Sirius and

Betelgeuse.

We have also designed and developed a low-cost light-weight, closed-loop pointing and stabilization platform for use in balloon-borne astronomical payloads. This system built entirely from off-the-shelf components: an MPU-9150 IMU, an HMC5883L magnetometer, an Arduino controller and a SiRF StarIII GSC3f GPS receiver unit. The system performance was checked on the ground and in tethered flights with satisfactory results. The system can point to an accuracy of $\pm 0.28^\circ$ and track objects from the ground with an accuracy of $\pm 0.13^\circ$. The performance in the tethered flights was poorer (0.40° in best conditions), mainly because of strong winds at low altitudes. However, the stability of the pointing was still within $\sim 1.6^\circ$ even in the worst conditions. Such winds are not present in the stratosphere Manchanda et al. (2011), where payloads are known to be stable at float Safonova et al. (2016), and we expect pointing accuracy and stability of our system to be similar to those on the ground.

7.2 Future works

Spatial Heterodyne spectrometer

In future, we are planning to improve the instrument using a better detector. This instrument can be modified to UV regime to fly on a balloon or satellite platform as a field-widened monolithic SHS (Doe et al., 2011), which will require additional studies on field-widening techniques.

In order to increase the sensitivity of the instrument, field widening (Harlander et al., 2002) technique can be used. A schematic diagram of the field widened SHS is given in Fig. 7.1. The FOV of the SHS system without a field-widening prism is $2.13 \times 10^{-4} sr$ with a resolving power of 28000. Thus, monochromatic fringes would have the highest contrast at the center of the field (beam-width) reducing towards the edges due to the fringes going out of phase from center to edges. The phase difference has an effect on the

fringe envelope as it gets modified from a rectangular function to a rectangular function multiplied by a sinc function, reducing the resolution of the system. Therefore, as the ray deviates more from the axis, the resolution of the system also reduces. The throughput and SNR of the system can be improved by field widening, which is accomplished by introducing a refractive material in the SHS arms. Usually, a field-widening prism is used for this purpose. The angles of the fixed prism in the SHS arms are chosen in such a way that it rotates the grating's image so that it appears normal to the optical axis. The maximum field of view η that can be achieved with the

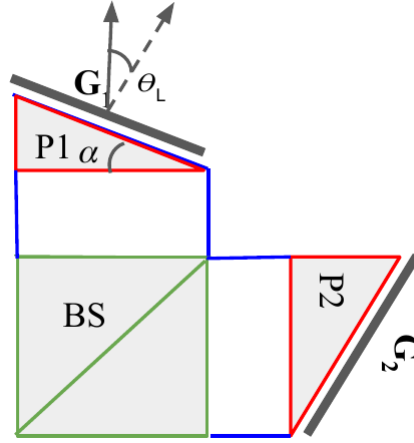


Figure 7.1: A schematic diagram of the field widened SHS.

prism of refractive index n is given by

$$\frac{n^2 - 1}{n^2} \tan \eta \frac{2n^2 - \sin^2 \eta}{n^2 - \sin^2 \eta} = \tan \theta_L. \quad (7.1)$$

The prism apex angle α can be calculated from η as

$$n \sin \frac{\alpha}{2} = \sin \eta. \quad (7.2)$$

7.2.1 Selection of material

Selection of materials for field widening prism should be made carefully. The refractive index of the glass varies with the wavelength. Hence the refractive

index of the glass corresponding to the particular wavelength should be found for the estimation of FOV and apex angle as in eq. 7.1, eq. 7.2. We studied different glass materials which can be used for field widening prism from the Schott glass catalog. The wavelength of interest in our case is 656.281 nm, hence the refractive index for this wavelength is found using Sellmeier dispersion formula as in eq. 7.3, where n is the refractive index, λ is the wavelength, $B_{1,2,3}$ and $C_{1,2,3}$ are Sellmeier coefficients, and is tabulated in Table. 7.1

$$n^2(\lambda) = 1 + \frac{B_1\lambda^2}{\lambda^2 - C_1^2} + \frac{B_2\lambda^2}{\lambda^2 - C_2^2} + \frac{B_3\lambda^2}{\lambda^2 - C_3^2} \quad (7.3)$$

Table 7.1: The refractive index of different glass from Schott glass catalog calculated using Sellmeier dispersion formula.

Glass	$n@H_\alpha$
FK5	1.4853
K10	1.4987
BK7	1.5143
KF9	1.5204
LLF1	1.5446
BaK4	1.5657
LF5	1.5772
F5	1.5987
SK4	1.6095
SF5	1.7472

In order to evaluate the variation of the refractive index of the material with temperature T , we used the formula displayed in Eq. 7.4, where the constants $D_0 - D_2, E_0$ and E_1 are found from Schott glass catalog and are presented in Fig.7.2.

$$\frac{dn}{dT} = \frac{n^2 - 1}{2n} \left(D_0 + 2D_1\Delta T + 3D_2\Delta T^2 + \frac{E_0 + 2E_1\Delta T}{\lambda^2 - \lambda_{TK}^2} \right) \quad (7.4)$$

In the future, we wanted to study the H_α emission from the Be stars. A

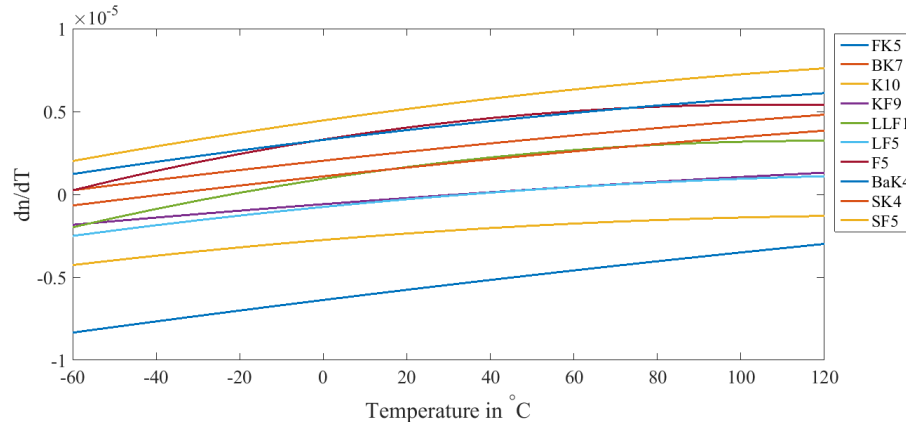


Figure 7.2: The rate of change of refractive index of different glasses with respect to temperature is plotted against temperature.

Be star is non-super giant B type star whose spectrum contains one or more Balmer series lines. Be stars are also variable star whose magnitude varies with time. The spectrum, as well as the variability of the Be star, indicates a presence of gaseous disk around the star. Due to the rotation of the disk around the star Be stars have strong H_{α} emission line that varies with time and the shape of the emission line changes with time as well as stars. An example of Be star H_{α} emission spectrum is given in Fig. 7.3.

Pointing system

We are exploring several avenues to improve further the system performance including using better sensors and servomotors with finer steps. We have developed a star-sensor (Sarpotdar et al., 2017) with a resolution of $30''$ which we will patch into the pointing system. We would like to improve the pointing system performance with the star sensor. The coarse pointing correction will be done with the MEMS sensor, and the fine pointing correction will be done with the star sensor (refer Fig. 7.5). An artistic representation of the pointing system with star sensor incorporated is given in Fig. 7.4. We plan to have a high-altitude floating balloon flight in November 2018 with an imager and a spectrograph where this pointing system will be put to use (Ambily et al., 2016; Sreejith et al., 2016).

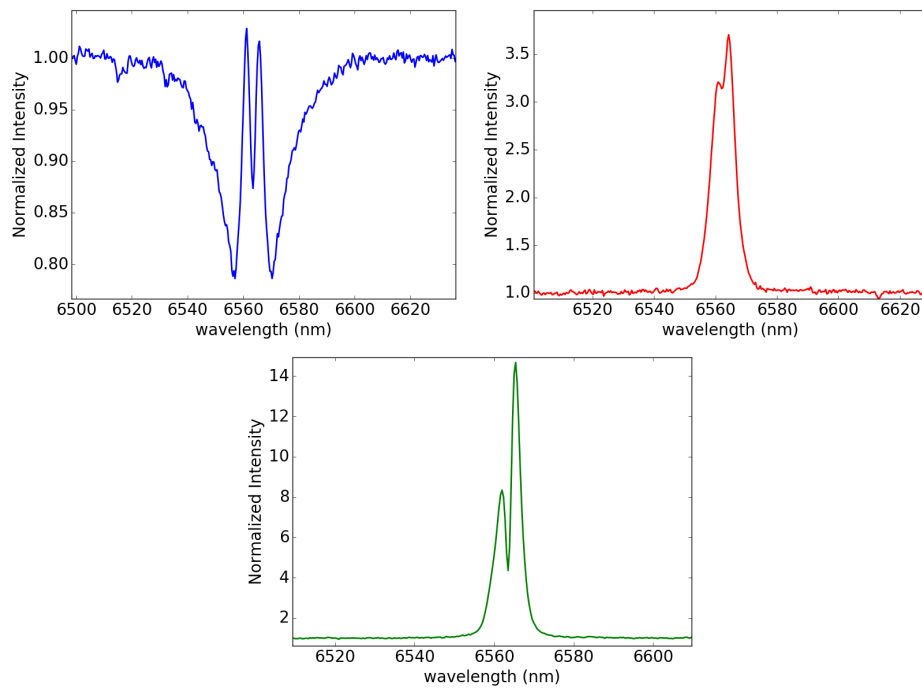


Figure 7.3: The H_α of different Be stars (Top) HD225132, (Middle) HD11606, (Bottom) HD50138.

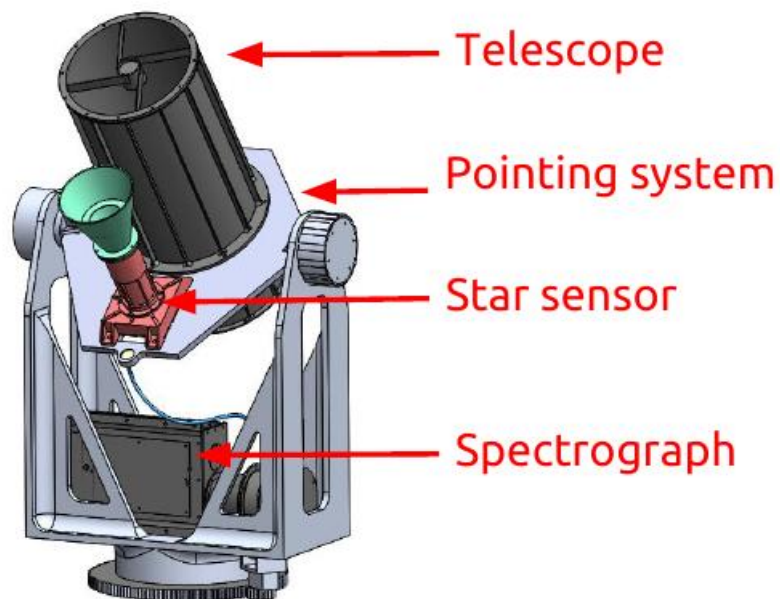


Figure 7.4: The mechanical structure of the whole system assembled.

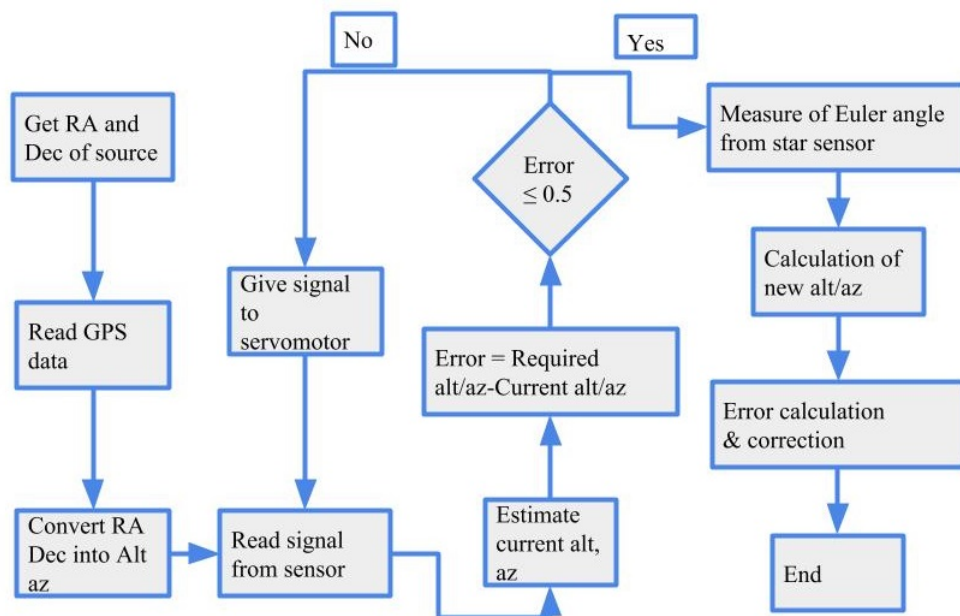


Figure 7.5: A flowchart showing the program flow in the pointing system incorporated with the star sensor.

Bibliography

Carl. A Zeiss,"Guiding System of the SpectroStratoscope", IEEE Trans on Aerospace and Electronic Systems, AES-5, pp.330-336,(1969).

D.J.McCarthy, "Operating Characteristics of the Stratoscope II Balloon Borne Telescope ", IEEE Trans on Aerospace and Electronic Systems, AES-5, Issue:2, pp.323-329, (1969).

Arabash S.V., Ivanov D.S., Ovchinnikov M.Yu., Tkachev S.S, "Balloon payload attitude control system", Keldysh Institute preprints, No. 15, 26 p. (2010).

Scott Milligan,James W. Howard,Bryan E. Laubscher,Barham W. Smith,Ralph R. Berggren,John M. Harlander,"Optical design of an imaging spatial heterodyne infrared spectrometer", Proc.SPIE, 3698,(1999).

John M. Harlander,^{1,*} James E. Lawler,² Jason Corlisset al., "First results from an all-reflection spatial heterodyne spectrometer with broad spectral coverage, OPTICS EXPRESS, Vol. 18, No. 6, March (2010).

Edwin J. Mierkiewicz,Fred L. Roesler,John M. Harlander,Ron J. Reynolds,Kurt P. Jaehnig, "First light performance of a near-UV spatial heterodyne spectrometer for interstellar emission line studies", Proc.SPIE, 5492, 5492 - 5492 - 16, (2004).

Kenneth D. Marr,Christoph R. Englert,John M. Harlander, "Measurement

and modeling of the thermal behavior of a laboratory DASH interferometer", Proc.SPIE, 8493, 8493 - 8493 - 7, (2012).

Christoph R. Englert, David D. Babcock, John M. Harlander, "Spatial heterodyne spectroscopy for long-wave infrared: first measurements of broadband spectra", Optical Engineering, 48, 48 - 48 - 9, (2009).

Steven M. Watson, N. Olson, R. P. Dalley, W. J. Bone, Robert T. Kroutil, Kenneth C. Herr, Jeff L. Hall, G. J. Schere, M. L. Polak, Thomas D. Wilkerson, Dennis M. Bodrero, R. O. Borys, D. Lowenthal, "Atmospheric properties measurements and data collection from a hot-air balloon," Proc. SPIE 2366, Optical Instrumentation for Gas Emissions Monitoring and Atmospheric Measurements, (1995).

Jean-Michel Lamarre, Guy Serra, Francois Pajot, Martin Giard, P. Encrenaz, "French activity in infrared astronomy from stratospheric balloons," Proc. SPIE 1341, Infrared Technology XVI, (1 November 1990).

Hideyo Kunieda, "Balloon-borne hard x-ray imaging observations of non-thermal phenomena," Proc. SPIE 6266, Space Telescopes and Instrumentation II: Ultraviolet to Gamma Ray, 62660B (20 June 2006).

J. Harlander, F. L. Roesler, "Spatial heterodyne spectroscopy - A novel interferometric technique for ground-based and space astronomy", Proc. SPIE, 1235, 622-633, july,(1990).

W. Harris, F. Roesler, E. Mierkiewicz, "Applications of UV Spatial Heterodyne Spectroscopy for High Spectral Resolution Studies of Diffuse Emission Line Sources in the Solar System", Bulletin of the American Astronomical Society, 35, 1003, 41.13, may,(2003).

J. Harlander, R. J. Reynolds, F.L Roesler, "Spatial heterodyne spectroscopy for the exploration of diffuse interstellar emission lines at far-ultraviolet wavelengths", ApJ, 396, 730-740, september,(1992).

- P. Hariharan, "Basics of INTERFEROMETRY", Elsevier, (2007).
- F. L Roesler, J. Harlander, R. Conway, M. E. Summers, "Spatial Heterodyne Spectrometer: A Compact Robust Interferometer for Optical Spectroscopic OH Measurements in the Solar System", AAS/Division for Planetary Sciences Meeting Abstracts", 31,1120,september,(1999).
- W. M. Harris, F. L. Roesler, K. H. Nordsieck, "Studies of H Ly- α emissions in the solar neighborhood with the techniques of polarimetry and spatial heterodyne spectroscopy (SHS)", Future EUV/UV and Visible Space Astrophysics Missions and Instrumentation, Proc. SPIE, 4854, 676-685,february,(2003).
- J. Harlander, J. E. Lawler, Jason Corliss, F. L. Roesler, Walter M. Harris, "First results from an all-reflection spatial heterodyne spectrometer with broad spectral coverage", OPTICS EXPRESS, 18, 6205-6210,march,(2010).
- S. Hosseini, W. Harris, J. Corliss, "Khayyam: a tunable spatial heterodyne spectrometer for observing diffuse emission line targets", Ground-based and Airborne Instrumentation for Astronomy IV", Proc. SPIE, 8446, 8446 - 8446 - 11, september,(2012).
- C. P. Perkins, J. P. Kerekes, M. G. Gartley Rochester, "Spatial heterodyne spectrometer: modeling and interferogram processing for calibrated spectral radiance measurements", Imaging Spectrometry XVIII, Proc. SPIE, 8870, 8870 - 8870 - 14,september,(2013).
- P. D. Feldman, "Comets", "Science with the Hubble Space Telescope - II", 525,(1996)
- N. Biver, "Cometary spectroscopy", Astronomical Spectrography for Amateurs, EAS Publications Series, 47, 165-188,april,(2011).

- Hosseini, Sona, "Tunable Reflective Spatial Heterodyne Spectrometer: A Technique for High Resolving Power, Wide Field Of View Observation Of Diffuse Emission Line Sources", Ph.D. Dissertation, july,(2015).
- M. K. Tahic, D. A. Naylor, "Apodization Functions for Fourier Transform Spectroscopy", Technical Digest, Optical Society of America,(2005).
- Christoph R. Englert, John M. Harlander, "Flat-fielding in spatial heterodyne spectroscopy", APPLIED OPTICS,45, 4583-4590, july,(2006).
- Richard A. Doe, Steven Watchorn", "Climate-monitoring CubeSat mission (CM2): a project for global mesopause temperature sensing", Proc.SPIE, 8153,8153 - 8153 - 12,(2011).
- J.M. Harlander, F.L. Roesler, C.R. Englert, J.G. Cardon, Conway R.R., Brown C.M., Wimperis J., "Robust monolithic ultraviolet interferometer for the SHIMMER instrument on STPSat-1", APPLIED OPTICS,42, 2829-2834, may,(2003).
- William A. Gault, Sean F. Johnson, David J. W. Kendall, "Optimization of field-widened Michelson interferometer", APPLIED OPTICS,24,june,(1985).
- John M. Harlander, Huan Tran, Fred L. Roesler , Kurt P. Jaehnig, Scott M. Seo, Wilton T. Sanders, Ronald J. Reynolds, "Field-widened spatial heterodyne spectroscopy: correcting for optical defects and new vacuum ultraviolet performance tests", Proc.SPIE, 2280,(1994).
- John M Harlander, Fred L. Roesler, Joel G. Cardon, Christoph R. Englert,Robert R. Conway, "SHIMMER: a spatial heterodyne spectrometer for remote sensing of Earth's middle atmosphere", APPLIED OPTICS, 41, march, (2002).
- Olivia R. Dawson, Walter M. Harris, "Tunable all-reflective spatial heterodyne spectrometer for broadband spectral line studies in the visible and near-ultraviolet", APPLIED OPTICS,48, 4227-4238,july,(2009).

- J. Moulataka, S. A. Ilovaisky, P. Prugniel, C. Soubiran, "The ELODIE Archive", *PASP*, astro-ph/0405025,116,693-698,july,(2004).
- , L. M. Fissel, P. A. R. Ade, F. E. Angilè, "The balloon-borne large-aperture submillimeter telescope for polarimetry: BLAST-Pol", *Pro. SPIE*, 7741, (2010).
- , B. P. Crill, P. A. R. Ade, J. J. Bhatia,"BOOMERANG: A Balloon-borne Millimeter-Wave Telescope and Total Power Receiver for Mapping Anisotropy in the Cosmic Microwave Background",*apjs*,148, 527-541, (2003.)
- E. Pascale, P. A. R. Ade, J. J. Bock et al.,"The Balloon-borne Large Aperture Submillimeter Telescope: BLAST", *apj*,681,(2008).
- P. Savvidis and D. Anderson and M. Grimble and et al., "Application of nonlinear generalised minimum variance to the nadir problem in 2-axis gimbal pointing and stabilization", *Automatic Target Recognition XX; Acquisition, Tracking, Pointing, and Laser Systems Technologies XXIV; and Optical Pattern Recognition XXI*, *Pro. SPIE*, 7696, 76961I, (2010).
- J. M. Ham, C. Williams, K. B. Shonkwiler, "Arduino-based control system for measuring ammonia in air using conditionally-deployed diffusive samplers", *AGU Fall Meeting Abstracts*, december,(2012).
- E. Emilsson, J. Rydell, "Sensor fusion for improved indoor navigation", *Electro-Optical Remote Sensing, Photonic Technologies, and Applications VI*, *Proc. SPIE*, 8542,85420M, september,(2012).
- Shang-Teh, Jeng-Young, "Time-Optimal Control of Servo Systems Using PD Algorithms", *JSME International Journal Series C*,*Proc. SPIE*, 41, (1998).
- Dominic J. Benford, Dale J. Fixsen, Stephen A. Rinehart, Maxime Rizzo, Stephen F. Maher, Richard K. Barry, "Precision attitude control for the BETTII balloon-borne interferometer," *Proc. SPIE* 8444, *Ground-based and Airborne Telescopes IV*, 84442P (10 October 2012);

-
- David J. Sahnou, Jeffrey W. Kruk, Thomas B. Ake, B-G Andersson, Alice Berman, William P. Blair, Robert Boyer, James Caplinger, Humberto Calvani, Thomas Civeit, W. Van Dyke Dixon, Martin N. England, Mary Elizabeth Kaiser, Mark Kochte, H. Warren Moos, Bryce A. Roberts, "Operations with the new FUSE Observatory: three-axis control with one reaction wheel," Proc. SPIE 6266, Space Telescopes and Instrumentation II: Ultraviolet to Gamma Ray, 626602 (7 June 2006);
- B. P. Crill and P. A. R. Ade, E. S. Battistelli, "SPIDER: a balloon-borne large-scale CMB polarimeter", Space Telescopes and Instrumentation 2008: Optical, Infrared, and Millimeter, Proc.SPIE,7010, 70102P, (2008).
- M. J. Rizzo, S. A. Rinehart, J. B. Alcorn et al., "Building an interferometer at the edge of space: pointing and phase control system for BETTII", Space Telescopes and Instrumentation 2014: Optical, Infrared, and Millimeter Wave, Proc.SPIE, 9143, 91433H,(2014).
- Margarita Safonova, Akshata Nayak and A. G. Sreejith et al., "An Overview of High-Altitude Balloon Experiments at the Indian Institute of Astrophysics", Astronomical and Astrophysical Transactions (AApTr), 29, (2016).
- A. G. Sreejith, Joice Mathew , Sarpodtar Mayuresh et al., "A Raspberry Pi-Based Attitude Sensor", Journal of Astronomical Instrumentation, 03,(2014).
- Ambily Suresh, Mayuresh Sarpotdar, Joice Mathew et al., "Development of Data Acquisition Methods for an FPGA-Based Photon Counting Detector", Journal of Astronomical Instrumentation, 06, (2016).
- , Sarpotdar Mayuresh and Joice Mathew and A.G. Sreejith and et al. "A software package for evaluating the performance of a star sensor operation", Experimental Astronomy, 43, Feb, (2017).

- A. G. Sreejith, Joice Mathew, Sarpodtar Mayuresh et al., "Measurement of limb radiance and Trace Gases in UV over Tropical region by Balloon-Borne Instruments – Flight Validation and Initial Results", Atmos. Meas. Tech. Discuss,(2016).
- R. K. Manchanda, J. V. Subba Rao, S. Sreenivasan et al., "Study of seasonal variation of winds in upper stratosphere over Hyderabad", Advances in Space Research", 47,480-487,february,(2011).
- A. G. Sreejith, Joice Mathew, Mayuresh Sarpotdar et al., "Balloon UV Experiments for Astronomical and Atmospheric Observations", Proc. of SPIE,(2016).
- Margarita Safonova, K. Nirmal, A. G. Sreejith et al., "Measurements of Gondola Motion on a Stratospheric Balloon Flight", IIA Technical Reports Series, 1-9, (2016).